Wave dynamics in origami-based mechanical metamaterials

Hiromi Yasuda

A dissertation
submitted in partial fulfillment of the
requirements for the degree of

Doctor of Philosophy

University of Washington

2018

Reading Committee:

Jinkyu Yang, Chair

Richard Wiebe

Marco Salviato

Program Authorized to Offer Degree:
Aeronautics and Astronautics

University of Washington

Abstract

Wave dynamics in origami-based mechanical metamaterials

Hiromi Yasuda

Chair of the Supervisory Committee:
Professor Jinkyu Yang
Department of Aeronautics and Astronautics

Origami has recently received significant interest from the scientific and engineering communities as a method for designing building blocks of engineered structures to enhance their mechanical properties. However, the primary focus has been placed on their kinematic applications by leveraging the compactness and auxeticity of planar origami platforms. In this thesis, we study two different types of volumetric origami structures, Tachi-Miura Polyhedron (TMP) and Triangulated Cylindrical Origami (TCO), hierarchically from a single unit cell level to an assembly of multi-origami cells. We strategically assemble these origami cells into mechanical metamaterials and demonstrate their unique static/dynamic mechanical responses. In particular, these origami structures exhibit tailorable stiffness and strain softening/hardening behaviors, which leads to rich wave dynamics in origami-based architectures such as tunable frequency bands and new types of nonlinear wave propagations. One of the novel waveforms investigated in this thesis is the rarefaction solitary wave arising from strain-softening nature of origami unit cell. This unique wave dynamic mechanism is analyzed in numerical, analytical, and experimental approaches. By leveraging their tailorable folding mechanisms, the origami-based mechanical metamaterials can be used for designing new types of engineering devices and structures, not only for deployable space and disaster relief applications, but also for vibration filtering, impact mitigation, and energy harvesting.

TABLE OF CONTENTS

LIST OF FIGURES

ACKNOWLEDGMENTS

First of all, I would like to express sincere appreciation to my supervisor, Professor Jinkyu Yang, for his invaluable advise and insightful guidance in this research project. Without his support, encouragement, and generosity, this thesis would not have been possible. In addition, he provided me with the academic freedom which allows me to explore my research interests. I also would like to thank the committee members, Prof. Richard Wiebe, Prof. Marco Salviato, Prof. Behcet Acikmese, and Prof Jayadev Athreya, for providing constructive commnets and insightful suggestions.

Also, I would like to thank the wonderful collaborators from various research fields and countries: Prof. Panayotis G. Kevrekidis (University of Massachusetts), Prof. Christopher Chong (Bowdoin College), Dr. Efstathios G. Charalampidis (University of Massachusetts), Prof. Eunho Kim (Chonbook National University, Korea), Prof. Mason A. Porter (University of Oxford, UK), Prof. Tomohiro Tachi. (University of Tokyo, Japan), Prof. Takahiro Kunimine (Kanazawa University ,Japan), and Prof. Rui Zhu (Beijing Institute of Technology).

Last but not least, I would like to express my gratitude to the past and present members of the Laboratory for Engineered Materials and Structures (LEMS) for their support and kindness: Rajesh Chaunsali, Hyunryung Kim, Seunghyun Ko, Chun-Wei Chen, Xiaotian Shi, James O'Neil, Balakumaran Gopalarethinam, Qingqian Li, Rohith Jayaram, Yasuhiro Miyazawa, Kosei Tsujikawa, Koshiro Yamaguchi , Dr. Gil-Yong Lee, Aman Thakkar, Noel Kimber, Joshua Rivey, Taru Singhal, Dr. Yang Nan, Dr. Hyung-Joon Bang, Ying Wu, Cheng Luo, Hannah Lee, Hannah Stevens, Riley Pratt, Mia Lee, Zhisong Chen, Charles King.

DEDICATION

to my parents, and brother, Tomohiro.

Chapter 1

INTRODUCTION

Origami is the traditional Japanese art of paper folding. By introducing crease lines in surface materials, we can fold the flat configuration into various 3D shapes. Recently, origami has attracted a significant amount of attention from researchers due to its unique mechanical properties. One of the advantages of using origami design principle is its drastic shape change, which leads to compactness and deployability enabling various types of expandable engineering structures, e.g., deployable solor panels in space [1], space solar sails [2], and solar arrays [3]. Also, in nature, one can find such compact origami patterns, such as foldable tree leaves [4, 5] and insect wings [6–8]. Based on the recent studies on origami structures, the design principles for origami have been extensively studied, which enable us to create complicated 3D shapes from sheet materials. For example, Tachi developed a software, called "origamizer", which creates flat craese patters from a given 3D shape [9]. Another useful aspect of origami-based structures is that origami patterns can enhance static mechanical properties of structures. For instance, structural bending rigidity for thin-walled cylindrical structures can be significantly improved by imposing origami-patterns [10]. These origami patterns are used not only for space structures, but also in commercial products (e.g., beverage cans to reduce the thickness of thin-walled structures without sacrificing their buckling strength).

Recently, the concept of origami has been stretched to to a wider range of design principles, such as robotics [11], reconfigurable structures [12], and self-folding actuated by living-cells [13]. In particular, origami has great potential to serve as a versatile platform for mechanical metamaterials which are another newly emerging research topic. Mechanical metamaterials offer a new dimension in achieving nonconventional and tailored mechanical properties through architectures instead of their chemical compositions [14–18]. The previous studies have shown the potential of origami to design building blocks for constructing mechanical metamaterials [19–23]. In particular, a quadrangular mesh origami, e.g., Miura-ori pattern [1], has been studied extensively, because it offers a single degree of freedom (DOF) mechanism of folding without relying on the elasticity of materials. This structure is called rigid (foldable) origami, and its 1-DOF motion can be beneficial for the control of deployable planar structures, such as solar panels and sails [2, 3] and sandwich core materials [24].

In contrast to the rigid planar origami, three dimensional volumetric origami has been relatively unexplored [25]. This is because the kinematics of volumetric origami is more complicated than planar ones, often deviating from rigid foldability. In the context of designing practical engineering applications, such as deployable space structures, space habitat, and foldable archtectures for disaster-relief activities, the volumetric structures have great advantage over the planer structures. In this thesis, we adopt two different origami structures as a building block of mechanical metamaterials to achieve enhanced mechanical properties such as tunable stiffness, wave filtering, and effective impact mitigation. One of the origami structures to investigate is the Tachi-Miura Polyhedron (TMP), which is a bellows-like 3D origami structure based on Miura-ori cells [26, 27] (see Fig. 1.1A for the folding motion of the TMP unit cell). Lateral assembly of Miura-ori cells in the form of Miura-ori sheets has been previously explored for the construction of metamaterials [19]. However, there have been limited efforts to study the cylindrical derivative of Miura-ori in the form of TMP [28]. In contrast to 2D origami structures such as Miura-ori sheets and waterbomb [29], the TMP holds a volume that changes continuously from zero to a certain value, and then it returns to zero again at the ends of the folding motion (see Fig. 1.1A). This implies that we can obtain a very large stroke from its folding motion, which is useful in designing actuators and impact absorbers. Also, compared to other origami-based cylindrical structures [30–34], the TMP has a unique feature of rigid foldability. That is, the deformation takes place only along crease lines instead of relying on the elasticity of materials. Therefore, the structure can consist of only rigid panels and hinges without incurring bending of planar origami surfaces.

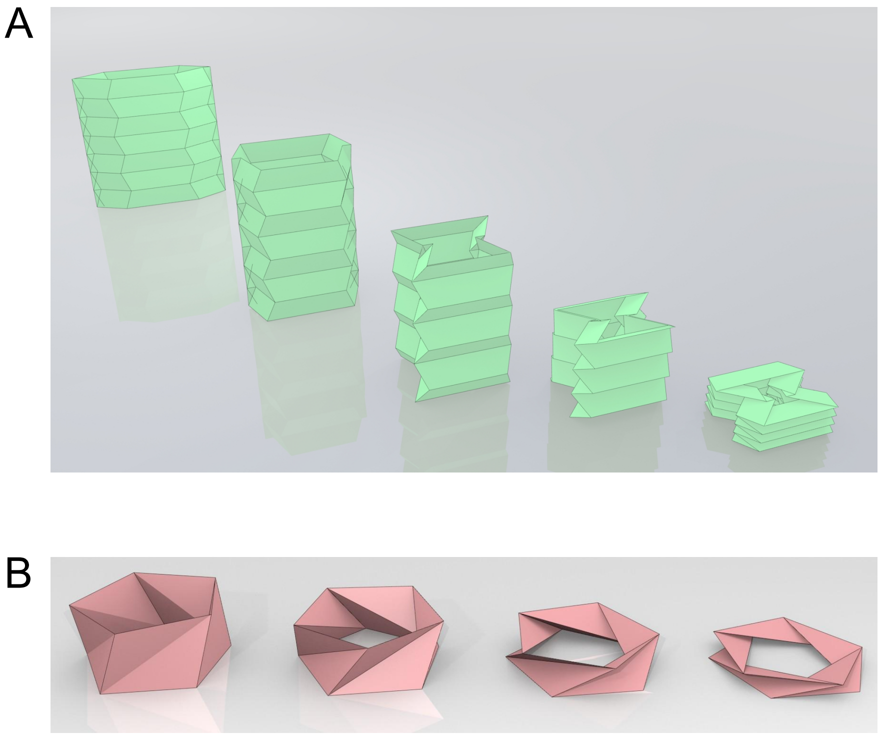

Figure 1.1: Volumetric origami structures. (**a**) Tachi-Miura Polyhedron (TMP), and (**b**) Triangulated Cylindrical Origami (TCO).

The other volumetric origami structure that we investigate is the triangulated cylindrical origami (TCO) [10,30,31,34–37], which can develop coupled dynamics of axial and rotational motions during folding (Fig. 1.1B). What makes this volumetric origami structures more appealing is this coupled behavior of folding and deformation, which can result in versatile kinematic and dynamic motions. For example, the wave-mode switching via wave mixing effects has been reported based on a similar 2-DOF system [38]. Also, isolation of stress wave in a coupled system has been investigated in a helicoidal setting of phononic crystals [39]. These studies have demonstrated unique wave manipulation based on the coupled behavior numerically. However, the experimental realization of such unique wave dynamics has been relatively unexplored due to the difficulty in building the wave medium with coupled dynamic motions. Therefore, building such a versatile platform will be of immense significance, potentially providing the breakthrough in the research field of stress wave control and management. In addition, unlike the TMP, the conventional bellows-like structures (e.g., accordion) generally inherit a highly nonlinear elastic behavior, making the aforementioned rigid foldability observed in TMP no longer valid. While this multi-DOF behavior with deformable surfaces poses formidable challenges in the analysis of volumetric origami, the TCO architecture can also offer a rich playground for forming and validating a variety of nonlinear wave dynamics.

In this thesis, by studying the two volumetric origami structures: the TMP and TCO, we design and analyze the origami-based mechanical systems in terms of their static and dynamic mechanical responses. For the static response, we first examine the kinematics of the TMP unit cell, specifically the Poisson's ratio, and we find that the TMP can exhibit negative Poisson's ratio, which can be utilized to manipulate wave propagation [40]. Then, we investigate the relationshp between axial force and displacement. Interestingly, by controlling geometrical parameters such as height and angle between the crease lines, the TMP structure shows negative stiffness as well as tunable stiffness. Previous studies reported that structural instability can be used to achieve tailored damping characteristics in mechanical metamaterials [41,42]. Therefore, this finding can lead to engineering devices dealing with vibrations and impact. Also, this tunable response can be further exploited to design foldable, yet highly stiff structures depending on the initial configuration of the structure. In addition to the TMP, we also study the static response of the TCO unit cells. We investigate the mechanics of volumetric origami, specifically demonstrating that the behavior of this TCO can be predicted analytically by modeling its deformable surfaces into the network of truss elements and by applying the minimum potential energy principle. We find a rich tunability in this TCO structure, which enables the design of monostable/bistable, zero-stiffness, and bifurcation structures from one-parameter family of the initial geometry.

Next, based on the static analysis of the TMP and TCO unit cells, we design a periodically arranged one dimensional chain composed of the TMP or TCO unit cells, and analyze linear/nonlinear wave propagation in this origami-based system. Although the dynamic analysis on origami-based structure is the natural next step to investigate, the connection between the origami crease pattern and the dynamic folding/unfolding behavior of origami itself has been relatively unexplored [24, 33]. In particular, very few experimental studies have been reported [2, 43]. One of the reasons is that the primary focus has been placed on the static or quasi-static properties of origami, and limited work has been reported on the dynamic response of origami-based structures [24]. Another reason is the intrinsic characteristic of typical origami structures, which exhibit limited DOF during their folding/unfolding motions. This is particularly true for rigid origami, in which the deformation takes place only along crease lines, while origami facets remain rigid in dynamic conditions. The rigid origami features single-DOF motions ideally, and thus, the studies on their wave dynamics have been more or less absent under this rigid foldability assumption. In this study, we use the TMP/TCO unit cell as a building block to assemble multi-DOF mechanical metamaterials, and we analyze their frequency band structure in the first place. The numerical and analytical results show the formation of frequency band gap, which forbids a certain frequency components propagating in the structure, when the chain is composed of two different configurations of the origami unit cell. In addition to this frequency band gap, for the TCO-based system, we observe the wave mixing behavior due to the coupling of axial and rotational motions of each TCO unit cell.

Finally, we study nonlinear wave dynamics in the origami-based system, specifically impact response of the system. The reason why the impact response is chosen is that one of the common issues for engineering structures is external impact which can induce catastrophic damage to the structures. Therefore, the effective impact mitigation is the important aspect of practical applications. We first consider the chain consisting of simplified TMP unit cell for preliminary investigation because the TMP is a single DOF structure which provides a simple theoretical and numerical handling. By applying compressive impact to the TMP-based system, we conduct the theoretical and numerical analysis, and we observe the formation of the rarefaction solitary wave, tsunami-like nonlinear wave with tensile strain, propagating in the chain. Interestingly, this rarefaction solitary wave propagating ahead of the initial compressive strain wave despite the application of compressive impact. Also, this compressive strain wave is attenuated significantly.

While the TMP architecture offers this rich wave dynamics, the experimental fabrication of rugged TMP systems requires highly sophisticated procedures. Thus, for the the experimental verification of this unique wave propagation, we use the TCO unit cell because of the ease of prototype fabrication. We develop both software (non-contact digital image correlation technique based on Python and OpenCV [44]) and hardware (customized laser-cut crease lines for paper sheets), and experimentally capture the rarefaction solitary wave with overtaking behavior. As a result, we successfully verify the formation of rarefaction solitary waves in the chain of the TCO cells. To the best of our knowledge, this is the first work to report the existence of rarefaction solitary waves in the mechanical setting.

This thesis is structured as follows: In Chapter 2, we describe the static analysis on the TMP and discuss negative Poisson's ratio and tunable stiffness. In Chapter 3, we investigate the static response of the TCO analytically and experimentally. We find the four distinctive different behaviors: mono-/bistable behaviors, zero-stiffness mode, and bifurcation behavior. Then, in Chapter 4 we design the chain of the TMP unit cells and analyze the frequency band structure. Similarly, in Chapter 5, we study the wave mixing effect is studied as well as tunable frequency band structure. In Chapter 6, the nonlinear wave propagation, specifically the rarefaction solitary wave, is discussed numerically, and then, in Chapter 7, we demonstrate the rarefaction solitary wave not only in numerical approach but also in experimental approach. Lastly, concluding remarks and future work are given in Chapter 8.

Chapter 2

STATIC MECHANICAL RESPONSE OF THE TMP

In this Chapter, we first examine the kinematics of the TMP (see Fig. 2.1(a) for the folding motion of the TMP unit cell) to show the tunable characteristics of its Poisson's ratio. We verify analytically and experimentally the auxetic effect of volumetric 3D TMP prototypes in bilateral directions, which is an improvement over the conventional 2D origami structures with a single-directional negative Poisson's effect [19, 20, 45]. Second, we investigate the force-displacement relationship in the longitudinal axis of the TMP structure to show that it exhibits unique force-displacement curves with local minima under the re-entrant configurations. Then, a cellular structure consisting of the TMP cells is explored to form origami-based metamaterials with a view toward potential engineering applications. Lastly, we examine the force-displacement relationship in other directions, and show that the TMP unit cell can exhibit a flat-foldble, yet highly stiff configuration.

2.1 Modeling of the TMP structure

We begin with characterizing the geometry of the TMP. Figures 2.1(b) and (c) show the folded TMP cell in slanted and top views, respectively. This unit cell consists of two flat sheets, whose geometry can be characterized by length parameters (l, m, d) and an inner angle of parallelogram (α) (Fig. 2.1(d)). The point Q is defined by the two crossing edges of the front and rear surfaces as shown in Fig. 2.1(c), which passes through the quarter line of the sheets (dash-dot line in Fig. 2.1(d)). Accordingly, the half breadth ($B/2$) of the TMP cell corresponds to the distance between points O and Q along the y-axis, and the half width ($W/2$) is the distance between points O and R along the x-axis (Figs. 2.1(c)). The

---

The texts and figures in this Chapter have been partly taken from the author's publication [46].

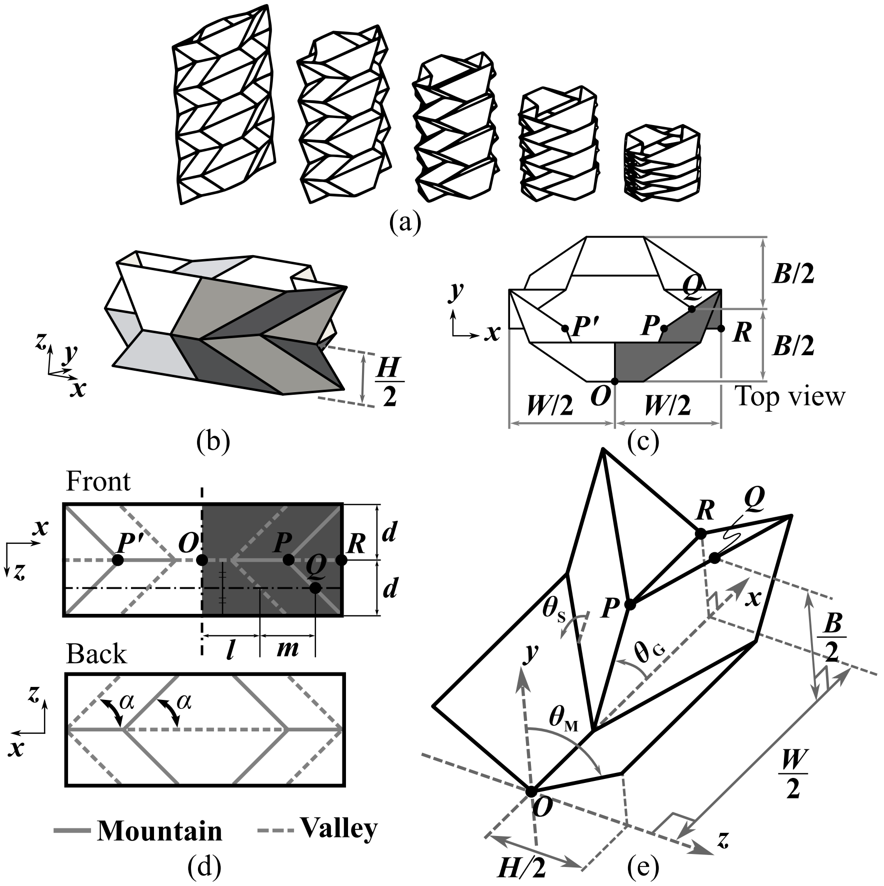

Figure 2.1: (**a**) Folding motion of Tachi-Miura Polyhedron (TMP). (**b**) Folded TMP cell. (**c**) Top view of TMP. (**d**) Flat front and rear sheets of TMP with the crease pattern consisting of mountain and valley folds. (**e**) Folded configuration of the front sheet corresponding to the shaded areas in (**c**) and (**d**).

half height ($H/2$) of the TMP cell is also illustrated in Fig. 2.1(b). Note that the TMP cell exhibits a re-entrant shape when the given geometrical angle α is above 45°.

To calculate W, B, and H under various folding configurations, we consider a quarter model of the TMP (Fig. 2.1(e)), which corresponds to the dark colored area in Figs. 2.1(b)-(d). Here, the folding angles, θ_M and θ_S, are functions of α (determined by the given geometry) and θ_G (varies by the degree of folding). It should be noted that while $\theta_M \in [0, 90°]$ and $\theta_S \in [0, 90°]$, the range of α is limited to satisfy $2l - d\cot\alpha + 2m\cos 2\alpha > 0$. This is to avoid the collision between points P and P' during folding. Accordingly, $\theta_G \in [0, 2\alpha]$. The building block for the TMP is the Miura-ori unit (Fig. 2.2). In Fig. 2.2, we define the three different folding angles; θ_M, θ_S, and θ_G. There are relationships among these three angles as

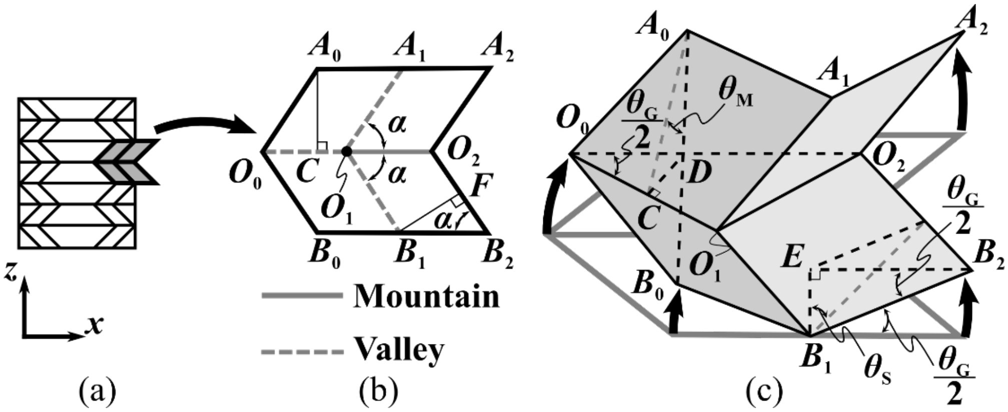

Figure 2.2: (**a**) Tachi-Miura Polyhedron. (**b**) Miura-ori unit cell which is folded into (**c**).

$$\frac{CD}{O_0C} = \frac{A_0C}{O_0C}\frac{CD}{A_0C} \quad \Leftrightarrow \quad \tan\frac{\theta_G}{2} = \tan\alpha\cos\theta_M, \tag{2.1}$$

$$\frac{B_1E}{B_1B_2} = \frac{B_1F}{B_1B_2}\frac{B_1E}{B_1F} \quad \Leftrightarrow \quad \sin\frac{\theta_G}{2} = \sin\alpha\cos\theta_S. \tag{2.2}$$

Taking a derivative of above two equations, we obtain

$$d\theta_G = \left(-2\tan\alpha\cos^2\frac{\theta_G}{2}\sin\theta_M\right)d\theta_M, \tag{2.3}$$

$$\frac{1}{2}\cos\frac{\theta_G}{2}d\theta_G = -\sin\alpha\sin\theta_S d\theta_S. \tag{2.4}$$

Therefore,

$$d\theta_S = -\frac{1}{2}\frac{\cos\frac{\theta_G}{2}}{\sin\alpha\sin\theta_S}d\theta_G = \frac{\cos^3\frac{\theta_G}{2}\sin\theta_M}{\cos\alpha\sin\theta_S}d\theta_M. \tag{2.5}$$

Also, the geometry described in Fig. 2.1, W, B, and H are obtained as follows:

$$B \quad = 2m\sin\theta_G + d\cos\theta_M \tag{2.6}$$

$$W \quad = 2l + \tfrac{d}{\tan\alpha} + 2m\cos\theta_G \tag{2.7}$$

$$H \quad = 2d\sin\theta_M. \tag{2.8}$$

Taking a derivative of these equations, we obtain

$$dB = (2m\cos\theta_G)\,d\theta_G - (d\sin\theta_M)\,d\theta_M \tag{2.9}$$

$$dW = (-2m\sin\theta_G)\,d\theta_G \tag{2.10}$$

$$dH = (Nd\cos\theta_M)\,d\theta_M. \tag{2.11}$$

Here, we investigate the Poisson's ratios of the TMP by defining them as

$$\nu_{HB} = -\frac{(dB/B\ )}{(dH/H\ )} \quad \text{and} \quad \nu_{HW} = -\frac{(dW/W\ )}{(dH/H\ )}. \tag{2.12}$$

Differentiating Eq. (2.6) with respect to the folding angles and plugging them into Eq. (2.12), we obtain the Poisson's ratios as follows:

$$\begin{aligned} \nu_{HB} &= \frac{4m\tan\alpha\cos\theta_G\cos^2(\theta_G/2) + d}{2m\sin\theta_G + d\cos\theta_M}\sin\theta_M\tan\theta_M \\ \nu_{HW} &= -\frac{4m\tan\alpha\sin\theta_G\cos^2(\theta_G/2)}{2l + (d/\tan\alpha) + 2m\cos\theta_G}\sin\theta_M\tan\theta_M. \end{aligned} \tag{2.13}$$

To verify this analytical expression, we fabricate three prototypes of the TMP ($\alpha = 30°$, $45°$, and $75°$) by using paper. The number of Miura-ori layers used in each configuration is $N = 7$, and the characteristic lengths of the prototypes are identical ($l = m = 50$ mm and $d = 30$ mm). We conduct three measurements of B and W at each H, as we gradually change the folding angle. We compare the measured Poisson's ratios with the analytical results from Eq. (2.13).

2.2 Measurement of Poisson's ratio and cross-sectional area

In order to verify analytical expression of the Poissons ratio, we fabricate three prototypes of the TMP ($\alpha = 30°$, $45°$, and $75°$) by using paper (Strathmore 500 Bristol, 2-Ply, Plate Surface, 23572). Length parameters (l, m, d) = (50 mm, 50 mm, 30 mm) are chosen.

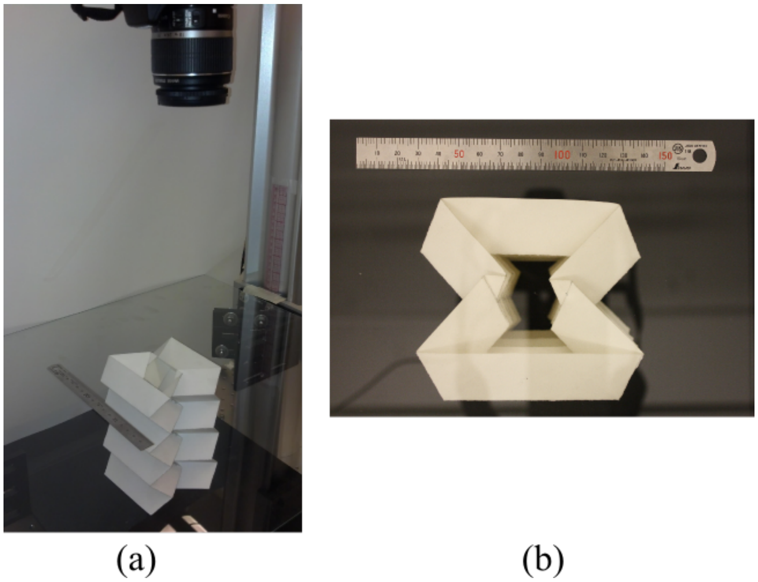

Figure 2.3: (**a**) Experimental setup. (**b**) Digital image taken from a camera mounted on top of a TMP prototype.

Figure 2.3 shows the experimental setup to measure the cross-sectional area of the TMP. A glass plate is placed on the top surface of the TMP to control the height of the TMP, and a camera captures a digital image of the cross-sectional area of the TMP from above. Based on the digital images from a camera, we measure the breadth (B), width (W), and cross-sectional area of the TMP with different height (H). To measure B and W, we use Image J software [47]. The measurement was conducted three times on each TMP prototype. In order to obtain the Poissons ratio from the experiment, we modify Eq. (2.13). Substituting

Eqs. (2.9) into Eq. (2.13), we obtain

$$\nu_{HB} = \frac{H\left(4m\cos 2\theta_G \tan\alpha \cos^2\theta_G \sin\theta_M + d\sin\theta_M\right)}{B\left(Nd\cos\theta_M\right)}, \tag{2.14}$$

$$\nu_{HW} = -\frac{4mH\sin 2\theta_G \tan\alpha \cos^2\theta_G \sin\theta_M}{W\left(Nd\cos\theta_M\right)}. \tag{2.15}$$

Where θ_M is calculated from Eq. (2.1), and θ_S and θ_G are calculated from Eq. (2.6).

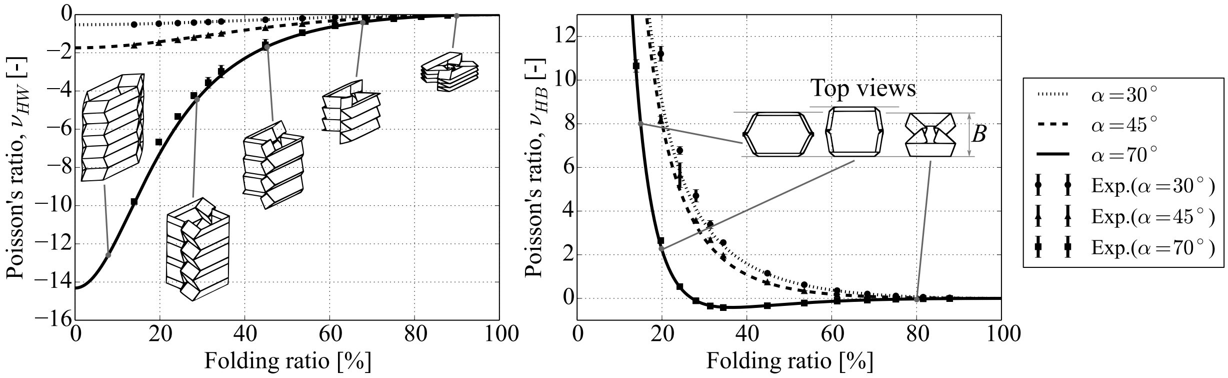

(a) $l = m = 50$, $d = 30$ (b) $l = m = 50$, $d = 30$

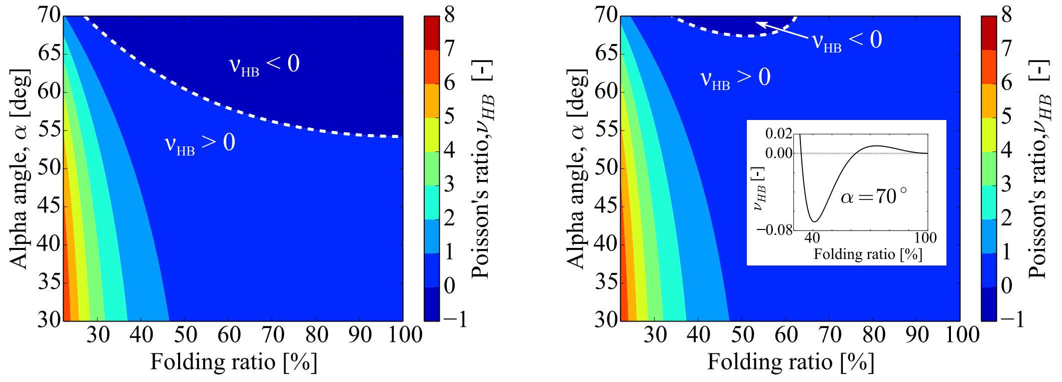

(c) $l = m = 50$, $d = 30$ (d) $l = m = 50$, $d = 60$

Figure 2.4: Poisson's ratio change of TMP. (**a**) ν_{HW} and (**b**) ν_{HB} as a function of the folding ratio. Insets show folded configurations of re-entrant TMP under $\alpha = 70°$ and $l = m = 50, d = 30$ mm. Errorbars indicate standard deviations. Contour plot of ν_{HB} as a function of α and the folding ratio if (**c**) $d = 30$ and (**d**) $d = 60$. The white dashed line indicates the boundary between positive and negative ν_{HB}.

Figure 2.4 shows the Poisson's ratios as a function of a folding ratio defined as $(90° - \theta_M)/90°$. The Poisson's ratio ν_{HW} in the case of $\alpha = 45°$, 30°, and 70° are plotted in

Fig. 2.4(a), while the insets show the folded configurations under $\alpha = 70°$. We find ν_{HW} is always negative regardless of the folding ratio and α. On the other hand, the Poisson's ratio ν_{HB} related to width B is positive in the initial folding stage, and it approaches zero. It is notable that in the re-entrant case (e.g., $\alpha = 70°$), ν_{HB} becomes negative as shown in Fig. 2.4(b). As seen in the inset, we evidently observe that B increases and then decreases as the folding ratio of the re-entrant TMP increases. We find excellent agreement between the experimental and analytical results. The areal change of the TMP is also measured and compared with the analytical predictions in the supplemental document.

The analytical contour plot of ν_{HB} as a function of continuous α and the folding ratio is shown in Fig. 2.4(c). If α is above approximately 55°, ν_{HB} becomes negative during the folding motion. Fig. 2.4(d) also shows the contour plot of ν_{HB} but $d = 60$ mm. By choosing a certain α angle (e.g. $\alpha = 70°$ as shown in the inset of Fig. 2.4(d)), we observe ν_{HB} changes from positive to negative in the initial folding stage, and then it becomes positive again around 62 %. The sign of ν_{HB} changes multiple times in one folding motion. This is a unique feature of the TMP compared to the conventional 2D Miura-ori, in which negative Poisson's effect has been reported, but multiple sign flips of the Poisson's ratio has not been discovered [19,20,45]. Solving $dB = 0$, we obtain the analytical expression for the transition between positive and negative ν_{HB}:

$$\cos^2\theta_M = \frac{2m\tan\alpha - d \pm 2\sqrt{m\tan\alpha\,(m\tan\alpha - 2d)}}{d\tan^2\alpha}. \tag{2.16}$$

This boundary is plotted in a dashed curve in Fig. 2.4(c,d).

In addition to the measurement on B and H, we also measure the cross-sectional area of the TMP. Figure 2.5 shows the cross-sectional area change as a function of the folding ratio defined. Since both ν_{HB} and ν_{HW} approach to zero in the final stage of the folding ratio, the change of the cross-sectional area becomes relatively small, which indicates that the structure can be folded with small cross-section change. This feature can be exploited for designing an actuator with small cross-section change.

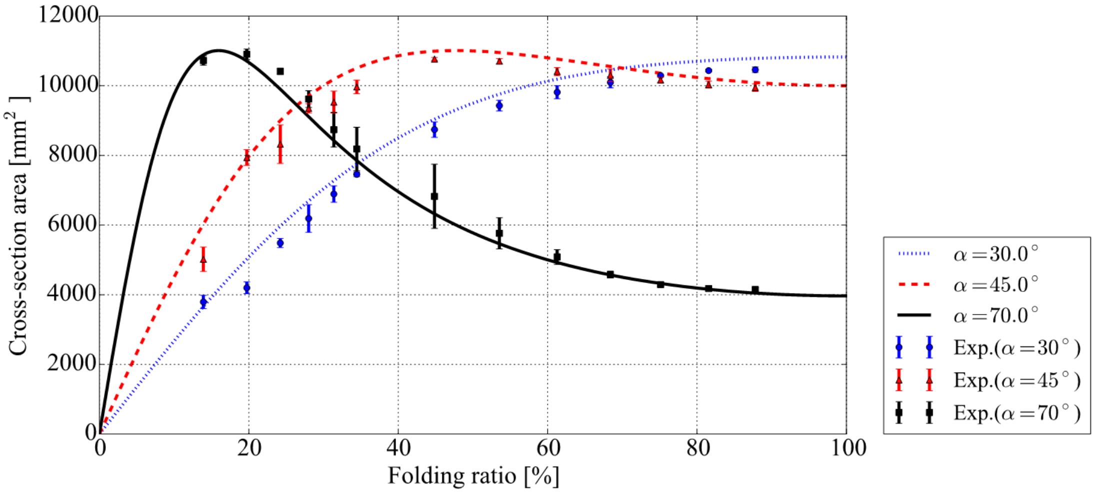

Figure 2.5: Cross-sectional area change of the TMP. Error bars indicate standard deviations.

2.3 *Force-folding ratio relationship*

Now we investigate force and folding ratio relationship to validate the unique force-displacement curves of the TMP. We model the TMP by rigid plates connected by torsional spring along the crease lines (see supplemental document for details). We consider the folding behavior of the TMP under a uniaxial force (F) in the z-direction. By applying virtual displacement (δu) to the TMP and using the principle of virtual work, we obtain the following equation:

$$F\delta u = 2n_M M_M \delta\theta_M + 2n_S M_S \delta\theta_S, \tag{2.17}$$

where $n_M = 8(N-1)$ and $n_S = 8N$ are the number of horizontal and inclined crease lines related to θ_M and θ_S respectively, and M_M (M_S) is the bending moment along horizontal (inclined) crease lines. Let the torsional spring constant be k_θ, assuming that the torsion spring is linear and identical throughout all crease lines. Mathematically, this can be expressed as $M = 2k_\theta\left(\theta - \theta^{(0)}\right)$ where $\theta^{(0)}$ is the initial folding angle (i.e., natural angle with no potential energy). Based on the geometry of the TMP and Eq. (2.25), the compressive force can be expressed as (see supplemental document for details):

$$\frac{F_3}{(k_\theta/d\ )} = -\frac{32}{\cos\theta_M}\left\{\frac{N-1}{N}\left(\theta_M-\theta_M^{(0)}\right)+\left(\theta_S-\theta_S^{(0)}\right)\frac{\cos^3\frac{\theta_G}{2}\sin\theta_M}{\cos\alpha\sin\theta_S}\right\} \tag{2.18}$$

where the subscript, 3, indicates z-axis (see Fig. 2.1). Note that we use a normalized force to remove the effect of spring coefficient and the dimension of the TMP.

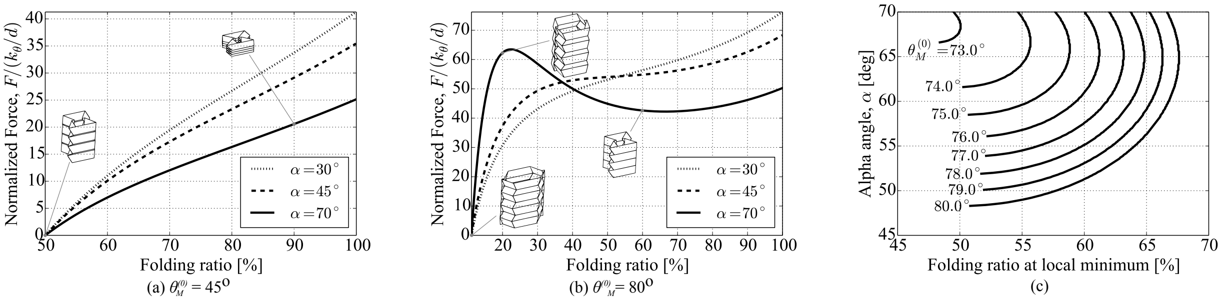

(a) $\theta_M^{(0)} = 45^{\circ}$

(b) $\theta^{(0)}{}_M = 80^{\circ}$

(c)

Figure 2.6: Force-folding ratio relationship. The number of layers N is 7, and initial folding angle is (**a**) $\theta_M^{(0)} = 45°$ and (**b**) $\theta_M^{(0)} = 80°$. Illustrations indicate the folded shape of the TMP with $\alpha = 70°$. (**c**) Folding ratio at local minimum point under different initial angles $\theta_M^{(0)}$.

Figure 2.6 shows the force-folding ratio relationship of the TMP under different initial conditions. When the natural folding angle $\theta_M^{(0)}$ is 45° and the number of layers N is 7, the normalized force increases monotonically regardless of α values as shown in Fig. 2.6(a). However, in the case of $\theta_M^{(0)} = 80°$ (i.e., a more upward initial posture than $\theta_M^{(0)} = 45°$), we observe the TMP with $\alpha = 70°$ exhibits a local minimum point in the force-folding relationship (see the solid curve in Fig. 2.6(b)). Then we investigate numerically the local minimum points under various combinations of α and $\theta_M^{(0)}$ values (Fig. 2.6(c)). We observe that the local minimum points arises when the TMP exhibits re-entrant shapes and appropriate initial folding angles are applied (minimal $\theta_M^{(0)}$ is 73° given the geometry), implying that by changing $\theta_M^{(0)}$, one can manipulate the stiffness of the TMP, particularly transform between positive and negative stiffness regimes.

2.4 Multi-TMP cellular structures

In this section, we explore the design of a cellular structure consisting of multiple TMP cells (Fig. 2.7). Similar to its unit cell, this TMP cellular structure transforms from a 2D state to another 2D configuration, while filling 3D space in the transition stage. Therefore, by taking advantage of the unique kinematics of the TMP unit cell discussed above, we can design a new type of 3D structures which exhibit tunable Poisson's ratio. Figure 2.7(a) shows the TMP cellular structure with $\alpha = 30^\circ$, where we observe the structure stretches in the y-direction while being contracted in the x-direction monotonically (i.e., positive ν_{HB} and negative ν_{HW}). If $\alpha = 70^\circ$, it expands in the y-direction at first behaving similar to the previous case, but past a certain threshold, it starts to shrink in all directions as shown in Fig. 2.7(b) due to the negative Poisson's ratios in bilateral directions. These TMP cellular structures are also one degree-of-freedom system. Therefore all TMP cells fold and unfold simultaneously by manipulating one parameter, folding angle θ_M in this study.

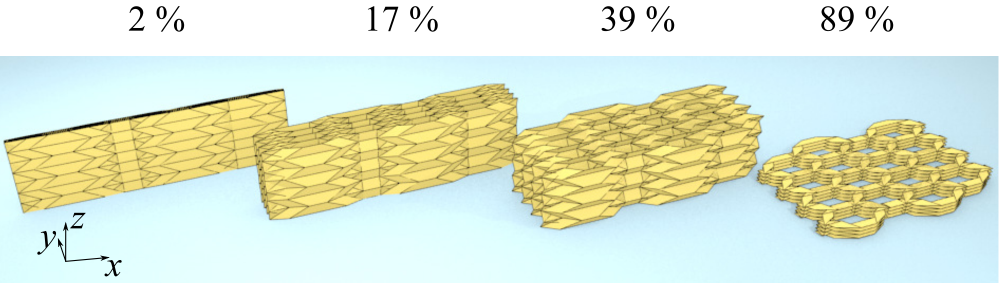

(a) $\alpha = 30^{\text{o}}$

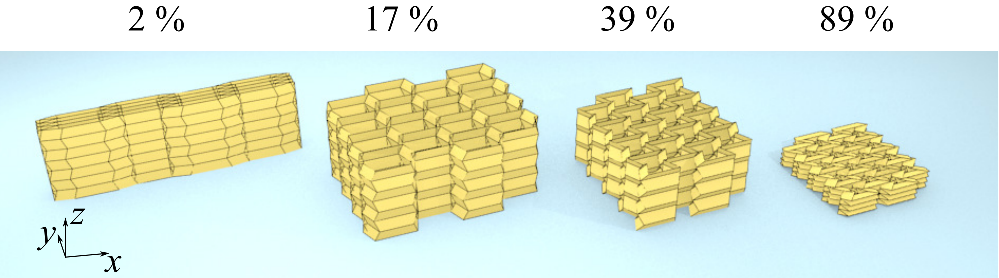

(b) $\alpha = 70^{\text{o}}$

Figure 2.7: Folding motions of TMP cellular structures. The numbers show folding ratios, and $l = m = 50$ mm, $d = 30$ mm. (**a**) $\alpha = 30°$. (**b**) $\alpha = 70°$.

2.5 Flat-foldable, yet highly stiff configuration

In the previous section, we discuss the force-folding relationship in the axial direction. Here, we examine the static mechanical response in the other two directions, and show that the TMP subjected to external force in the breadth direction exhibits flat-foldable, yet highly stiff configuration by controlling the initial shape of the structure (the conceptual illustration is shown in Fig. 2.8).

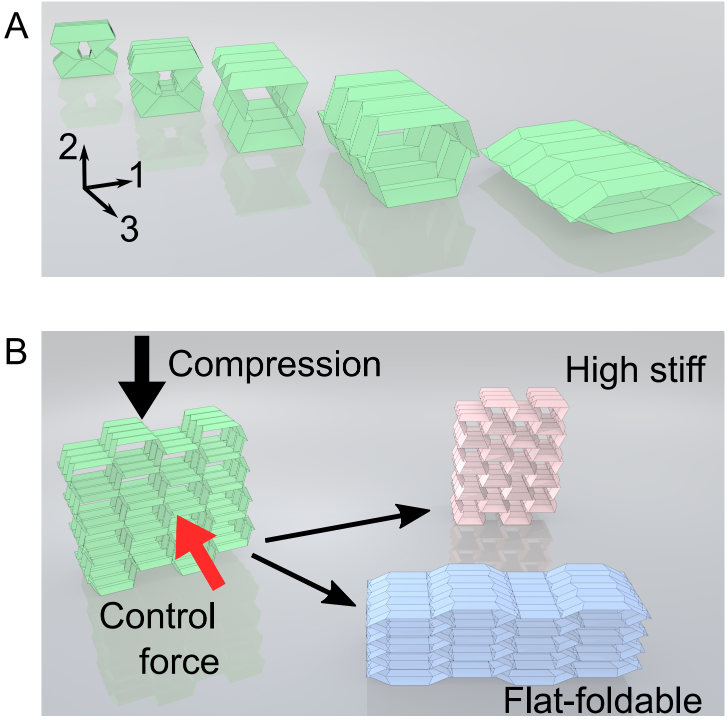

Figure 2.8: Conceptual illustration of flat-foldable, yet high stiff origami. (**a**) Sequence of unfolding behavior of the TMP unit cell. (**b**) Concept of flat-foldable yet high stiff multi-TMP cellular structure is shown.

Let 1,2,3-axis be the horizontal, vertical, and depth direction as shown in Fig. 2.9A, we first analyze the kinematic behavior by focusing on the the cross-section change. Defining an extension ratio as

$$\gamma = \theta_M/90^\circ, \tag{2.19}$$

we show the change of the width and breadth of the TMP unit cell with three different α angles;$\alpha = 30°$, $45°$, and $70°$ (see Fig. 2.9C and D).

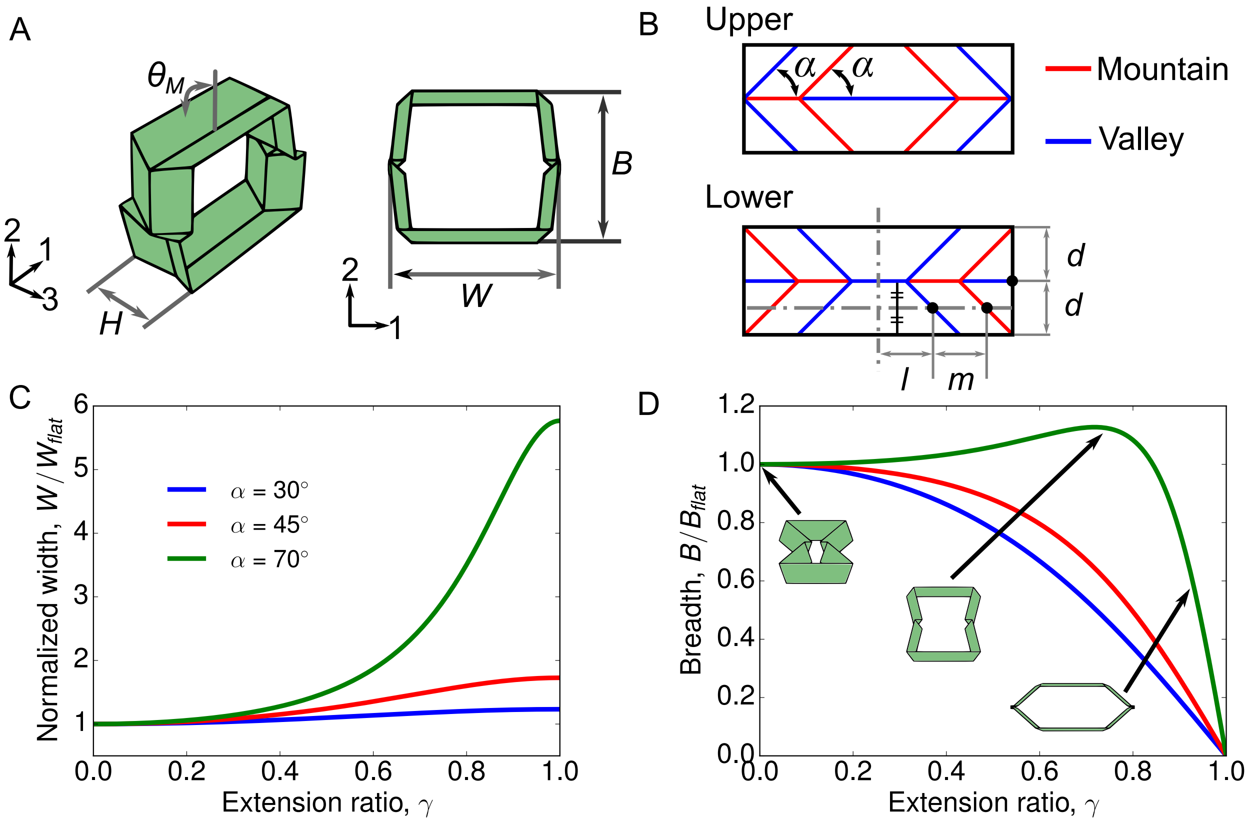

Figure 2.9: Geometry of the TMP uni cell and its folding kinematics. (**a**) The 3D view (Left) and cross-sectional view (Right) of the TMP unit cell. The TMP unit cell is composed of two sheets with mountain (red line) and valley (blue line) crease lines as shown in (**b**). The change of (**c**) Width and (**d**) Breadth of the TMP unit cell with $l = m = 40$ mm, $d = 30$ mm, and $N = 7$. The width and breadth are normalized by those values for $\gamma = 1$.

In Fig. 2.9C, the width of the TMP unit cell increases monotonically as the TMP transforms from the folded configuration in the 3-axis to the flat state unfolded in the 2-axis for all three α cases. On the other hand, for the breadth direction, the TMP with $\alpha = 70°$ shows non-monotonic change. Let γ_C and $\theta_G^{(c)}$ be the critical extension ratio (γ) and θ_G angle in which the structure takes its local maximum breadth, we obtain the critical state by solving

$dB/d\theta_M = 0$, which leads to

$$4\tan\alpha\cos\theta_G^{(c)}\cos^2\left(\frac{\theta_G^{(c)}}{2}\right)+\frac{d}{m}=0. \tag{2.20}$$

Then,

$$\cos^2\theta_G^{(c)}+\cos\theta_G^{(c)}+\frac{(d/m\ )}{2\tan\alpha}=0. \tag{2.21}$$

Please note that we can obtain the critical extension ratio (γ_C) by using Eqs. 2.21, 2.1, and 2.19.

Next, similarly to the previous section, we examine the relationship between force and displacement in 1-/2-direction. By using Eq. 2.6, we obtain

$$\delta u_1 = 2m\sin\theta_G\delta\theta_G \tag{2.22}$$

Therefore,

$$F_1=-\frac{8k_\theta}{m\sin\theta_G}\left\{\frac{(N-1)\left(\theta_M-\theta_M^{(0)}\right)}{\tan\alpha\cos^2\left(\theta_G/2\ \right)\sin\theta_M}+\frac{N\left(\theta_S-\theta_S^{(0)}\right)\cos\left(\theta_G/2\ \right)}{\sin\alpha sin\theta_S}\right\} \tag{2.23}$$

Normalizing this equation, we have

$$\frac{F_1}{(k_\theta/d\ )}=-\frac{8}{(m/d\ )\sin\theta_G}\left\{\frac{(N-1)\left(\theta_M-\theta_M^{(0)}\right)}{\tan\alpha\cos^2\left(\theta_G/2\ \right)\sin\theta_M}+\frac{N\left(\theta_S-\theta_S^{(0)}\right)\cos\left(\theta_G/2\ \right)}{\sin\alpha sin\theta_S}\right\} \tag{2.24}$$

Also, for 2-direction (i.e., breadth direction),

$$\begin{aligned}\delta u_2 &= -\left(2m\cos\theta_G\right)\delta\theta_G+\left(d\sin\theta_M\right)\delta\theta_M\\ &= -\left(2m\cos\theta_G\right)\left(-2\tan\alpha\cos^2\frac{\theta_G}{2}\sin\theta_M\right)\delta\theta_M+\left(d\sin\theta_M\right)\delta\theta_M\\ &= \sin\theta_M\left(4m\cos\theta_G\tan\alpha cos^2\frac{\theta_G}{2}+d\right)\delta\theta_M. \end{aligned}\tag{2.25}$$

Therefore,

$$\begin{aligned}F_2 &= \frac{4k_\theta}{\sin\theta_M\left\{4m\cos\theta_G\tan\alpha\cos^2\left(\theta_G/2\ \right)+d\right\}}\\ &\quad\times\left\{8\left(N-1\right)\left(\theta_M-\theta_M^{(0)}\right)+8N\left(\theta_S-\theta_S^{(0)}\right)\frac{\sin\theta_M\cos^3\left(\theta_G/2\ \right)}{\cos\alpha\sin\theta_S}\right\}\end{aligned}\tag{2.26}$$

Normalizing this equation, we obtain

$$\begin{aligned}\frac{F_2}{(k_\theta/d\ )} &= \frac{32}{\sin\theta_M\left\{4\,(m/d\ )\cos\theta_G\tan\alpha\cos^2(\theta_G/2\ )+1\right\}}\\ &\quad\times\left\{(N-1))\left(\theta_M-\theta_M^{(0)}\right)+N\left(\theta_S-\theta_S^{(0)}\right)\frac{\sin\theta_M\cos^3(\theta_G/2\ )}{\cos\alpha\sin\theta_S}\right\}\end{aligned} \tag{2.27}$$

Based on the analysis, we calculate the force-displacement relationship for the unit cell. Figure 2.10A shows the force-extension ratio relationship for 2-direction for two different initial extension ratios ($\gamma_0 = 0.71$ and 0.73). Two cases show distinctive behaviors; $\gamma = 0.73$ case shows foldable behavior with relatively small force (F_2), whereas $\gamma = 0.71$ case indicates that force increases exponentially, i.e., stiffness becoming higher as we compress, which means that it is extremely difficult to fold the structure in a practical sense. These distinctively different behaviors are determined by the critical extension ratio (γ_C) obtained by Eq. 2.20. Therefore, if we apply force (or displacement) to the TMP only in its 2-direction, the TMP is foldable in both 1- and 2-directions (i.e., bi-directionally flat-foldable structure) if $\gamma_0 < \gamma_C$, whereas, it becomes foldable in 1-direction yet high-stiff in 2-direction (i.e., one-directional foldable structure) if $\gamma_0 > \gamma_C$.

To examine this unique behavior for various configurations, we consider Eq. 2.21. If the TMP shows foldable in 1-direction and increasing stiffness in 2-direction, the structure satisfies the following conditions obtained from Eq. 2.21;

$$1-\frac{2\,(d/m\ )}{\tan\alpha} > 0 \tag{2.28}$$

$$-1+\sqrt{1-\frac{2\,(d/m\ )}{\tan\alpha}} > 2\cos 2\alpha. \tag{2.29}$$

Please note that $\theta_G \in [0, 2\alpha]$. Using these equation, we numerically examine the transition between the two distinctive behaviors under compression in 2-direction as shown in Fig. 2.10B where the blue region indicates that the TMP is bi-directionally flat-foldable, whereas the red region shows the flat-foldable in 1-direction yet increasing stiff configuration in 2-direction.

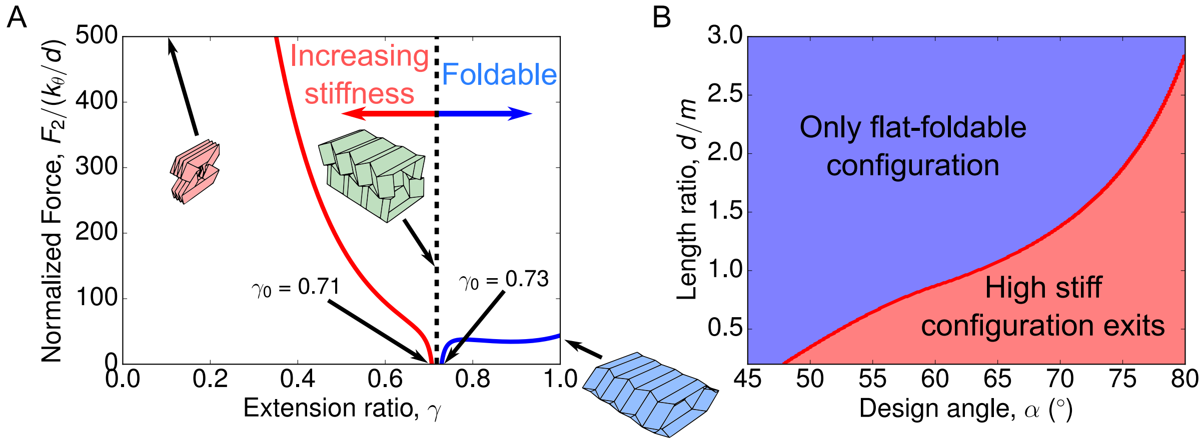

Figure 2.10: Analytical predictions of the folding behavior of the TMP. (**a**) Force-extension ratio relationship for the two different configurations of the TMP: The initial extension ratio of 0.71 and 0.73. The inset illustration shows the shape of the the TMP for each extension ratio. (**b**) We numerically examine whether the TMP exhibits the increasing stiffness by changing the angle (α) and the length ratio (d/m). The numerical results are plotted as the phase diagram where the blue region indicates the bi-directional foldable states, whereas, the red is the high stiff configuration.

2.6 Conclusion

In conclusion of this Chapter, we investigated unique kinematics of origami-based 3D structures based on the Tachi-Miura Polyhedron (TMP). We found that the Poisson's ratio of the re-entrant TMP can be tuned to exhibit negative values in bilateral directions under the strains along the stacking direction. Also, the re-entrant TMP can exhibit force-displacement relationships in contrast to normal TMP configurations. The findings in this study can form a foundation in designing and constructing a new type of mechanical metamaterials, which feature controllable auxeticity and structural stiffness. These 3D cellular structures offer an enhanced degree of freedom in structural responses, showing great potentials for various engineering applications such as space structures and impact absorbers.

Chapter 3

STATIC MECHANICAL RESPONSE OF THE TCO

In this Chapter, we investigate the mechanics of volumetric origami, specifically triangulated cylindrical origami (TCO), which can develop coupled dynamics of axial and rotational motions during folding (Fig. 3.1a). Despite its simplicity, we find a rich tunability and expandability it offers for the construction of mechanical computing units. The tunability of the TCO can be achieved in two different ways, 1) altering its initial geometry and 2) applying pre-compression, and we demonstrate the tunable behavior from single unit cell level to multi-cell level.

3.1 Modeling of the TCO structure

The TCO consists of repeating triangular arrays, which are characterized by valley crease lines (length a) and mountain crease lines (length b) as shown in Fig 3.1b. Top and bottom surfaces of the TCO unit cell are n-sided polygons (e.g., $n = 5$ in Fig. 3.1) with side length c. Since the TCO is not a rigid foldable origami, folding/unfolding motions cause the warping of each facet, which may result in surface fatigue and damage under repeated usage. To overcome this issue while preserving the key characteristics of the TCO, we replace its surfaces with purely elastic truss members, which support tension/compression by using linear springs (Fig. 3.1c). If we assume that the top and bottom surfaces are always parallel during folding/unfolding, we can characterize the shape of the unit cell by defining its height (h), relative angle between the top and bottom polygons (θ), and radius of the circle circumscribing the polygon (R). Note that for the sake of mathematical simplicity, θ is defined as an angle between OB and the perpendicular bisector of A_aA_b as shown in the

---

The texts and figures in this Chapter have been partly taken from the author's publication [48].

top view of Fig 3.1c. Letting h_0 and θ_0 be the initial height and relative angle respectively, we can express deformations of the structure by axial displacement $u = -(h - h_0)$ where compression is defined to be positive, and rotational angle $\varphi = \theta - \theta_0$.

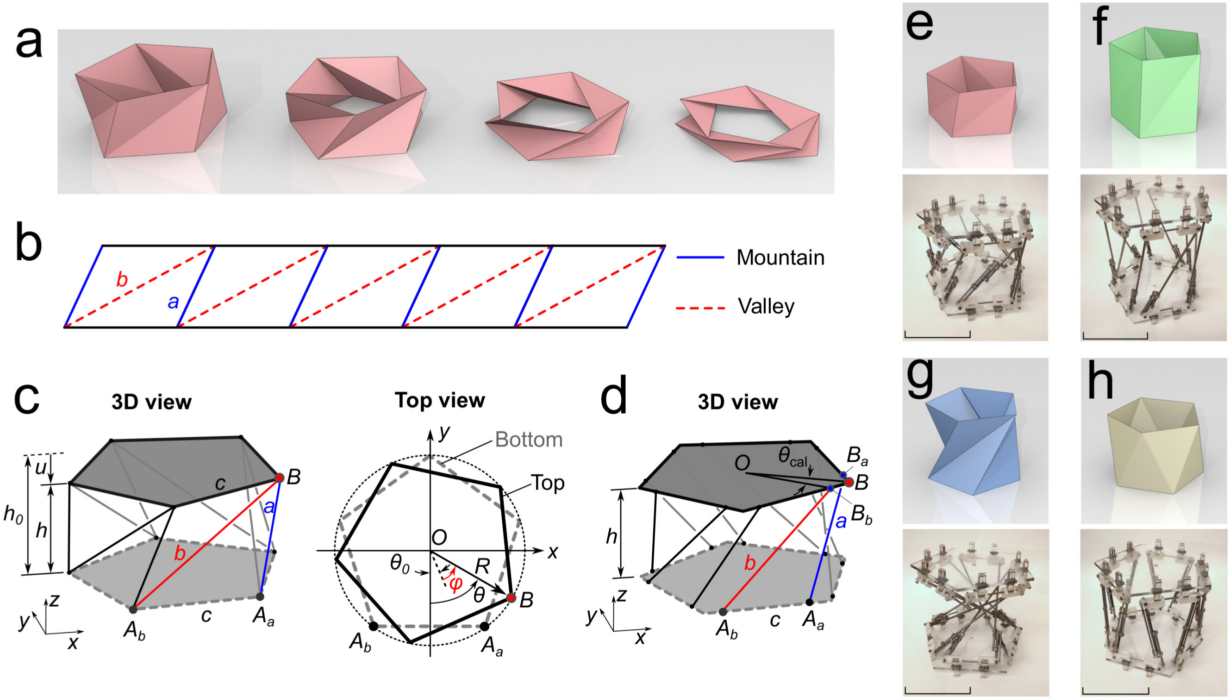

Figure 3.1: Geometry of triangulated cylindrical origami. (**a**) Folding motion of the TCO. (**b**) The flat sheet with crease patterns consisting of mountain crease lines (a shown as blue solid lines) and valley crease lines (b shown as red dashed lines). (**c**) Truss version of the TCO, where all facets are removed and crease lines are replaced by linear springs with a spring constant of k. (**d**) Modified truss structure for the fabrication of physical prototypes. (**e-h**) Graphical illustrations of four different TCO configurations (upper row) and digital images of their physical prototypes (lower row). Their initial configurations are $(h_0, \theta_0) =$ (90 mm, 46°), (150 mm, 40°), (140 mm, 92°), and (119 mm, 0°) from left to right.

In this truss model, two crease lines a and b are intersecting at a vertex of the polygon (e.g., B in Fig. 3.1c). For the fabrication of this truss model, we need to secure space for mechanical joints. Thus, we modify the geometry of the TCO model, such that the two crease lines avoid intersecting (Fig. 3.1d). The difference between the original (Fig. 3.1c) and modified (Fig. 3.1d) models is characterized by the correction of the relative angle (θ_{cal} in Fig. 3.1d).

By using this modified model, we fabricate, test, and analyze four different types of the TCO structures by changing h_0 and θ_0. Figure 3.1e-h show the graphical illustration of these four original models (top row) and the digital images of their modified physical prototypes (bottom row): $(h_0, \theta_0) =$ (90 mm, 46°), (150 mm, 40°), (140 mm, 92°), and (119 mm, 0°). In these models, we use $R = 90$ mm and $\theta_{cal} = 9.7°$.

3.2 Potential energy analysis

To analyze the static mechanical response of the TCO unit cell, we derive the expressions for axial force and torque as a function of u and φ by employing the principle of minimum potential energy. First we consider the TCO model without the modification for the sake of simplicity, and then, we implement the correction angle θ_{cal} in our analysis tool. Our analysis is based on the potential energy, and to calculate the energy, we derive the expressions of the length change of crease lines a and b, as the TCO cell experiences axial and angular deformations. By examining the geometry of the modified TCO as shown in Fig. 3.2, the distance between vertex A_a (A_b) and D are expressed by

$$\begin{aligned} L_a &= 2R\sin\left(\frac{\theta}{2} - \frac{\pi}{2n}\right) \\ L_b &= 2R\sin\left(\frac{\theta}{2} + \frac{\pi}{2n}\right). \end{aligned} \tag{3.1}$$

Also, from the geometry of the TCO (see Fig. 3.2b), we obtain

$$\begin{aligned} L_a^2 + h^2 &= a^2 \\ L_b^2 + h^2 &= b^2, \end{aligned} \tag{3.2}$$

Substituting Eq. (B.1) into Eq. (3.2), we can calculate the length of each crease lines as follows:

$$a = \sqrt{(h_0 - u)^2 + 4R^2 \sin^2\left(\frac{\varphi}{2} + \frac{\theta_0}{2} - \frac{\pi}{2n}\right)}, \qquad b = \sqrt{(h_0 - u)^2 + 4R^2 \sin^2\left(\frac{\varphi}{2} + \frac{\theta_0}{2} + \frac{\pi}{2n}\right)}. \tag{3.3}$$

Here, it is noted that the maximum limit of the rotational angle (φ_{max}) is determined by

$$\varphi_{max} = \left(\pi - \frac{\pi}{n}\right) - \theta_0. \tag{3.4}$$

If $\varphi = \varphi_{max}$, the crease lines intersect each other, limiting the maximum axial and angular deformation of the TCO cell.

Based on Eq. (3.3), the total elastic energy is calculated as

$$U = \frac{1}{2} nk(a - a_0)^2 + \frac{1}{2} nk(b - b_0)^2, \tag{3.5}$$

where a_0 and b_0 are initial length of a and b, and k is a spring constant of the truss members. Here we assume that all truss members exhibit identical axial stiffness. Also, the work done on this system is

$$W = Fu + T\varphi, \tag{3.6}$$

where F and T are the external force and torque respectively. Then, by using the expressions of the elastic energy and work in Eq. (3.5) and Eq. (3.6), the total potential energy (Π) can be expressed as:

$$\Pi(u, \varphi) = U - W = \frac{1}{2} nk(a - a_0)^2 + \frac{1}{2} nk(b - b_0)^2 - Fu - T\varphi. \tag{3.7}$$

We apply the principle of minimum total potential energy (i.e., $\delta\Pi = 0$) to Eq. (3.7) as follows:

$$\partial\Pi/\partial u = 0 \quad \text{and} \quad \partial\Pi/\partial\varphi = 0. \tag{3.8}$$

As a result, we obtain expressions of F and T in terms of u and φ as follows:

$$\begin{aligned} F(u,\varphi) &= nk\left(u-h_0\right)\left(2-\frac{a_0}{a}-\frac{b_0}{b}\right), \\ T(u,\varphi) &= nkR^2\left\{\left(1-\frac{a_0}{a}\right)\sin\left(\varphi+\theta_0-\frac{\pi}{n}\right)+\left(1-\frac{b_0}{b}\right)\sin\left(\varphi+\theta_0+\frac{\pi}{n}\right)\right\}. \end{aligned} \tag{3.9}$$

Next, we modify this TCO model according to the necessity of the modification from fabrication aspect. In the original TCO model, axial truss members a and b intersect at vertices that are positioned on the surface of interfacial polygons (see Fig. 3.2a). Such intersecting joints are not easy to fabricate, when we build a prototype with mechanical joints. Thus, to secure enough space for mechanical joints that connect axial members to the interfacial polygons, we modify the original TCO model. Specifically, we separate a single vertex (e.g., B in Fig. 3.2a) into a pair of vertices (e.g., B_a and B_b in Fig. 3.2b). The difference between the original model and the modified model can be characterized by a shifted angle of the vertices (θ_{cal} in the 3D view of Fig. 3.2b) and a modified radius of these vertices (R' in the top view of Fig. 3.2b).

We can reflect these modifications in Eq. (3.3) as follows:

$$\begin{aligned} a &= \sqrt{(h_0-u)^2+4R'^2\sin^2\left(\frac{\varphi}{2}+\frac{\theta_0}{2}-\frac{\pi}{2n}+\theta_{\text{cal}}\right)} \\ b &= \sqrt{(h_0-u)^2+4R'^2\sin^2\left(\frac{\varphi}{2}+\frac{\theta_0}{2}+\frac{\pi}{2n}-\theta_{\text{cal}}\right)} \end{aligned} \tag{3.10}$$

where

$$R' = \frac{R\cos\left(\frac{\pi}{n}\right)}{\cos\left(\frac{\pi}{n}-\theta_{\text{cal}}\right)}. \tag{3.11}$$

Then, Eq. (3.9) also needs to be modified accordingly as follows:

$$\begin{aligned} F(u,\varphi) &= nk\left(u-h_0\right)\left(2-\frac{a_0}{a}-\frac{b_0}{b}\right) \\ T(u,\varphi) &= nk(R')^2\left\{\left(1-\frac{a_0}{a}\right)\sin\left(\varphi+\theta_0-\frac{\pi}{n}+2\theta_{\text{cal}}\right)+\left(1-\frac{b_0}{b}\right)\sin\left(\varphi+\theta_0+\frac{\pi}{n}-2\theta_{\text{cal}}\right)\right\}. \end{aligned} \tag{3.12}$$

Note that a and b in Eq. (3.12) are based on the expressions in Eq. (3.10), which include the modification parameters θ_{cal} and R'. In this Chapter, the computation results of the TCO's folding behavior are based on this modified model.

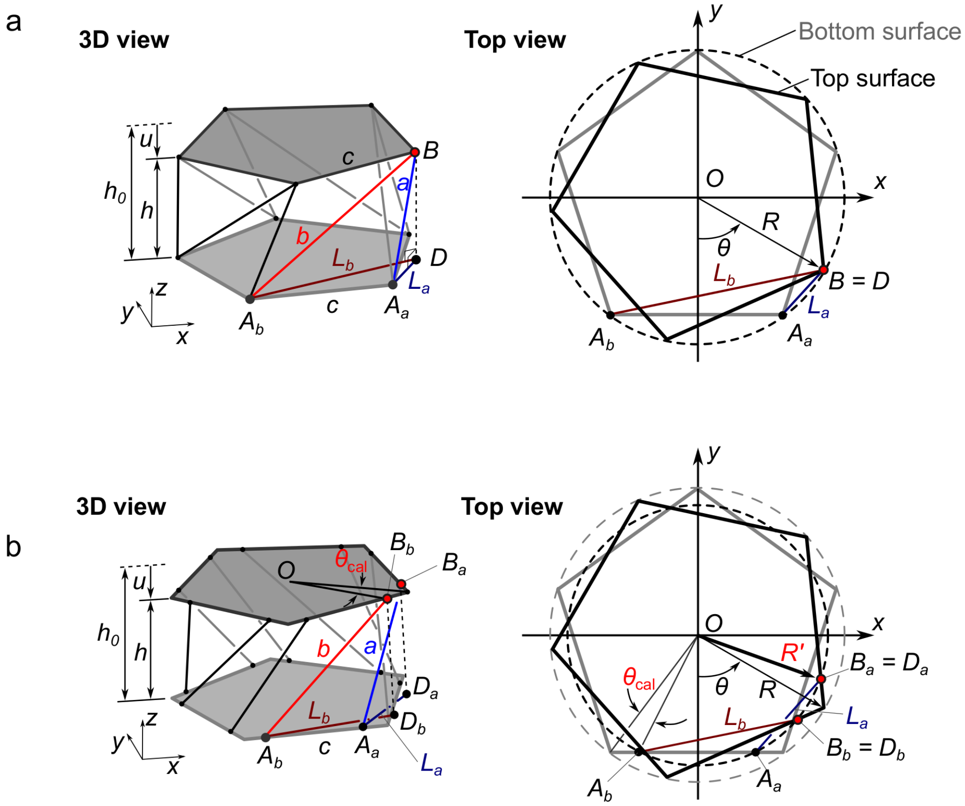

Figure 3.2: Original and modified TCO model. (**a**) 3D (left) and top (right) views of the original TCO unit cell are shown. (**b**) We modify the geometry of the TCO by separating a single vertex (e.g., B in (**a**)) into two vertices (e.g., B_a and B_b in (**b**)). The differences between the original TCO model and modified TCO model are characterized by θ_{cal} and R'.

3.3 Compression test on single unit cells

3.3.1 Force-displacement relationship

In this study, we conduct a series of compression tests on the fabricated TCO prototypes. Figure 3.3a shows a unit-cell prototype placed horizontally on the load frame. In this setup, the right end of the prototype is fixed in both translational and rotational directions. The polygon on the left side is supported by a stainless steel shaft. We use a ball bearing to grab the shaft at the tip, so that the left polygon can rotate freely with minimal friction. The other end of the shaft is connected to the motor-driven linear stage (BiSlider, Velmex). We control the axial compression of the prototype by translating the shaft along the horizontal direction (see the arrow in Fig. 3.3a). Note that by using this shaft system, we apply a desired compression to the system, while allowing free rotational motions and restricting any bending motions of the prototype. The axial force transmitted through the shaft is measured by a force sensor located between the right tip of the shaft and the linear stage (LUX-B-50N-ID, Kyowa).

By using the compression test setup, we obtain force-displacement data. Figure 3.3b shows the measured force-displacement curves (dashed curves) for $(h_0, \theta_0) = (90\text{ mm}, 46°)$ denoted as red color, (150 mm, 40°) denoted as green color, and (140 mm, 92°) denoted as blue color. The corresponding analytical results are also shown in solid curves. As noted in the main text, these curves show remarkably different behaviors, depending on the choice of the TCO's geometry in terms of h_0 and θ_0. The model with ($h_0 = 90$ mm, $\theta_0 = 46°$) shows a maximum peak around u/kh_0 of 0.16, and after this maximum peak, the slope of the force-displacement curve becomes negative, i.e., negative stiffness (red curves in Fig. 3.3b). The model with ($h_0 = 150$ mm, $\theta_0 = 40°$) indicates the transition from compressive force to tensile force during folding (green curves in Fig. 3.3b).

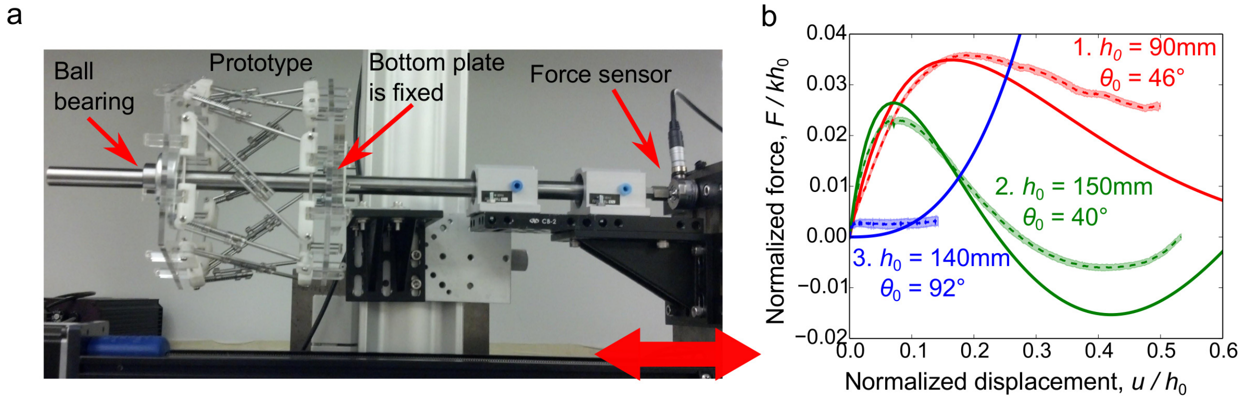

Figure 3.3: Compression test setup and experimental/analytical data. (**a**) The photograph of the compression test setup is shown. The fabricated prototype of the TCO-based truss structure is placed horizontally. The right end of the prototype is fixed, while its left end is attached to a stainless steel shaft via a ball bearing. This allows the left plate to rotate freely with minimal friction. Axial force is measured by a force sensor attached the shaft. (**b**) Dashed curves show measurements of the axial force (normalized by kh_0) as a function of axial compression (normalized by h_0) for three different prototypes, which represent monostable, bistable, and zero-stiffness configurations. Shaded areas represent standard deviations of the measured data. Solid curves show predictions from the potential energy analysis.

Lastly, for the zero-stiffness model, the measurement indicates that the slope of the force-displacement is nearly zero at the initial stage (blue curves in Fig. 3.3b). This zero-stiffness effect is more evident if we zoom up the region near $u/h_0 = 0$ (Fig. 3.4). By applying the linear approximation to the measurements between $u/h_0 = 0.01$ and 0.03, we can compare the slope of the force-displacement curves among the different prototypes (see the solid lines in Fig. 3.4 for the linearization). The reason that we apply the linearization not from $u/h_0 = 0$ is due to the static friction in the mechanical joints (see the initial force required to overcome this friction in all curves in Fig. 3.4). The slope of these non-dimensionalized graphs are 0.326, 0.479, and 0.000861 for monostable, bistable, and zero-stiffness cases, respectively. The slope of this zero-stiffness case corresponds to mere 0.26% and 0.18% compared to the monostable and bistable cases. This successfully verifies the feasibility of zero-stiffness structure using this TCO architecture, making it potentially applicable for impact mitigation purposes.

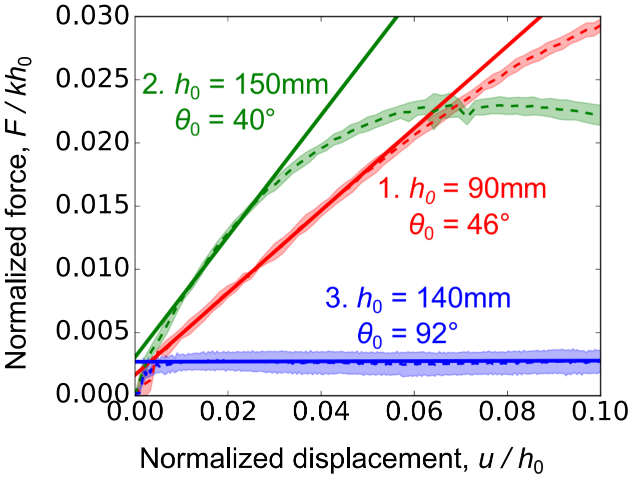

Figure 3.4: Force-displacement curves for the comparison of stiffness. We zoom up the force-displacement measurements from the three prototypes near $u/h_0 = 0$. The solid lines are based on the linear approximation of the experimental data in the range between $u/h_0 =$ 0.01 and 0.03. It is evident that the zero-stiffness case exhibits a significantly smaller slope (i.e., stiffness) compared to the other cases.

We also conduct the compression test on the model ($h_0 = 119$ mm, $\theta_0 = 0°$). We consider two experimental setups. The first one is with the constraints on the rotational motion of the prototype (Fig. 3.5a), and the other one is without any constraints (Fig. 3.5b). For application of the constraints on the rotational motion of the prototype, we use a pair of stainless steel shafts and linear bearings, which allow the prototype to translate in the axial direction without any rotational motions (Fig. 3.5a). The setup without any constraints is identical to the test configuration for the other TCO unit cells.

Figure 3.5c shows the experimental results (dashed curves) and analytical predictions (solid curves). In the unstable case (red curves indicated by arrow 4), the axial force increases monotonically from $u/h_0 = 0$ to 0.1. As shown in the inset, the TCO cell compresses without twisting motions. This unstable mode is possible only if there exist constraints that prevent any onset of rotational motions. On the other hand, if the constrains are removed, the measurement shows a kink point where the slope of the force-displacement curve changes to negative (blue curves indicated by arrow 5 in Fig. 3.5c). Note that the TCO cell experiences a twisting motion in one or the other direction after the bifurcation point, as illustrated by the inset. We observe noticeable discrepancies between the experimental and analytical results, particularly in terms of the bifurcation point. Again, this is probably due to the friction existing in the prototypical systems.

Overall, the force-displacement curves obtained from the compression tests are in qualitative agreement with the analytical predictions (Fig. 3.3b). The discrepancy between the experimental and analytical data may be attributed to the friction in the mechanical joints of the prototypes. In fact, the application of grease to these joints significantly improved the quality of the experimental data, particularly in the earlier part of the compression tests.

3.3.2 Energy analysis

To understand the folding behavior of the TCO-based structure from the view point of energy analysis, we calculate the total elastic energy (U) stored in the TCO cell as a function of u and φ. We numerically integrated the force-displacement curves obtained from the experiment

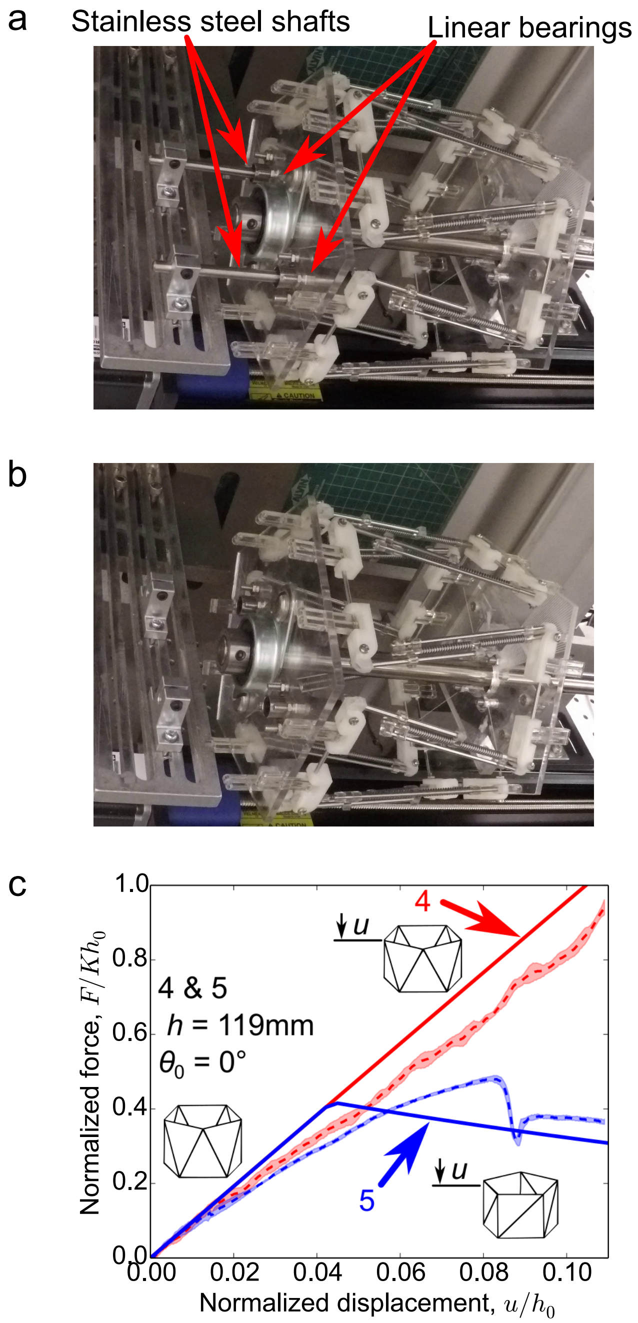

Figure 3.5: Bifurcation test setup and experimental/analytical data. (**a**) The photograph shows the compression test setup with constraints on the rotational motion of the left plate of the prototype. Two stainless steel shafts and linear bearings are used to allow the translational motion without triggering the rotational motion. (**b**) The test setup without constraints on the rotational motion is shown. (**c**) Force-displacement measurements for the two cases show a bifurcation behavior. Here, dashed and solid curves indicate the measured experimental results and the predictions from the energy analysis, respectively. The arrows 4 and 5 indicate the unstable and stable cases respectively.

and presented the total energy profiles. The insets of Fig. 3.6a-d show the surface maps of U for the four models, where dark colored region indicates the valley of the minimum energy level. Simultaneously compressive and rotational motions of the TCO will follow this trajectory to satisfy the minimum potential energy principle. We can also identify the change of the normalized energy (U/kh_0^2 where k is the elastic constant of the linear truss element) under non-dimensionalized axial compression (u/h_0) by imposing $\partial U/\partial\varphi = 0$. Figure 3.6a-d shows the energy plots, where solid curves denote analytical results predicted by the minimum potential energy trajectory in the inset surface maps. The experimental measurements (dashed curves) corroborate these analytical results. Comparing the four plots in Fig. 3.6a-d, we observe remarkably different trends: monostable, bistable, zero-stiffness, and bifurcation behaviors, respectively. If (h_0, θ_0) = (90 mm, 46°), the structure possesses only one minimum energy state at $u = 0$ (Fig. 3.6a). Therefore, the total energy increases monotonically as the TCO cell is compressed, implying a monostable property. If (h_0, θ_0) = (150 mm, 40°), there exist two local minimum states along the energy valley as shown in Fig. 3.6b, indicating bistability.

The TCO-based structure can also exhibit an infinitesimally small stiffness, so called zero-stiffness mode, in which the application of axial compression does not create significant axial force or torque at the initial stage. Therefore, the total energy increases at an extremely low rate around $u = 0$ (Fig. 3.6c). The discrepancy between the analytical and experimental results attributes to the friction of the mechanical joints in the truss elements. Nonetheless, we observe much smaller stiffness in this model compared to the previous two cases.

Here we mathematically derive how to meet the zero-stiffness condition using the truss-based TCO architecture. We first linearize Eq. (3.3) around the undeformed, initial state ($u = \varphi = 0$):

$$\begin{aligned} a &\approx a_0 + \alpha_u u + \alpha_\varphi \varphi \\ b &\approx b_0 + \beta_u u + \beta_\varphi \varphi, \end{aligned} \tag{3.13}$$

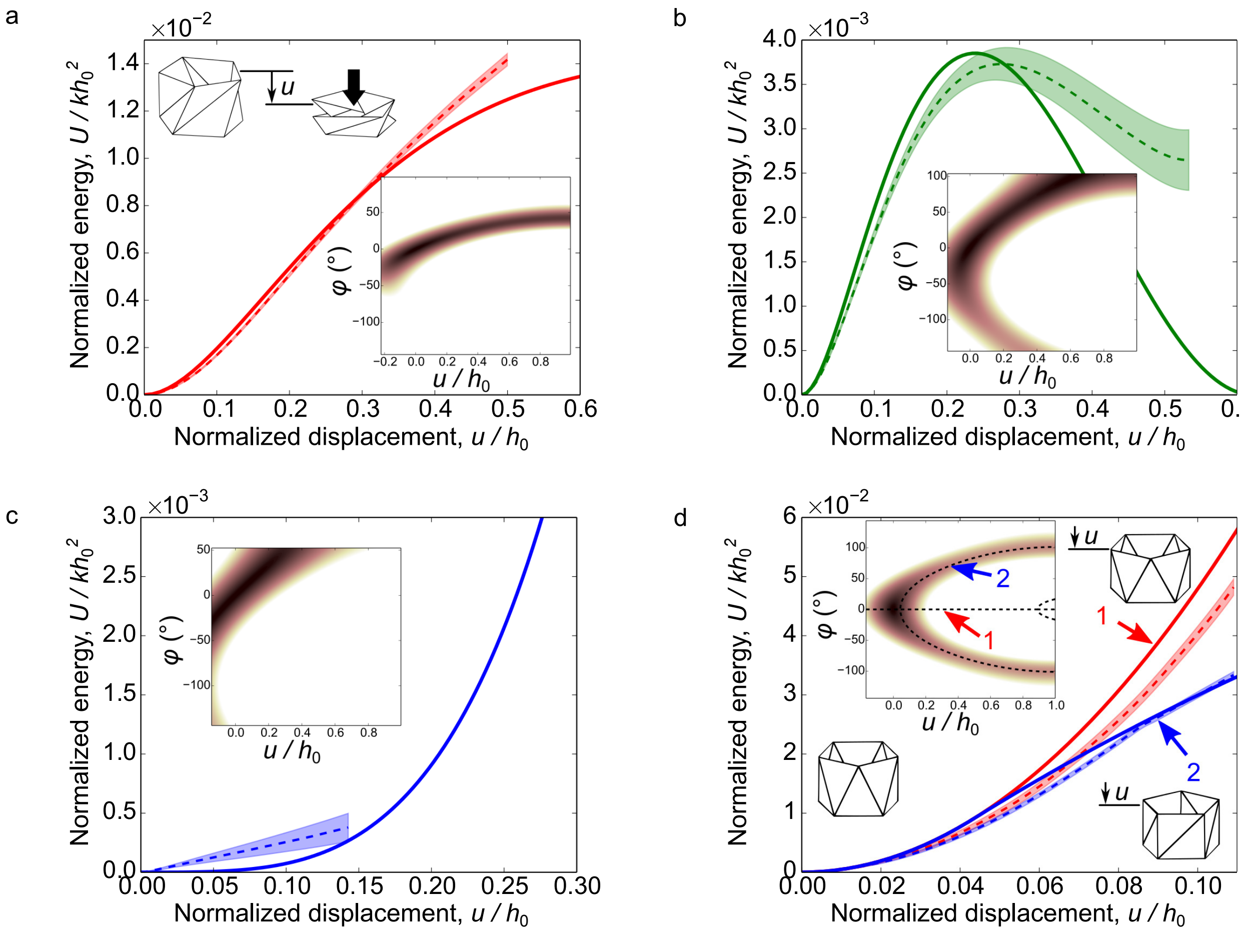

Figure 3.6: Folding motions of the TCO cells. (**a-d**) The energy analysis for the TCO-based truss structures shows remarkably different behaviors: (**a**) Monostability at $(h_0, \theta_0) = (90$ mm, 46°); (**b**) bistability at (150 mm, 40°); (**c**) zero-stiffness mode at (140 mm, 92°); and (**d**) bifurcation at (119 mm, 0°). The displacement is normalized by h_0, and energy is normalized by kh_0^2. Experimental results (mean value is shown as dashed curves, and standard deviation is represented by colored areas) show qualitative agreements with the analytical predictions (solid curves). The inset plots show the equi-potential plots of U/kh_0^2 as a function of u/h_0 and φ, in which highlighted trajectories indicate the valley of minimum potential energy. In the experimental curves, the range of u/h_0 is restricted by the folding motions of the TCO-based truss prototypes. For example, the highly twisted shape of the zero-stiffness TCO prototype (Fig. 3.1g) causes the truss elements overlap in the early stage of folding, allowing only ∼15% of u/h_0 as shown in the panel (**c**). The moderately twisted geometry of the monostable and bistable cases (Figs. 3.1e and f) permit more compression, allowing approximately 50% folding of the truss structure in terms of u/h_0 as shown in the panels (**a**) and (**b**).

where a_0 and b_0 are initial length of a and b respectively, and

$$\begin{aligned}\alpha_u &= -\frac{h_0}{a_0}\\ \alpha_\varphi &= \frac{R^2 \sin\left(\theta_0 - \pi/n\ \right)}{a_0}\\ \beta_u &= -\frac{h_0}{b_0}\\ \beta_\varphi &= \frac{R^2 \sin\left(\theta_0 + \pi/n\ \right)}{b_0}.\end{aligned} \tag{3.14}$$

After the linearization, Eq. (3.13) can be expressed in a matrix form as

$$\boldsymbol{e} \approx \boldsymbol{A\xi} \tag{3.15}$$

where

$$\begin{aligned}\boldsymbol{A} &= \begin{bmatrix}\alpha_u & \alpha_\varphi\\ \beta_u & \beta_\varphi\end{bmatrix},\\ \boldsymbol{e} &= \begin{bmatrix}a - a_0\\ b - b_0\end{bmatrix},\\ \boldsymbol{\xi} &= \begin{bmatrix}u\\ \varphi\end{bmatrix}.\end{aligned}$$

Here, $\boldsymbol{e}$ represents the length change of the crease lines, a and b. To fulfill the zero-stiffness condition, the length change of the crease lines (i.e., $\boldsymbol{e}$) need to be infinitesimal given external excitations (i.e., $\boldsymbol{\xi}$). Mathematically, this implies $\det \mathbf{A} = \alpha_u\beta_\varphi - \alpha_\varphi\beta_u = 0$. By using the definitions of the coefficients in Eq. (3.14), we obtain

$$\sin\left(\frac{\pi}{n}\right)\cos\left(\theta_0\right) = 0 \tag{3.16}$$

This means, if the initial angle (θ_0) is $\pi/2$, $\det \mathbf{A}$ becomes zero, which leads to the zero-stiffness mode. Note that this condition can be also met by having $n \to \infty$. Thus, a TCO cell with a large number of truss members that connect the top and bottom polygons (i.e., polygons with numerous vertices) will also exhibit a small stiffness under compression. It should be noted that Eq. (3.16) contains only θ_0 and n. Therefore, the zero-stiffness mode is not affected by the spring constant of the truss members (k) or the initial height of the TCO cell (h_0).

Lastly, we observe that the TCO-based truss can experience bifurcation if $\theta_0 = 0$ (Fig. 3.6d). That is, in the initial stage of the folding, the TCO-based structure is axially compressed without rotation. However, if it reaches a bifurcation point, there are three branches: one unstable branch (continuing pure compression without rotation as indicated by arrow 1 in Fig. 3.6d) and two stable branches (starting to develop twisting motions in one or the other direction as pointed by arrow 2 in Fig. 3.6d). The two different trends in the uni-axial testing verify this bifurcation behavior (Fig. 3.6d).

Overall, we observe versatile nature of the TCO-based truss structure as we alter its geometry. Particularly, the stability of the system can be manipulated by changing its two geometrical parameters: initial twist angle (θ_0) and height (h_0). To examine such tunable stability of the TCO-based unit cell, we numerically analyze its stability for various initial configurations. The process is as follows. We first calculate the elastic energy (U) as a function of axial compression (u) by following the trajectory of the minimum energy valley (e.g., see Fig. 3.6). Then, the slope of this energy curve is numerically obtained by using $(U_{i+1} - U_i)/(u_{i+1} - u_i)$, where i represents a step for numerical calculations. If the TCO-based structure exhibits the bistable behavior, there exists a transition from a positive to negative slope. Thus, we can judge whether the unit cell shows monostable or bistable behavior.

The results are shown in Fig. 3.7. We evidently observe monostable and bistable regions. We also mark lines that represent zero-stiffness ($\theta_0 = 90°$) and bifurcation ($\theta_0 = 0°$) modes in the investigation range. Note that the zero-stiffness mode is located at the boundary between the monostable and bistable regions. In the bistable regions, there exist two stable states, and these two stable states merge at this boundary as the initial angle (θ_0) increases. The four prototypes that we fabricate are also marked as circles in the figure.

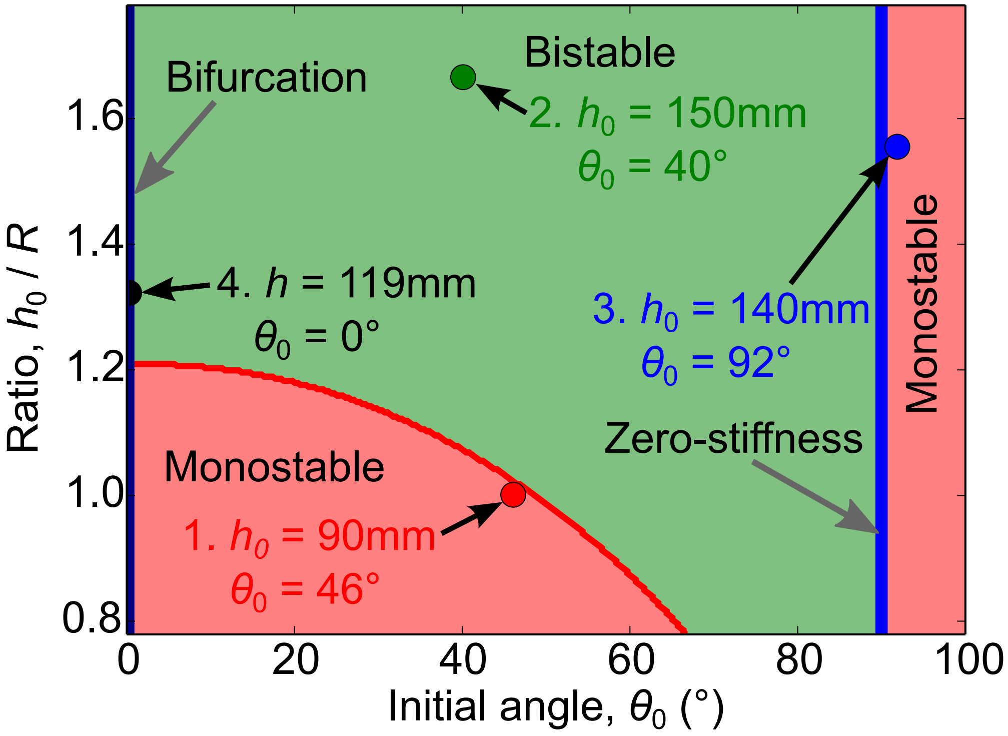

Figure 3.7: Tunable behavior of the TCO. Tunable behavior of the TCO-based unit cell is examined numerically in various combinations of initial configurations (i.e., h_0 and θ_0). We use $\theta_{\mathrm{cal}} = 9.7°$ for all calculations. Red and green regions indicate monostable and bistable behaviors respectively. If $\theta_0 = 90°$ (blue solid line), the unit cell shows the zero-stiffness mode. The black solid line ($\theta_0 = 0°$) indicates that the system shows the bifurcation behavior in the investigation range of the height ratio.

3.4 *In-situ potential energy map*

In the previous section, we manipulate the static mechanical response of the TCO unit cell by controlling the initial geometrical parameters. Here, we show that the stability of the unit cell, i.e., elastic energy map, can be tuned even after those initial geometrical parameters are determined. Using the TCO-based truss structure as a unit cell, we further investigate the folding mechanism of multi-cell structures composed of stacked TCO cells. We study a two-cell structure that consists of identical monostable TCO units with $(h_0, \theta_0) = (90\text{ mm}, 46^\circ)$. They are linked together by sharing the interfacial polygon (Fig. 3.9a). Note that the chirality of the TCO cells is important in the multi-cell architectures. In this two-cell level, we arrange the cells in the opposite chirality, i.e., $(h_0, \theta_0) = (90\text{ mm}, \pm 46^\circ)$, such that they collectively show an interesting coupling motion. To test the dynamics of the combined structure, we fix the right end of the stacked prototype to the wall and impose precompression $u_C = 45$ mm to the left end of the system (Fig 3.8).

Then, the total elastic energy of the system will differ depending on the rotational angles of the two unit cells, characterized by φ_1 and φ_2. Note that these angles are measured with respect to the initial positions of the left and central polygons, respectively. The inset of Fig. 3.9b shows the analytical values of U as a function of φ_1 and φ_2, where the highlighted zone represents the valley of the minimum potential energy. We find that the pair of TCO cells collectively possess two local minimum states: one with the right cell folded and the other with the left cell folded (see the graphical illustrations in the inset of Fig. 3.9b). The normalized elastic energy can be re-plotted as a function of φ_1 by imposing $\partial U/\partial \varphi_2 = 0$. Figure 3.9b evidently shows a symmetric double-well potential. This demonstrates that a pair of monostable TCO cells can successfully form a bistable system, requiring energy to overcome the potential barrier for the transition between the two stable states. Please note that this potential barrier can be manipulated by controlling precompression, i.e., tunable potential barrier.

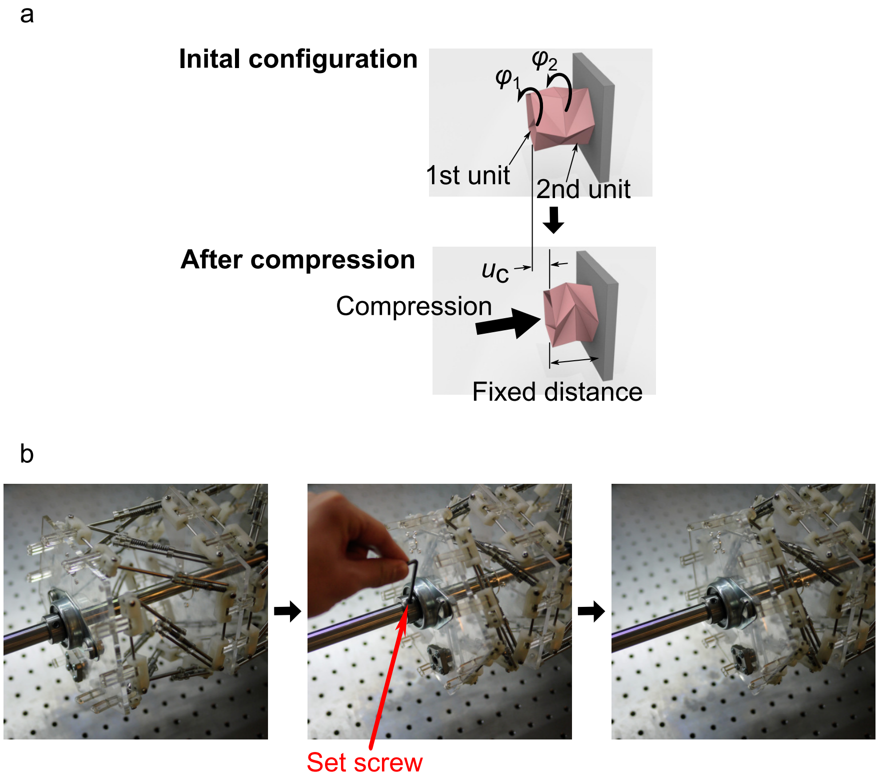

Figure 3.8: Application of precompression to a two-cell structure. (**a**) Two monostable TCO-based unit cells (h_0 = 90 mm, θ_0 = ±46°) are connected horizontally as shown in the schematic illustration. The upper panel illustrates the initial configurations under no external force and torque. We apply pre-compression to this system (denoted by u_C), and we fix the distance between leftmost and rightmost plates as shown in the lower panel. The rotation of the leftmost surface of the system is φ_1 measured with respect to its initial configuration. (**b**) Photographs show the preparation of the system with pre-compression by tightening a set screw of the bearing which is attached to the cross-section of the TCO-based unit cell.

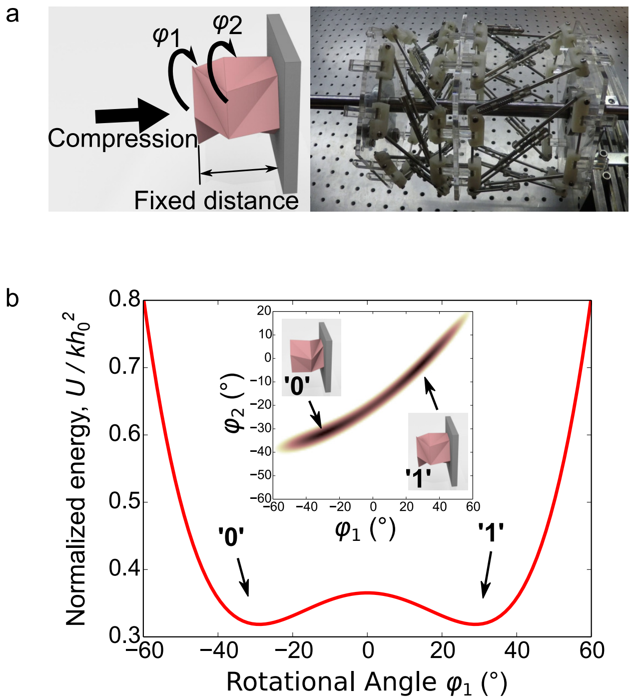

Figure 3.9: A pair of TCO cells' capability to demonstrate in-situ double well potential. (**a**) Two monostable TCO-based unit cells are connected horizontally. We fix the distance between leftmost and rightmost polygons by imposing a constant distance between them. Photograph of the corresponding configuration is shown in the right panel. (**b**) The normalized elastic energy as a function of φ_1 shows the double-well potential numerically. The inset shows the surface map of the elastic energy as a function of both φ_1 and φ_2, where the highlighted region denotes the valley of the map corresponding to the minimum potential energy trajectory. There exist two minimum states, and the illustrations show the schematic shapes of the pair of TCO cells at these points.

One of the potential applications of this in-situ double well potential is a mechanical memory device. Let ‘1’ be the state where the first unit cell is folded, and ‘0’ be the state where the second unit cell is folded. Then we can use this system as a non-volatile mechanical memory device, which can store bit information (‘1’ or ‘0’) by exploiting the double-well potential. One advantage of this mechanical memory is that it can store bit information stably without the necessity of external residual force. To change the states from ‘0’ to ‘1’ or vice versa, we control only φ_1 so that the two-unit cell system can switch its state.

For the operation of the single bit, we control the rotation of the leftmost polygon (denoted by φ_1) by applying torque to the polygon (Fig. 3.10a). For the accurate control of the imposed rotational angle, we use a crank system attached to the leftmost polygon of the prototype (Fig. 3.10b). We measure the exact amount of the translational motion (δ) by using a non-contact laser Doppler vibrometer (OFV-505, Polytec), and covert the measurement values to the rotational motion (φ_1). A force sensor (LUX-B-50N-ID, Kyowa) is also attached at the end of the crank arm to calculate the torque applied.

Figure 3.10c shows the experimental measurements (red curve) of the torque and the rotational angle, in comparison to the analytical results (black curve) predicted by the energy analysis. We observe that as we rotate the leftmost polygon (i.e., φ_1 increases), the system changes its state from ‘0’ (i.e., the initial configuration that the right cell is folded) to ‘1’ (i.e., the final configuration that the left cell is folded). This experimental trend agrees well with the prediction from the energy analysis.

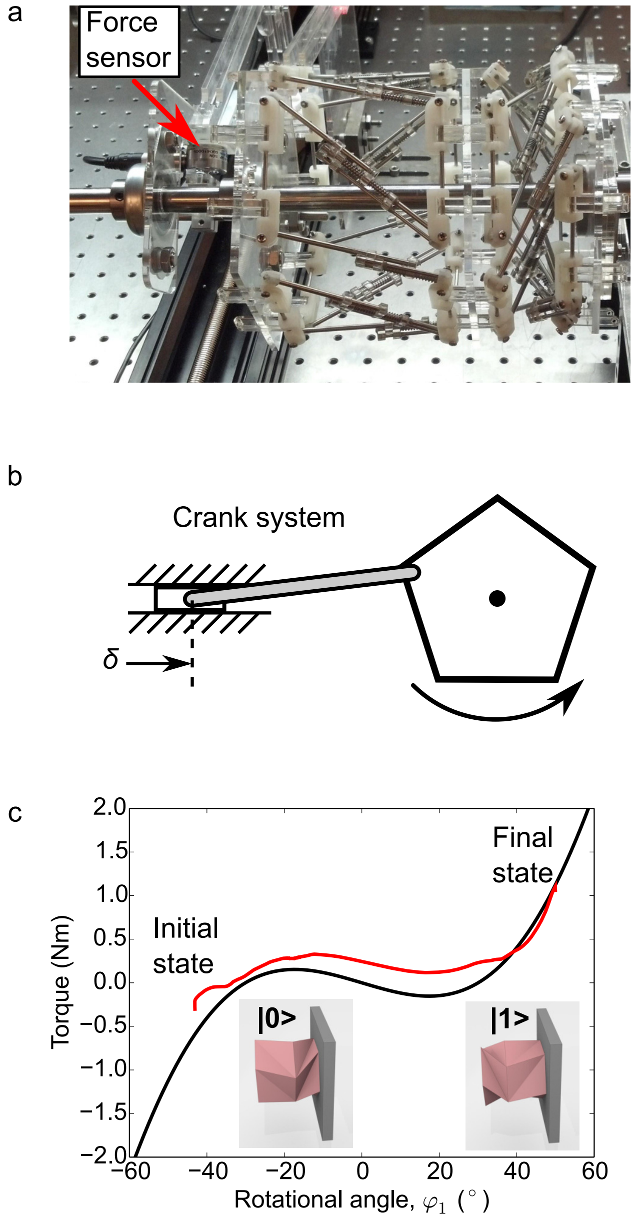

Figure 3.10: Single bit operation for memory storage. (**a**) Photograph shows the test setup for measuring the relationship between torque and φ_1. We obtain the torque information by using the force sensor attached to the crank system, which is operated by the linear stage. (**b**) The crank system is used to convert the translational motion (δ) into the rotational motion. We measure/control δ to impose an accurate amount of the rotation of the system. (**c**) Measurements of the torque as a function of the rotational angle (red curve) show a good agreement with the prediction from the energy analysis (black curve). The insets show the graphical illustrations of the '0' and '1' states.

3.5 Conclusion

We showed the versatile nature and potential of the TCO elements hierarchically from a single-cell to double-cell level. We envision that it can be further extended to multi-dimensions, e.g., honey-comb like 3D clusters. This will function as a layer of mechanical memory storage and computing structures, which can also provide multi-functional features, such as rugged protective layers. Moreover, origami can be scaled to miniaturized dimensions. Therefore, the versatile nature of the TCO together with nanoelectromechanical systems (NEMS) has great potential to develop robust NEMS actuators and sensing devices. Also, the intrinsic nature of the TCO cells that interweave axial and torsional motions can be further exploited for dynamic purposes. Conclusively, the volumetric origami cells can pave a new way for designing novel engineering systems for mechanical computing and other purposes relying on their rich constitutive mechanics in a single-cell level and strong cohesion in a multi-cell level.

Chapter 4

LINEAR WAVE PROPAGATION IN TMP

In this Chapter, we investigate unique wave dynamics in origami-based mechanical metamaterials composed of the Tachi-Miura Polyhedron (TMP) [26, 27] as shown in Fig. 4.1(a). The TMP is known as a rigid foldable origami, which means that it can be made of rigid plates and hinges in order to exhibit unique mechanical properties as we discuss in the Chapter 2. First, we simplify the TMP structure maintaining its rigid foldable feature and derive the equation of motion and force-displacement relationship. By focusing on the axial motion, we linearize the force-displacement relation of the TMP structure. This linear model is also used and compared with the simplified TMP model for the subsequent dynamic analysis.

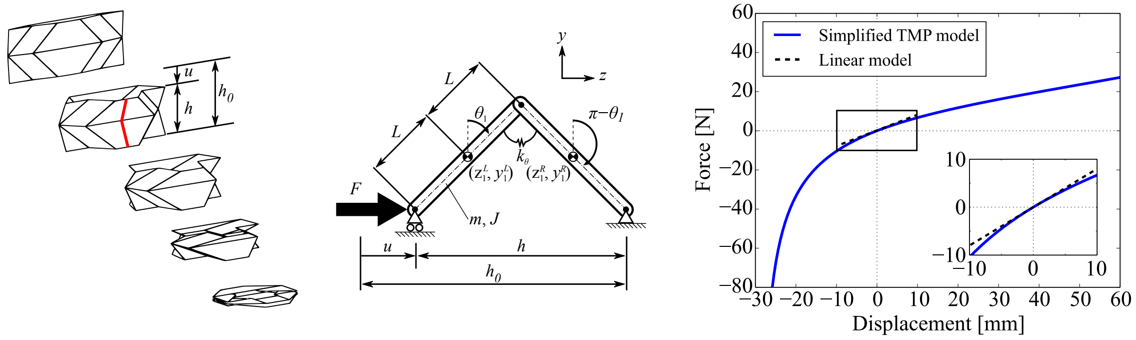

(a) (b) (c)

Figure 4.1: (**a**) Folding motion of the TMP unit cell. (**b**) Simplified TMP model representing the folding motions of the two facets as marked in red lines in (**a**). (**c**) Force-displacement relationship of a single unit cell. Blue solid line is calculated based on the simplified TMP model (Eq. (A.7)), and black dashed line is obtained from the linearized model (Eq. (4.3)). The inset in (**c**) shows the magnified view of the relationship around the equilibrium state.

Based on the simplified TMP model, we conduct dynamic analysis via theoretical and

---

The texts and figures in this Chapter have been partly taken from the author's publication [49].

computational approaches. Specifically, we first apply harmonic excitations to the single unit cell and analyze its frequency response by using the shooting method [50]. Numerical results show that the dynamic responses of the TMP unit cell can be tuned by altering its initial geometrical configurations. Also, depending on the amplitude of the excitation, the system transits from linear to nonlinear regimes or vice versa.

Next, we consider an origami-based mechanical metamaterial composed of a chain of the simplified TMP unit cells. We analyze the dispersion relationship (i.e., frequency and wave number relationship) of mechanical waves propagating through the system. We examine the effect of geometrical parameters on the wave propagation in the 1D chain structure. We find numerically that our 1D chain structure can exhibit versatile wave dynamics by forming tunable frequency band structures. The computational results corroborate analytical dispersion relationship characterized by distinctive cutoff frequencies. This origami-based mechanical system has great potentials to be used as novel engineering devices that are capable of handling vibrations and impact efficiently by leveraging their unique wave dynamics.

4.1 Modeling of TMP Unit Cells and TMP-based Lattices

To analyze dynamical folding/unfolding behavior of the TMP, we simplify it as a bar-linkage model as shown in Fig. 4.1(b). The unit cell of this bar-linkage model consists of two rigid bars connected by a linear torsional spring, whose spring constant is k_θ. In order to maintain the rigid foldability of the TMP, we use a pin joint at the right end of the cell and a roller joint at the left end of the cell. This results in a single degree-of-freedom (DOF) motion along the z-axis, which is consistent with the aforementioned rigid foldability of the TMP. Thus, this linkage model – despite its simplicity – well captures the rigid foldability of the TMP cell, while accounting for its translational and rotational motions simultaneously. It should be also noted that this linkage model can be used in other types of foldable structures (e.g., accordion-like structures), provided that they are rigid origami.

The displacement (u) along z-axis is obtained by $u = 4L\left(\sin\theta_{1,0} - \sin\theta_1\right)$, where θ_1 is the folding angle of the linkage structure and $\theta_{1,0}$ is its initial folding angle. Please note that for the sake of simplicity, the folding angle is defined as an angle between a center line of the bar and vertical line (see Fig. 4.1(b)), which decreases as the model is folded (i.e., as u increases). Let mass, length, and moment of inertia of each bar be m, $2L$, and $J = \frac{mL^2}{3}$, respectively. The equation of motion of this unit cell can be expressed by (see Appendix A for the derivation):

$$\begin{aligned} &\left(2mL^2 + 2J + 8mL^2\cos^2\theta_1\right)\ddot{\theta}_1 - 4mL^2\dot{\theta}_1^2\sin 2\theta_1 \\ &\qquad = -4FL\cos\theta_1 - 4k_\theta\left(\theta_1 - \theta_{1,0}\right). \end{aligned} \tag{4.1}$$

Here, the principle of virtual power [51] is used to derive the above equation of motion. Also, the force-displacement relationship can be expressed as:

$$F = -\frac{k_\theta\left(\theta_1 - \theta_{1,0}\right)}{L\cos\theta_1}, \tag{4.2}$$

where k_θ is the coefficient of the torsional spring at the hinge.

Assuming the displacement (u) is small, we can linearize Eq. (A.7) around equilibrium position ($u = 0$) as follows:

$$F = F|_{u=0} + \left.\frac{dF}{du}\right|_{u=0} u + \cdots \approx K\left(\theta_{1,0}\right)u, \tag{4.3}$$

where

$$K\left(\theta_{1,0}\right) = \frac{k_\theta}{4L^2\cos^2\theta_{1,0}}. \tag{4.4}$$

Therefore, the stiffness of the simplified TMP structure varies depending on the initial folding angle ($\theta_{1,0}$). Figure 4.1(c) shows the comparison between the original TMP model (Eq. (A.7)) and the linearized model (Eq. (4.3)) in the force-displacement relationship along the z-direction. $L = 25$ mm, $k_\theta = 1$ Nm/rad, and $\theta_{1,0} = 45°$ are used for this calculation. Around $u = 0$, the linearized model agrees well with the simplified TMP model.

By using the simplified TMP model as a building block, we design a 1D chain of the origami-based metamaterial, which is composed of $2N$-simplified TMP unit cells, as shown in Fig. 4.2(a). Please note that the original TMP is a 1 DOF structure. Therefore, we use multiple TMP unit cells and separators between them to construct a multi-DOF structure (please see Appendix A). Similarly to the single unit cell, we use pin joints to connect the ends of adjacent unit cells, which are allowed to move along the z-axis. Since each unit cell shows a 1-DOF folding motion, we use θ_j, the folding angle of the j-th unit cell, as the general coordinate $\boldsymbol{q} = \begin{bmatrix}\theta_1 & \cdots & \theta_j & \cdots & \theta_{2N}\end{bmatrix}^T$ to derive the equation of motion for the system (see Appendix A for the detail):

$$\boldsymbol{G}^T\hat{\boldsymbol{M}}\boldsymbol{G}\ddot{\boldsymbol{q}} + \boldsymbol{G}^T\hat{\boldsymbol{M}}\dot{\boldsymbol{G}}\dot{\boldsymbol{q}} = \boldsymbol{G}^T\boldsymbol{f} \tag{4.5}$$

where

$$\begin{aligned}
\hat{\boldsymbol{M}} &= \operatorname{diag}\begin{bmatrix}\hat{\boldsymbol{M}}_1 & \cdots & \hat{\boldsymbol{M}}_{2N}\end{bmatrix}, \\
\hat{\boldsymbol{M}}_j &= \operatorname{diag}\begin{bmatrix}m & m & J & m & m & J\end{bmatrix}, \\
\boldsymbol{G}^T &= \begin{bmatrix}
\boldsymbol{G}_1^T & \boldsymbol{O}_{1\times 6} & \boldsymbol{O}_{1\times 6} & \cdots & \cdots & \cdots & \boldsymbol{O}_{1\times 6} \\
\boldsymbol{g}_2^T & \boldsymbol{G}_2^T & \boldsymbol{O}_{1\times 6} & \cdots & \cdots & \cdots & \boldsymbol{O}_{1\times 6} \\
\vdots & \vdots & \vdots & \vdots & \vdots & \vdots & \vdots \\
\boldsymbol{g}_j^T & \boldsymbol{g}_j^T & \cdots & \boldsymbol{G}_j^T & \boldsymbol{O}_{1\times 6} & \cdots & \boldsymbol{O}_{1\times 6} \\
\vdots & \vdots & \vdots & \vdots & \vdots & \vdots & \vdots \\
\boldsymbol{g}_N^T & \boldsymbol{g}_N^T & \boldsymbol{g}_N^T & \cdots & \cdots & \cdots & \boldsymbol{G}_N^T
\end{bmatrix}, \\
\boldsymbol{G}_j^T &= \begin{bmatrix}-3L\cos\theta_j & -L\sin\theta_j & 1 & -L\cos\theta_j & -L\sin\theta_j & -1\end{bmatrix}, \\
\boldsymbol{g}_j^T &= \begin{bmatrix}-4L\cos\theta_j & 0 & 0 & -4L\cos\theta_j & 0 & 0\end{bmatrix}, \\
\boldsymbol{O}_{1\times 6} &= \begin{bmatrix}0 & 0 & 0 & 0 & 0 & 0\end{bmatrix}.
\end{aligned}$$

Also, $\boldsymbol{f}$ is a force vector defined as follows

$$\boldsymbol{f} = \begin{bmatrix}\boldsymbol{f}_1 & \cdots & \boldsymbol{f}_j & \cdots & \boldsymbol{f}_{2N}\end{bmatrix}^T \tag{4.6}$$

where

$$\boldsymbol{f}_j = \begin{cases}
[F, \;\; 0, \;\; -2k_\theta\left(\theta_1 - \theta_{1,0}\right) - FL\cos\theta_1, & \\
\quad 0, \;\; 0, \;\; -2k_\theta\left(\theta_{1,0} - \theta_1\right)] & \text{if } j = 1 \\
[0, \;\; 0, \;\; -2k_\theta\left(\theta_j - \theta_{j,0}\right), & \\
\quad 0, \;\; 0, \;\; -2k_\theta\left(\theta_{j,0} - \theta_j\right)] & \text{if } j = 2\ldots 2N
\end{cases}$$

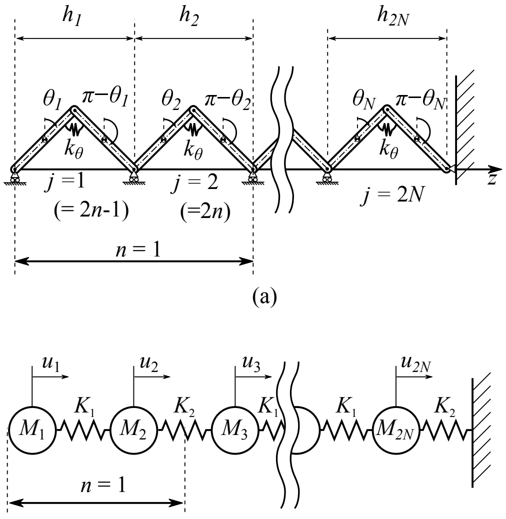

(a)

(b)

Figure 4.2: (**a**) 1D chain composed of the simplified TMP unit cells. (**b**) Lumped mass model.

By using the linearized model expressed by Eq. (4.3), we also consider a 1D chain model consisting of lumped masses and linear springs (see Fig. 4.2(b)). Each lumped mass ($M = 2m$) is connected by a linear spring whose spring constant is calculated by Eq. (4.4). If the identical initial folding angle ($\theta_{j,0}$) is used for all unit cells, the stiffness is also the same at each particle's interface. The equation of motion of the j-th particle is

$$M\ddot{u}_j = K\left(u_{j+1} + u_{j-1} - 2u_j\right). \tag{4.7}$$

By using the ansatz $u_j = ue^{i(kjh_0 - \omega t)}$ where ω and k are angular frequency and wave number, we obtain the dispersion relationship for the linearized 1D chain model as

$$\omega = \sqrt{4\frac{K}{M}\sin^2\left(\frac{kh_0}{2}\right)} \tag{4.8}$$

where h_0 is the initial distance between two adjacent particles.

If the initial folding angles vary from unit cell to unit cell, the inter-particle stiffness should be also modified accordingly. Here, we consider two different types of unit cells

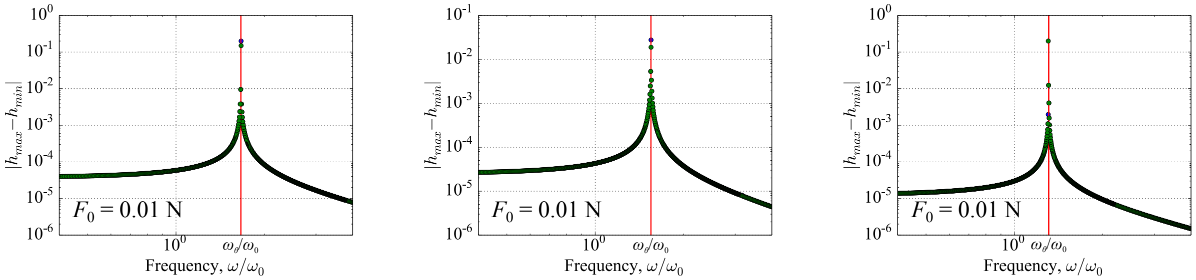

(a) $\theta_{j,0} = 30°$ (b) $\theta_{j,0} = 45°$ (c) $\theta_{j,0} = 60°$

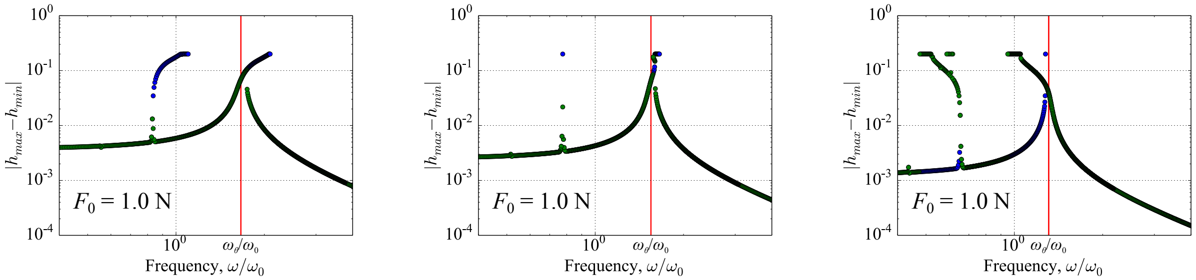

(d) $\theta_{j,0} = 30°$ (e) $\theta_{j,0} = 45°$ (f) $\theta_{j,0} = 60°$

Figure 4.3: Frequency responses of a TMP unit cell. (**a-c**) Excitation with $F_0 = 0.01$ N is applied to the simplified TMP unit cell with $\theta_{j,0} = 30°$, $45°$, and $60°$, respectively, and (**d-f**) $F_0 = 1.0$ N. The frequencies are normalized by $\omega_0 = \sqrt{K/M}$. Blue circles represent solutions obtained numerically by searching from low to high frequency, and green circles are obtained from high to low frequency. Red lines are calculated by Eq. (4.12).

by changing their initial folding angles. These two unit cells are connected in alternating arrangement in the same 1D chain where we have n sets of these two unit cells. Let the initial folding angle for odd-numbered ($j = 2n - 1$) and even-numbered ($j = 2n$) unit cells be $\theta_{j,0}^{(1)}$ and $\theta_{j,0}^{(2)}$ respectively, there are two different stiffness; $K_1\left(\theta_{j,0}^{(1)}\right)$ and $K_2\left(\theta_{j,0}^{(2)}\right)$. Therefore, the equations of motion for the linearized 1D chain model are written as

$$\begin{aligned} M\ddot{u}_n^{(1)} &= K_2\left(u_{n-1}^{(2)} - u_n^{(1)}\right) - K_1\left(u_n^{(1)} - u_n^{(2)}\right) \\ M\ddot{u}_n^{(2)} &= K_1\left(u_n^{(1)} - u_n^{(2)}\right) - K_2\left(u_n^{(2)} - u_{n+1}^{(1)}\right) \end{aligned}$$

where superscripts (1) and (2) represent odd ($j = 2n - 1$) and even ($j = 2n$) numbered unit cells, respectively. By using ansatz $u_n^{(1)} = u^{(1)}e^{i(2kn\bar{h}_0 - \omega t)}$ and $u_n^{(2)} = u^{(2)}e^{i(2kn\bar{h}_0 - \omega t)}$ where $\bar{h}_0 = \left(h_0^{(1)} + h_0^{(2)}\right)/2$, the equations of motion become the following form;

$$\omega^2 \begin{bmatrix} u^{(1)} \\ u^{(2)} \end{bmatrix} = \frac{1}{M} \begin{bmatrix} K_1 + K_2 & -K_1 - K_2 e^{-2ik\bar{h}_0} \\ -K_1 - K_2 e^{2ik\bar{h}_0} & K_1 + K_2 \end{bmatrix} \begin{bmatrix} u^{(1)} \\ u^{(2)} \end{bmatrix} \tag{4.9}$$

Solving this equation as an eigenvalue problem, we obtain the dispersion relationship as

$$\omega^2 = \frac{K_1 + K_2}{M} \pm \sqrt{\left(\frac{K_1 + K_2}{M}\right)^2 - 4\frac{K_1 K_2}{M^2}\sin^2\left(k\bar{h}_0\right)} \tag{4.10}$$

where the solutions with the ± sign represent the acoustic($-$) and optical ($+$) branches based on the classical frequency band theory [52]. We conduct numerical simulations to study dispersion relationship by using the 1D chain of the simplified TMP model, and simulation results are compared with Eq. (4.8) or Eq. (4.10) in the following section.

Numerical Simulations

To analyze dynamic behavior of the simplified TMP model, two different types of numerical computations are performed. One is on the frequency response of a single TMP unit cell, and the other is on the dispersion relationship of a 1D chain of TMP unit cells. The numerical constants used in the simulations are $L = 25$ mm, $m = 19.7$ g, $k_\theta = 1$ Nm/rad.

4.1.1 Frequency response of a unit cell

By applying harmonic excitation to a unit cell, we examine it dynamic behavior under various frequencies. Specifically, the harmonic excitation expressed by $F = F_0 \sin(\omega t)$ is applied to the tip of the single unit cell as shown in Fig. 4.1(b). We solve Eq. (A.6) by using the shooting method to find the steady-state periodic solutions [50]. From the numerical calculation results, we determine the maximum tip displacement defined by the difference between maximum and minimum height of the unit cell ($h_{max} - h_{min}$). We choose three different initial folding angles ($\theta_{j,0} = 30°$, $45°$, and $60°$) to examine the effect of the geometrical parameters, and we apply two different excitation amplitude ($F_0 = 0.01$ N and 1.0 N) to consider the effect of the external excitation.

Simulation results are shown in Fig. 4.3 where blue circles represent solutions obtained numerically by searching from low to high frequency, and green circles are obtained from high to low frequency. In Fig. 4.3, frequencies are normalized by

$$\omega_0 = \sqrt{\frac{K}{M}} = \sqrt{\frac{k_\theta}{8mL^2\cos^2\theta_{1,0}}} \tag{4.11}$$

and red lines are calculated by

$$\omega_\theta = \sqrt{\frac{4k_\theta}{2mL^2 + 2J + 8mL^2\cos^2\theta_{1,0}}} \tag{4.12}$$

which is obtained from Eq. (A.6) by ignoring the velocity term. Figures 4.3(a-c) illustrate the cases of $\theta_{j,0} = 30°$, $45°$, and $60°$, respectively, under $F_0 = 0.01$ N. Each plot shows a resonant peak, which deviates from ω_0 representing the linearized model. The resonance peak can be predicted well by Eq. (4.12) in which the moment of inertia is considered. Figures 4.3(d-f) depict the condition of $F_0 = 1.0$ N under $\theta_{j,0} = 30°$, $45°$, and $60°$, respectively. All cases show two peaks at least, which occur due to the bifurcations induced by the nonlinearity. Another interesting behavior is that resonance peaks are inclined to the higher frequency region if $\theta_{j,0} = 30°$ and $45°$, and to the lower frequency region if $\theta_{j,0} = 60°$. This indicates dynamic behavior of strain-hardening and strain-softening springs, respectively [53]. Therefore, by altering the initial folding angle, we can control the frequency response of the TMP unit cell under harmonic excitations, as well as shifting its dynamics from linear to nonlinear regime.

4.1.2 Dispersion relationship of a 1D TMP chain

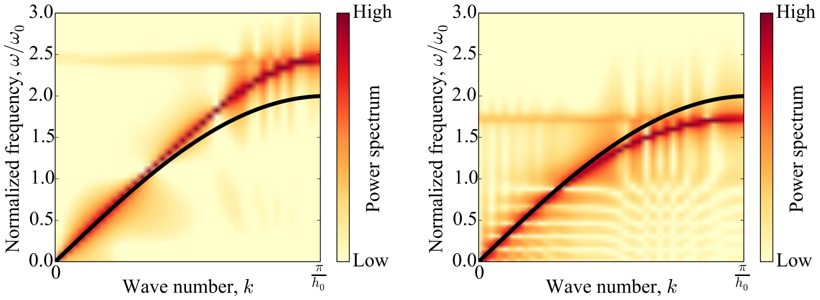

(a) $\theta_{j,0} = 45°$

(b) $\theta_{j,0} = 60°$

Figure 4.4: Dispersion relationship in a 1D homogeneous chain with (**a**) $\theta_{j,0} = 45°$ and (**b**) $\theta_{j,0} = 60°$. Power spectrum is based on numerical simulations, while solid black curves are from analytical predictions based on Eq. (4.8). The frequencies are normalized by $\omega_0 = \sqrt{K/M}$.

To examine wave propagation in a 1D chain of TMP cells as shown in Fig. 4.2, we numerically solve Eq. (4.5) by using the Runge-Kutta method. We analyze wave number and frequency relationship by using 2D FFT. In the simulations, the 1D chain is composed of 80 unit cells, and the right end of the last (80-th) unit cell is fixed by a pin joint as shown in Fig. 4.2(a). Compressive impact of 0.1 N is applied to the first unit cell only for the first 1 ms, and the strain waves propagating in the lattice structure are obtained by defining the strain as $\xi_j = (h_{j,0} - h_j)/h_{j,0}$ where $h_{j,0}$ is an initial height of j-th unit cell. Based on the strain field, we apply 2D FFT and then calculate power spectrum to show the wave modes in the frequency and wave number domain.

Figure 4.4 shows the numerically calculated power spectrum, compared with the analytical predictions based on Eq. (4.8) (black solid curves) for $\theta_{j,0} = 45°$ and $\theta_{j,0} = 60°$. Analytical dispersion curves obtained from the lumped mass model agree well with the numerical results in small k region. However, the discrepancy between the numerical and analytical results increases as k approaches the edge of the first Brillouin zone. It should be noted that such discrepancy is smaller when $\theta_{j,0} = 60^\circ$ compared to $\theta_{j,0} = 45^\circ$ (compare Figs. 4.4(a) and (b)). This is consistent with the result from the unit cell as depicted in Figs. 4.3(b) and (c). That is, from the unit cell response in Fig 4.3, we observe the gap between ω_θ (the actual resonant peak) and ω_0 (which represents the linear model) is smaller when $\theta_{j,0} = 60^\circ$ compared to $\theta_{j,0} = 45^\circ$. The discrepancy between these two peaks stem from the over-simplification of the inertia effect in the lumped mass model, in which the distributed effect of mass (e.g., angular momentum) is neglected. Despite the quantitative disagreement between the numerical and analytical results, the overall shapes of the dispersion curves are in qualitative agreement, showing a single branch (i.e., mode) of wave dispersion.

Now we move to the case of employing heterogeneous unit cells by imposing different initial angles to the TMP cells. Figure 4.5 shows the dispersion curve for the alternating arrangement of initial angles; $\left(\theta_{j,0}^{(1)}, \theta_{j,0}^{(2)}\right) = (60^\circ, 45^\circ)$ shown in Fig. 4.5(a) and $(45^\circ, 60^\circ)$ shown in Fig. 4.5(b). Note that we use the same set of two initial folding angles, but the sequence is different between these two lattices. Thus, the first and second chains will have distinctive ω_0 values based on 60° and 45° folding angles, respectively. We will also show later that this difference results in the formation of a localized mode. The ratio of the stiffness of odd and even number unit cells is $K_2/K_1 = 0.5$ for $(60^\circ, 45^\circ)$ and $K_2/K_1 = 2.0$ for $(45^\circ, 60^\circ)$. In Fig. 4.5, solid black curves are obtained from Eq. (4.10), and there is a band gap between acoustic and optical branches which is not observed in Fig. 4.4. In the inset of Fig. 4.5(b), red and blue circles represent the modal displacements of odd and even numbered unit cells, obtained by plotting eigen-vectors of the corresponding modes. From these mode shapes, it is evident that the lower and upper dispersion curves represent the acoustic (i.e., in-phase between two neighboring cells) and optical (out-of-phase) modes, respectively.

Interestingly, another mode appears between acoustic and optical branches if $\left(\theta_{j,0}^{(1)}, \theta_{j,0}^{(2)}\right) = (45^\circ, 60^\circ)$ (see the highlighted horizontal line in Fig. 4.5(b)). This is due to the waves localized around the first unit cell. Figures 4.5(c-d) show space-time contour plots of strain wave propagation where the strain is normalized by its maximum value. Comparing the

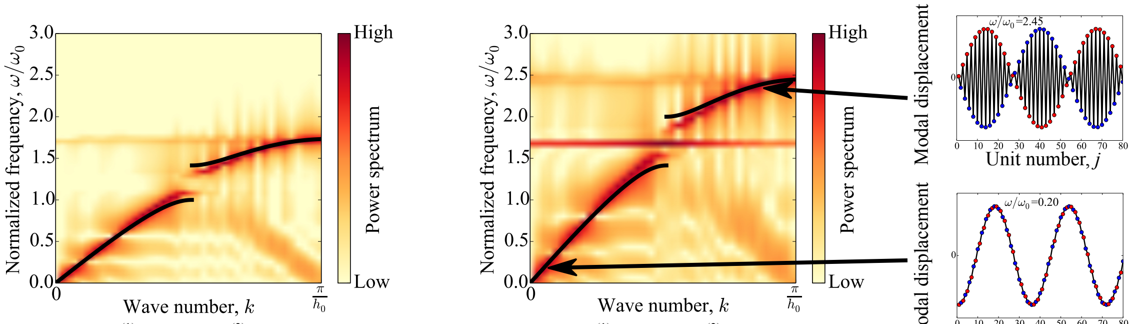

(a) $\theta_{j,0}^{(1)} = 60°$ and $\theta_{j,0}^{(2)} = 45°$

(b) $\theta_{j,0}^{(1)} = 45°$ and $\theta_{j,0}^{(2)} = 60°$

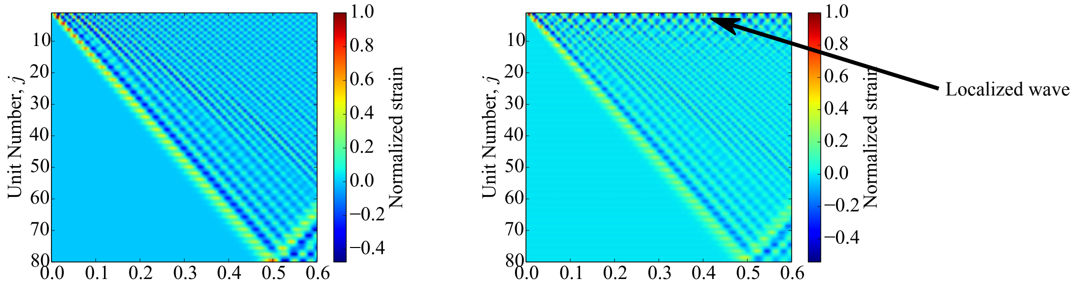

(c) $\theta_{j,0}^{(1)} = 60°$ and $\theta_{j,0}^{(2)} = 45°$

(d) $\theta_{j,0}^{(1)} = 45°$ and $\theta_{j,0}^{(2)} = 60°$

Figure 4.5: Dispersion relationship in a 1D heterogeneous chain with (**a**) $\theta_{j,0}^{(1)} = 60°$ and $\theta_{j,0}^{(2)} = 45°$ (Stiffness ratio is $K_2/K_1 = 0.5$), and (**b**) $\theta_{j,0}^{(1)} = 45°$ and $\theta_{j,0}^{(2)} = 60°$ (Stiffness ratio is $K_2/K_1 = 2.0$). Two insets show the modal displacements for (**lower**) acoustic and (**upper**) optical modes. Black solid curves are analytical predictions based on Eq. (4.10). The frequencies are normalized by $\omega_0 = \sqrt{K_1/M}$. (**c-d**) Space-time contour plots of strain wave propagation for (**a**) $\theta_{j,0}^{(1)} = 60°/\theta_{j,0}^{(2)} = 45°$, and (**b**) $\theta_{j,0}^{(1)} = 45°/\theta_{j,0}^{(2)} = 60°$.

two types of unit cell arrangements, we observe waves tend to be localized around the first unit cell if $\theta_{j,0}^{(1)} = 45°/\theta_{j,0}^{(2)} = 60°$ as shown in Fig. 4.5(d). Such trend is not observed in $\theta_{j,0}^{(1)} = 60°/\theta_{j,0}^{(2)} = 45°$ case (see Fig. 4.5(c)). This is due to the onset of the edge mode. The conditions and properties of such edge modes in origami-based metamaterials will be further studied and will be reported in the authors' future publication.

4.2 Conclusion

We examined dynamic behaviors of origami-based structures consisting of the simplified Tachi-Miura polyhedron (TMP) cells. We analyzed the frequency response of the single unit cell, and by changing the initial folding angle, we were able to control the strain softening/hardening behavior under harmonic excitations. Also, depending on the amplitude of the excitation, the structure exhibits multiple resonance peaks, signaling bifurcation phenomena. Based on this single cell mechanism, we studied a 1D lattice of TMP cells, in which we arranged not only a homogenous chain, but also a heterogenous one with alternating two types of unit cells with different initial folding angles. Our analysis results show the versatile behavior of the frequency band structure, exhibiting both single and double dispersion curves with acoustic/optical modes. By leveraging their tunable wave dynamics, the origami-based mechanical metamaterials can be highly useful to handle vibrations and impact efficiently.

Chapter 5

LINEAR WAVE PROPAGATION IN TCO

In this Chapter, we first approximate the TCO structures into a network of elastic spring elements to suppress the effect of the planar deformation of their facets, while preserving the key features of the TCO cells as we discuss in Chapter 3. For dynamic analysis, we start with modeling a unit cell of the TCO into a two degree-of-freedom (DOF) structure that feature axial and torsional motions under perturbations. Next, we connect these unit TCO cells in series to form a 1D system of origami-based mechanical metamaterial. By using theoretical and computational approaches, we verify that this mechanical metamaterial system can exhibit interesting phenomena of wave dynamics, such as wave mixing effect and the formation of frequency bandgap. See Fig. 7.1(b), e.g., for the selective transmission and rejection of specific frequency components as an outcome of the frequency bandgap. First, we discuss the equation of motion for a 1D chain of the TCO unit cells. Then, we conduct numerical simulations of wave propagation and analyze wave mixing effects and tunable frequency band structure.

5.1 Modeling of the chain of the TCO unit cells

To obtain the dynamic folding motion of the TCO unit cell, we introduce a truss-like structure (see Fig. 5.2), which we introduce in Chapter 3. Figure 5.2(a) shows the original TCO model which has regular polygon cross-sections with n sides ($n = 5$ case is shown in Fig. 5.2(a)). To determine the initial shape of the TCO, we use the three parameters: initial height (h_0), relative angle (θ_0), and circumradius of the cross-section (R) (see Fig. 5.2(b-c)). Let u and φ be the axial displacement from the initial height (h_0) and the rotational angle (φ) measured

---

The texts and figures in this Chapter have been partly taken from the author's publication [54].

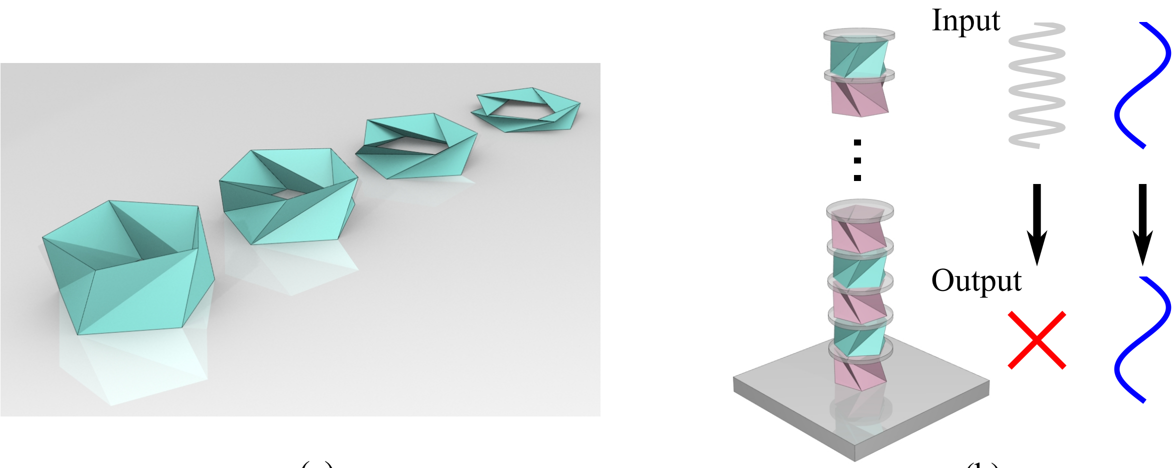

(a) (b)

Figure 5.1: (**a**) Folding motion of the Triangulated Cylindrical Origami (TCO). (**b**) Schematic illustration of TCO-based mechanical metamaterials with allowable and forbidden frequency bands.

from the initial relative angle (θ_0), respectively. We can obtain height (h) and relative angle (θ) of the TCO unit cell for a deformed shape as follows:

$$h = h_0 - u, \qquad \theta = \theta_0 + \varphi. \tag{5.1}$$

Based on the equation of motion for the single TCO unit cell, we design a 1D chain of multiple TCO cells stacked vertically as shown in Fig. 5.3(a). The equations of motion for j-th unit cell in this system is expressed by

$$\begin{aligned} M_j \frac{d^2 u_j}{dt^2} &= F(u_{j-1} - u_j, \varphi_{j-1} - \varphi_j) - F(u_j - u_{j+1}, \varphi_j - \varphi_{j+1}) \\ J_j \frac{d^2 \varphi_j}{dt^2} &= T(u_{j-1} - u_j, \varphi_{j-1} - \varphi_j) - T(u_j - u_{j+1}, \varphi_j - \varphi_{j+1}). \end{aligned} \tag{5.2}$$

For the first unit cell, equations are expressed by

$$\begin{aligned} M_1 \frac{d^2 u_1}{dt^2} &= -F(u_1 - u_2, \varphi_1 - \varphi_2) + F_{in} \\ J_1 \frac{d^2 \varphi_1}{dt^2} &= -T(u_1 - u_2, \varphi_1 - \varphi_2) + T_{in}. \end{aligned} \tag{5.3}$$

In our dynamic analysis, we apply input excitation, force (F_{in}) and torque (T_{in}), to the first unit cell. We solve the nonlinear equations of motion numerically by using the Runge-Kutta method. In addition to nonlinear equations, we also consider the following linearized equations of motion:

$$\begin{aligned} M_j\frac{d^2u_j}{dt^2} &= \alpha_{uu}\left(u_{j-1}+u_{j+1}-2u_j\right)+\alpha_{u\varphi}\left(\varphi_{j-1}+\varphi_{j+1}-2\varphi_j\right) \\ J_j\frac{d^2\varphi_j}{dt^2} &= \alpha_{u\varphi}\left(u_{j-1}+u_{j+1}-2u_j\right)+\alpha_{\varphi\varphi}\left(\varphi_{j-1}+\varphi_{j+1}-2\varphi_j\right). \end{aligned} \tag{5.4}$$

where

$$\alpha_{uu} = \frac{\partial F}{\partial u} = nKh_0^2\left(\frac{1}{a_0^2}+\frac{1}{b_0^2}\right) \tag{5.5}$$

$$\alpha_{u\varphi} = \frac{\partial F}{\partial \varphi} = \frac{\partial T}{\partial u} = -\frac{nKR^2h_0\sin\left(\theta_0-\frac{\pi}{n}\right)}{a_0^2}-\frac{nKR^2h_0\sin\left(\theta_0+\frac{\pi}{n}\right)}{b_0^2} \tag{5.6}$$

$$\alpha_{\varphi\varphi} = \frac{\partial T}{\partial \varphi} = \frac{nKR^4\sin^2\left(\theta_0-\frac{\pi}{n}\right)}{a_0^2}+\frac{nKR^4\sin^2\left(\theta_0+\frac{\pi}{n}\right)}{b_0^2}. \tag{5.7}$$

Please note that these coefficients are governed by the initial configurations, i.e., the initial height (h_0) and angle (θ_0). To conduct Eigenvalue analysis, we use the following ansatz;

$$u_j = ue^{i(kjh_0-\omega t)}, \qquad \varphi_j = \varphi e^{i(kjh_0-\omega t)} \tag{5.8}$$

where k and ω are wave number and angular frequency respectively. Then we can rewrite Eq. (5.4) as

$$-\omega^2\begin{bmatrix} u \\ \varphi \end{bmatrix} = \begin{bmatrix} \frac{\alpha_{uu}}{M_j}\left(e^{-ikh_0}+e^{ikh_0}-2\right) & \frac{\alpha_{u\varphi}}{M_j}\left(e^{-ikh_0}+e^{ikh_0}-2\right) \\ \frac{\alpha_{u\varphi}}{J_j}\left(e^{-ikh_0}+e^{ikh_0}-2\right) & \frac{\alpha_{\varphi\varphi}}{J_j}\left(e^{-ikh_0}+e^{ikh_0}-2\right) \end{bmatrix}\begin{bmatrix} u \\ \varphi \end{bmatrix} \tag{5.9}$$

Therefore, by solving this equation as an eigenvalue problem, we can calculate the relationship between wave number (k) and frequency (ω), namely dispersion relation.

5.2 Wave mixing behavior

To investigate wave propagation in the 1D chain system composed of TCO unit cells, we conduct numerical simulations as well as eigenvalue analysis. In this study, we examine the

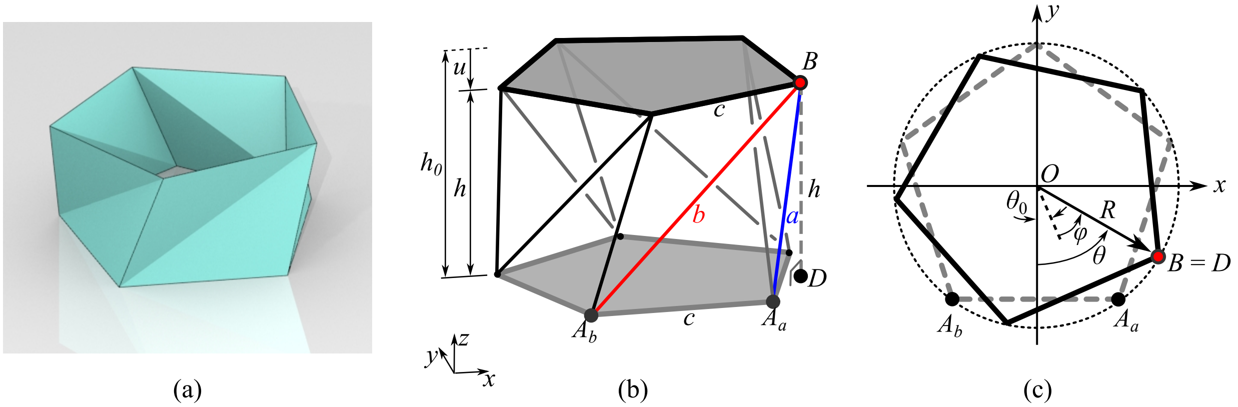

(a) (b) (c)

Figure 5.2: (**a**) Original TCO model. Deformed shape of the TCO. Axial displacement (u) and rotational angle (φ) are show in (**b**) and (**c**).

strain waves which are calculated by defining the strain as $\xi_j = (h_{j,0} h_j)/h_{j,0}$ where $h_{j,0}$ is an initial height of j-th unit cell. Based on the strain field, we apply 2D FFT and calculate power spectrum to analyze the wave modes in the frequency and wave number domain. For the numerical simulation, we use 80 unit cells, and the bottom (80-th) unit cell is fixed on a rigid wall as shown in Fig. 5.3(a). Compressive impact (F_{in}) of 110 N is applied to the first unit cell only for the first 1 ms. The numerical parameters used in the dynamic analysis are $M = 310$ g and $J = 6.37 \times 10^4$ kg-m^2. The initial height (h_0) of the unit cell is 90 mm, and initial angle (θ_0) is 45°.

Figure 5.3(b) shows the space-time contour plot of strain waves, and we observe two different wave modes with different group velocities (see arrows in Fig. 5.3(b)). The wave form at $t = 0.15$ s is shown in Fig. 5.3(c), and the smaller amplitude wave denoted by the black arrow in the figure propagates faster than the larger amplitude wave denoted by the red arrow. Figure 5.3(d) shows the 2D FFT analysis result (surface map, obtained directly by solving Eq. (5.4)) overlapped with eigenvalue analysis (dotted curves, obtained from Eq. (5.9)), and there is a good agreement between these two results. Here, we also confirm the two branches; one corresponding to the lower mode and the other for the higher mode denoted by black and red arrows in Fig. 5.3(d), respectively.

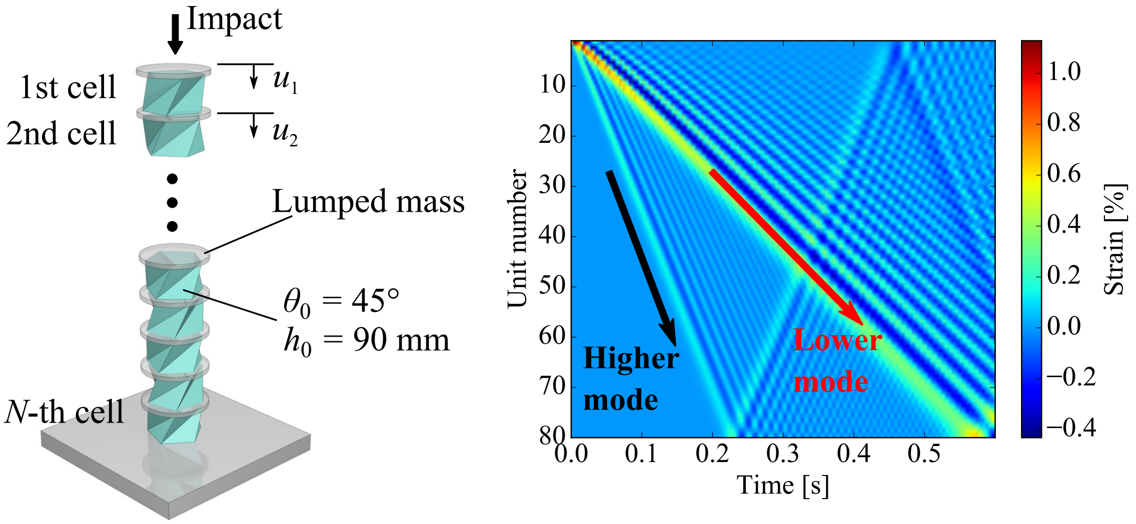

(a) Homogeneous system

(b) Spatio-temporal plot

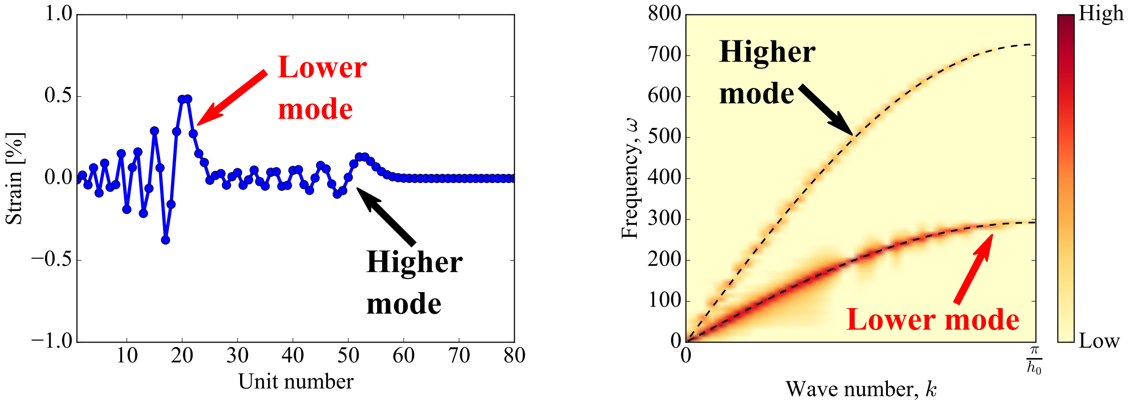

(c) Wave form at $t = 0.15$ s

(d) Dispersion relationship

Figure 5.3: (**a**) Illustration of the homogeneous chain of the TCO. All of the unit cells are identical. (**b**) Spatio-temporal surface plot of strain wave propagation showing two distinctive group velocities. (**c**) Wave form at $t = 0.15$ s. (**d**) Dispersion relationship obtained from 2D FFT applied to (**b**). Black dashed curves are obtained from the eigenvalue analysis.

These lower and higher modes are formed due to the coupling behavior between axial and rotational motions of the TCO. The modes in a coupled system, where wave dynamics of two channels is coupled, can be manipulated by applying two different inputs to the system [38]. For example, if we use sinusoidal excitation of force and torque as input, we can select a specific mode from the TCO-based structure (see conceptual illustration in Fig. 5.4(a)). Let F_{in} and T_{in} be force and torque input excitation respectively, we apply

$$\begin{aligned} F_{\text{in}} &= F_{\text{amp}} \sin\left(\omega_{\text{in}} t\right) \\ T_{\text{in}} &= T_{\text{amp}} \sin\left(\omega_{\text{in}} t\right) \end{aligned} \tag{5.10}$$

where $\omega_{in} = 200$ Hz is selected for both force and torque inputs and $F_{amp} = 5$ N is used for numerical simulations. Here, we introduce the amplitude ratio defined by F_{in}/T_{in} to manipulate coupled wave dynamics. Figure 5.4(b) shows the strain wave propagation if $F_{in}/T_{in} = +20$, and we observe only the lower mode in this case, which is also confirmed by the 2D FFT analysis as shown in Fig. 5.4(c). On the other hand, if $F_{in}/T_{in} = -20$, we obtain the higher mode (see Fig. 5.4(d,e)). Therefore, by controlling the input excitations, we can manipulate the coupled wave dynamics of the TCO-based structure.

5.3 *Tunable frequency band structure*

Next, we consider a 1D chain which consists of two different configurations of TCO unit cells and analyze its wave dynamics. We connect two different unit cells (Unit 1 and Unit 2 in Fig. 5.5(a)) in an alternating way to construct a dimer system as shown in Fig. 5.5(a). For the eigenvalue analysis similar to what we have conducted in the homogenous system, we assume the following ansatz

$$\begin{aligned} u_j^{(1)} &= u^{(1)} e^{i(2kjh_0 - \omega t)}, \quad \varphi_j^{(1)} = \varphi^{(1)} e^{i(2kjh_0 - \omega t)} \\ u_j^{(2)} &= u^{(2)} e^{i(2kjh_0 - \omega t)}, \quad \varphi_j^{(2)} = \varphi^{(2)} e^{i(2kjh_0 - \omega t)} \end{aligned} \tag{5.11}$$

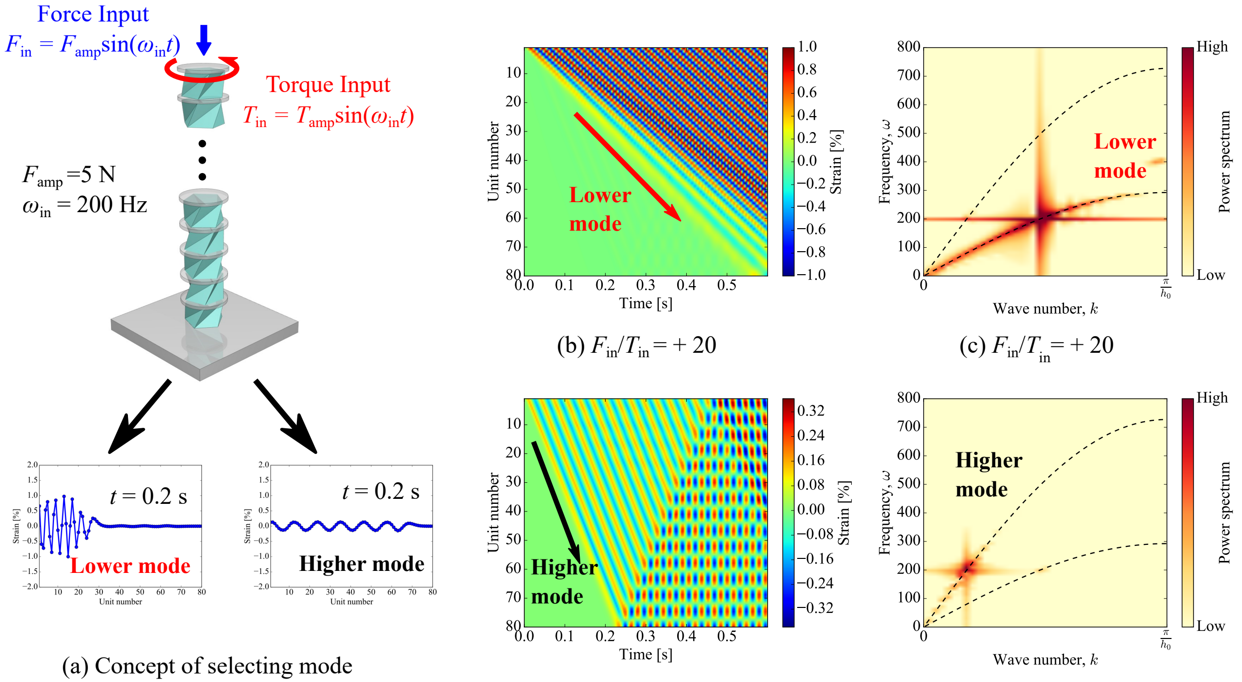

(b) $F_{in}/T_{in} = +20$

(c) $F_{in}/T_{in} = +20$

(a) Concept of selecting mode

(d) $F_{in}/T_{in} = -20$

(e) $F_{in}/T_{in} = -20$

Figure 5.4: (**a**) Conceptual illustration of selecting mode (**b**) Spatio-temporal surface plot and (**c**) dispersion relation for $F_{in}/T_{in} = +20$. In this case, the lower mode with slower group velocity is selected. (**d,e**) shows the case of $F_{in}/T_{in} = -20$, which triggers only the higher mode with faster group velocity.

and then we derive the matrix form as follows (see Apendix B):

$$-\omega^2 \begin{bmatrix} u^{(1)} \\ \varphi^{(1)} \\ u^{(2)} \\ \varphi^{(2)} \end{bmatrix} = \begin{bmatrix} -\frac{\alpha_{uu}^{(1)}+\alpha_{uu}^{(2)}}{M_j} & -\frac{\alpha_{u\varphi}^{(1)}+\alpha_{u\varphi}^{(2)}}{M_j} & \frac{\alpha_{uu}^{(1)}+\alpha_{uu}^{(2)}e^{-2ikh_0}}{M_j} & \frac{\alpha_{u\varphi}^{(1)}+\alpha_{u\varphi}^{(2)}e^{-2ikh_0}}{M_j} \\ -\frac{\alpha_{u\varphi}^{(1)}+\alpha_{u\varphi}^{(2)}}{J_j} & -\frac{\alpha_{\varphi\varphi}^{(1)}+\alpha_{\varphi\varphi}^{(2)}}{J_j} & \frac{\alpha_{u\varphi}^{(1)}+\alpha_{u\varphi}^{(2)}e^{-2ikh_0}}{J_j} & \frac{\alpha_{\varphi\varphi}^{(1)}+\alpha_{\varphi\varphi}^{(2)}e^{-2ikh_0}}{J_j} \\ \frac{\alpha_{uu}^{(1)}+\alpha_{uu}^{(2)}e^{2ikh_0}}{M_j} & \frac{\alpha_{u\varphi}^{(1)}+\alpha_{u\varphi}^{(2)}e^{2ikh_0}}{M_j} & -\frac{\alpha_{uu}^{(1)}+\alpha_{uu}^{(2)}}{M_j} & -\frac{\alpha_{u\varphi}^{(1)}+\alpha_{u\varphi}^{(2)}}{M_j} \\ \frac{\alpha_{u\varphi}^{(1)}+\alpha_{u\varphi}^{(2)}e^{2ikh_0}}{J_j} & \frac{\alpha_{\varphi\varphi}^{(1)}+\alpha_{\varphi\varphi}^{(2)}e^{2ikh_0}}{J_j} & -\frac{\alpha_{u\varphi}^{(1)}+\alpha_{u\varphi}^{(2)}}{J_j} & -\frac{\alpha_{\varphi\varphi}^{(1)}+\alpha_{\varphi\varphi}^{(2)}}{J_j} \end{bmatrix} \begin{bmatrix} u^{(1)} \\ \varphi^{(1)} \\ u^{(2)} \\ \varphi^{(2)} \end{bmatrix} \tag{5.12}$$

where superscript (1) and (2) denote Unit 1 and Unit 2, respectively. From this equation, we calculate the dispersion relation for the dimer system. For numerical parameters, we use the initial angle (θ_0) of $60°/-60°$ for Unit 1/Unit 2 and the other parameters are the same as those in the previous section. Figure5.5(b) shows the dispersion relation. Here, interestingly, we observe a frequency band gap (i.e., a band of forbidden frequencies), which is created just by changing the direction of the initial angle (θ_0) for even-numbered unit cells compared to the homogeneous system. In addition, if we select different initial angles, we can manipulate this frequency band structure as shown in Fig. 5.5(c). This implies that the frequency band gap formed in the TCO-based origami structure is highly tunable by altering the initial geometry of the TCO cells. Another notable feature is that the frequency band gap can start from an extremely low frequency. For example, when $0 = 90$ (i.e., zero-stiffness mode according as we discuss in Chapter 3), we can completely suppress the formation of the low pass band (see the right inset of Fig. 5.5(c)). On the other hand, if we employ the Yoshimura pattern ($\theta_0 = 0°$), we observe no frequency band gaps. Such a tunable frequency band structure can be highly useful for engineering devices for adaptive, anti-vibration applications.

5.4 Conclusion

We studied unique wave dynamics of the triangulated cylindrical origami (TCO) structures with the focus on the formation of frequency band structures. For this, we modeled the TCO cells into a network of spring elements, which significantly reduces the complexity of the TCOs kinematics while preserving their key features. Based on this model, we designed and investigated two different types of TCO-based mechanical metamaterial systems:

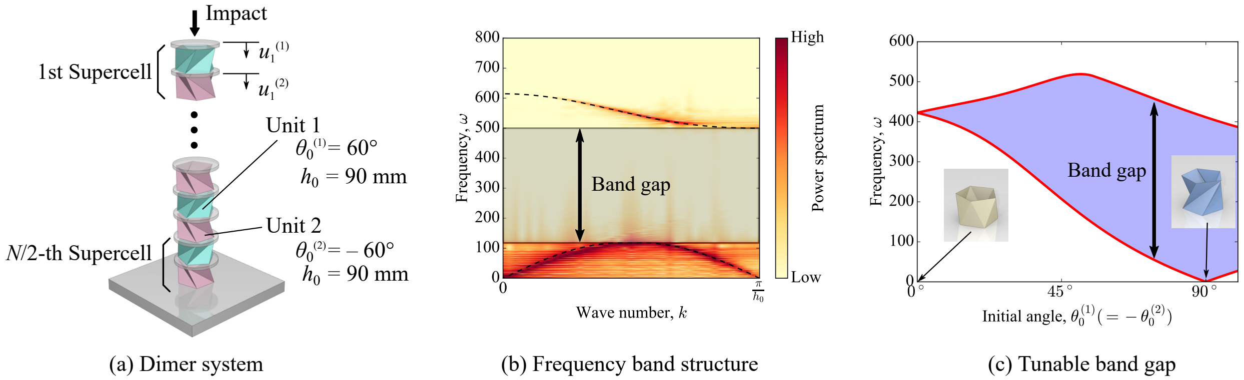

(a) Dimer system (b) Frequency band structure (c) Tunable band gap

Figure 5.5: (**a**) Schematic illustration of the system for a dimer system composed of two different types of the TCO unit cells. (**b**) Dispersion relationship for the dimer system. The gray shaded area indicates the band gap. (**c**) Tunable frequency band gap altered by the different initial angles of the Unit 1 and 2.

homogenous and heterogeneous (specifically dimer) configurations. For the homogeneous system, we observe two modes with different group velocities, corresponding to axial and torsional wave modes in the TCO-based metamaterial system. We also find that the application of two different input excitations enables the selection of a specific wave mode. For the dimer system, the system creates a tunable frequency band structure, which can be altered by the initial geometrical configurations of the TCO. By leveraging these unique properties, the TCO-based mechanical metamaterials have great potential to form novel engineering devices, such as deployable space structures and efficient vibration absorbing systems.

Chapter 6

NONLINEAR WAVE PROPAGATION IN TMP

In this Chapter, we investigate the nonlinear wave dynamics of origami-based systems analytically and numerically by using a single-DOF rigid origami structure as a building block to assemble multi-DOF mechanical metamaterials. Specifically, we employ the Tachi-Miura polyhedron (TMP) [26,27] as a unit cell of the metamaterial as shown in Fig. 6.1. The TMP cell is made of two adjoined sheets (Fig. 6.1(a)), and changes its shape from a vertically standing planar body to a horizontally flattened one while taking up a finite volume between the two phases (Fig. 6.1(b)). This volumetric behavior is in contrast to conventional origami-patterns that feature planar architectures and in-plane motions (e.g., Miura-ori sheets [1]). In this study, we first characterize the kinematics of the TMP cell, showing that it exhibits controllable strain-softening behavior. By cross-linking these TMP unit cells in a horizontal layer (e.g., see [46]) and stacking them up vertically with separators, we form a multi-DOF metamaterial as shown in Fig. 6.1(c). We then conduct analytical and numerical studies to verify that these multi-DOF origami structures can support a nonlinear stress wave in the form of a so-called rarefaction wave, owing to the strain softening nature of the assembled structure.

The rarefaction wave, which can be viewed as a variant of a depression wave [56], has been studied in various settings, including systems of conservation laws [57]. Recently, it was proposed in the context of discrete systems with strain-softening behavior [58, 59]. Interestingly, these rarefaction waves feature tensile wavefronts despite the application of compressive stresses upon external impact (see the conceptual illustrations in Fig. 6.1(c)). In that light, they are fundamentally different from the commonly encountered dynamical

---

The texts and figures in this Chapter have been partly taken from the author's publication [55].

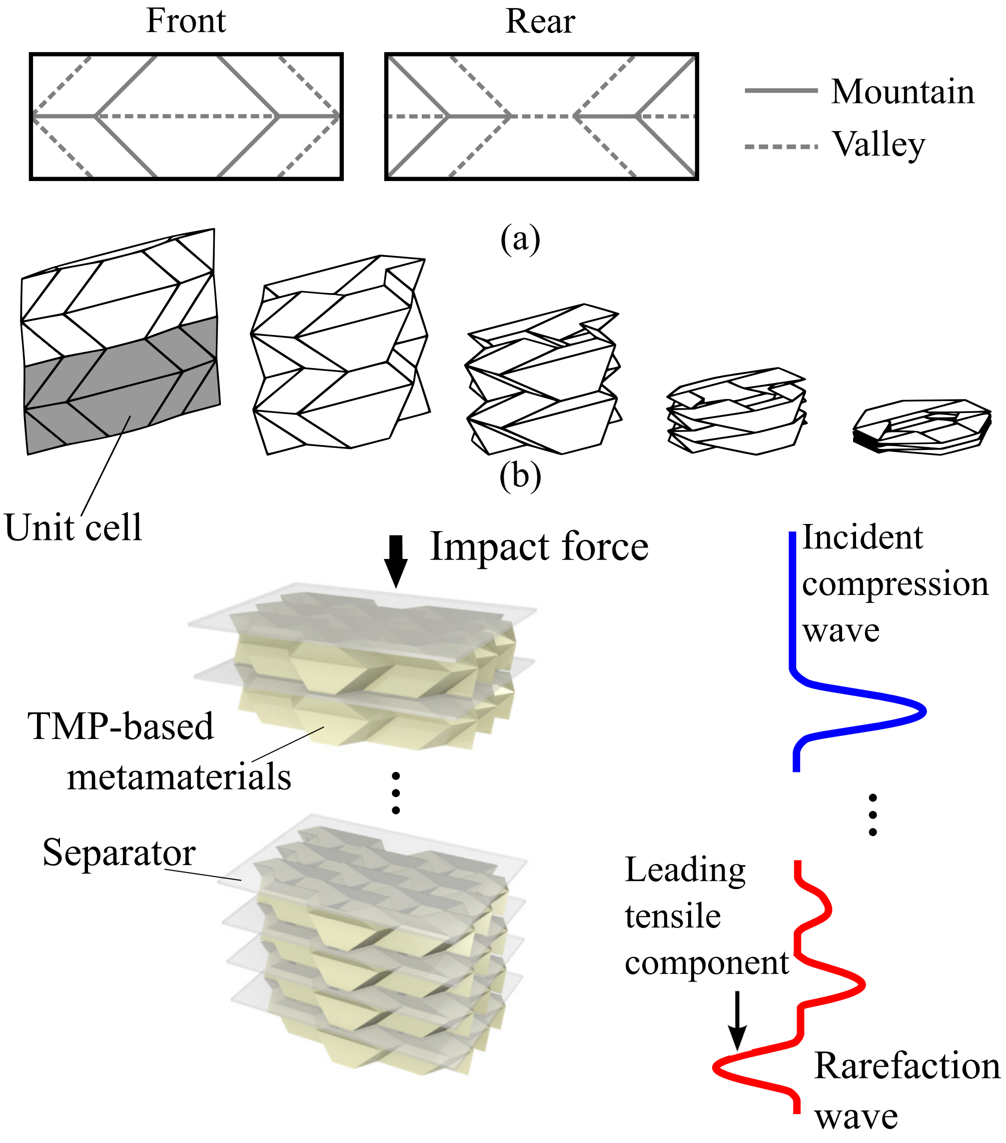

(a)

(b)

(c)

Figure 6.1: (**a**) Flat front and rear sheets of the TMP with mountain (solid lines) and valley (dashed lines) crease lines. (**b**) Folding motion of the TMP unit cell. Shaded area is a unit cell of the TMP, which consists of the front and rear sheets shown in (**a**). (**c**) System consisting of TMP-based metamaterials and rigid separators stacked vertically. Each layer consists of nine inter-linked TMP unit cells (see [46] for details of such horizontal clustering). Conceptual illustrations of incident compressive waves and transmitted rarefaction waves are also shown.

response of nonlinear elastic chains which support weakly or even strongly nonlinear traveling compression waves [59–61]. More recently, strain-softening behavior was shown to be possible in tensegrity structures [62], where rarefaction waves were identified computationally in the elastic softening regime.

In this study, we will study the formation and propagation of rarefaction waves in origami-based metamaterials via two simplified models: a multi-bar linkage model and a lumped mass model. In both cases, we confirm that the origami structure disintegrates strong impact excitations by forming rarefaction waves, followed by other dispersive wave patterns to be discussed in more detail below. We also validate the nonlinear nature of the stress waves by calculating the variations of wave speed as a function of external force amplitude. Notably, we observe the reduction of wave speed as the excitation amplitude increases, which is in sharp contrast to conventional nonlinear waves seen in nature or engineered systems [59]. The findings in this study provide a foundation for building a new type of impact mitigating structure with tunable characteristics, which does not rely on material damping or plastic deformation. This study also offers a platform for exciting the rarefaction pulse – a far less explored type of traveling wave – and examining its characteristics.

6.1 Modeling of Origami-based Structures

We begin by modeling a single TMP cell as shown in Fig. 6.2. For the sake of simplicity, we focus on the folding motion of two adjacent facets along the horizontal crease line as marked by the red line in Fig. 6.2(a).

Preserving the key features of the TMP, such as rigid foldability and single-DOF mobility, we can model the folding/unfolding motion of the origami facets into a simple 1D linkage model as shown in Fig. 6.2(b). Here, the unit cell consists of two rigid bars (mass m and length $2L$), and the center-of-mass coordinates of those two bars are (z_1^L, y_1^L, θ_1) and (z_1^R, y_1^R, $\pi - \theta_1$), where superscripts L and R denote left and right linkages, respectively. The hinge that connects the two bars is equipped with a linear torsional spring with the torsion coefficient k_θ. The left end of the linkage structure is supported by a roller joint, which

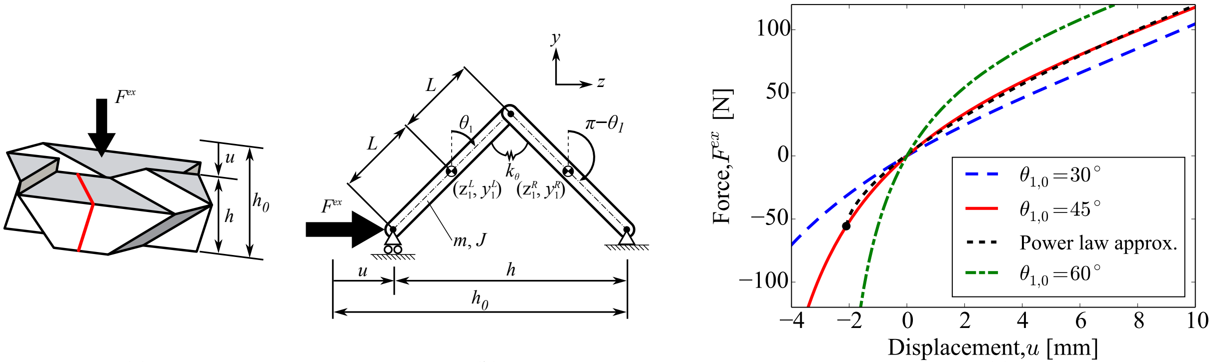

(a) (b) (c)

Figure 6.2: (**a**) TMP unit cell. (**b**) Two-bar linkage model representing the folding motion of the two facets as marked in red lines in (**a**). (**c**) Force-displacement relationship of the TMP unit cell with $L = 5\,\text{mm}$, $k_\theta = 1.0\,\text{Nm/rad}$, and different initial folding angles: $\theta_{1,0} = 30°$, $45°$, and $60°$. Dotted line indicates a power law approximation of $\theta_{1,0} = 45°$ case.

is allowed to move only along the z-axis up on the application of external force F^{ex}. The right end is fixed by a pin joint. Therefore, the inclined angle of the linkage, θ_1, is the only parameter required to describe the motion of this unit-cell system. This corresponds to the single-DOF nature of the TMP cell.

Introducing the general coordinate

$$\boldsymbol{q} = \begin{bmatrix}\theta_1 & \cdots & \theta_j & \cdots & \theta_N\end{bmatrix}^T,$$

we can obtain the equation of motion as follows (please see Appendix A for the derivation):

$$\boldsymbol{G}^T\hat{\boldsymbol{M}}\boldsymbol{G}\ddot{\boldsymbol{q}} + \boldsymbol{G}^T\hat{\boldsymbol{M}}\dot{\boldsymbol{G}}\dot{\boldsymbol{q}} = \boldsymbol{G}^T\boldsymbol{f}. \tag{6.1}$$

where $\boldsymbol{G}$ is a Jacobian matrix (see Apendix A for the detail), and $\hat{\boldsymbol{M}}_j$ is a mass matrix expressed as

$$\hat{\boldsymbol{M}}_j = \text{diag}\begin{bmatrix}m & m & J & m & m & J\end{bmatrix},$$

and J is the bar's moment of inertia ($J = mL^2/3$). Also, $\boldsymbol{f}_j$ is a force vector defined as follows

$$
\boldsymbol{f}_j = \begin{cases} [F^{ex}, \quad 0, \quad -2k_\theta\left(\theta_1 - \theta_{1,0}\right) - F^{ex} L\cos\theta_1, & \\ \quad 0, \quad 0, \quad -2k_\theta\left(\theta_{1,0} - \theta_1\right)] & \text{if } j = 1 \\ [0, \quad 0, \quad -2k_\theta\left(\theta_j - \theta_{j,0}\right), & \\ \quad 0, \quad 0, \quad -2k_\theta\left(\theta_{j,0} - \theta_j\right)] & \text{if } j = 2\ldots N \end{cases}
$$

where $\theta_{j,0}$ is the initial folding angle of the j-th unit cell (i.e., no torque applied at the hinge in this initial angle), and F^{ex} is the external force applied to the first unit cell as shown in Fig. 6.3(a). The advantage of the principle of virtual power is that we can apply it to a system with both motion and geometrical constraints, and we can derive the equation of motion without considering force constraints. Plugging these expressions into Eq. (A.5), we finally obtain the equation of motion of the single unit cell as

$$
\begin{aligned} \left(mL^2/2 + J/2 + 2mL^2\cos^2\theta_1\right)\ddot{\theta}_1 - mL^2\dot{\theta}_1^2\sin 2\theta_1 \\ +k_\theta\left(\theta_1 - \theta_{1,0}\right) = -F^{ex}L\cos\theta_1. \end{aligned} \tag{6.2}
$$

Here, we consider the quasi-static case (i.e., acceleration and velocity terms are much smaller compared to the external excitation and spring force terms), and the force-displacement relationship can be derived as follows:

$$
F^{ex} = -\frac{k_\theta\left(\theta_1 - \theta_{1,0}\right)}{L\cos\theta_1}. \tag{6.3}
$$

Note that F^{ex} is the external force applied to the roller joint as shown in Fig. 6.2(b). Using Eq. (6.3) and the axial displacement expression $u = 4L(\sin\theta_{1,0} - \sin\theta_1)$, we can calculate the force-displacement response as shown in Fig. 6.2(c). We observe that the system exhibits strain softening behavior in the compressive region, whereas the system shows strain hardening response in the tensile domain. Also, it is interesting to find that this strain softening/hardening behavior can be tuned by controlling the initial folding angle, $\theta_{1,0}$.

In this section, we introduce a lumped mass model, in which a chain of origami cells is modeled as lumped masses connected by nonlinear springs (see Fig. 6.3(b)). The strain softening behavior of the TMP unit cell considered herein leads to the following power-law

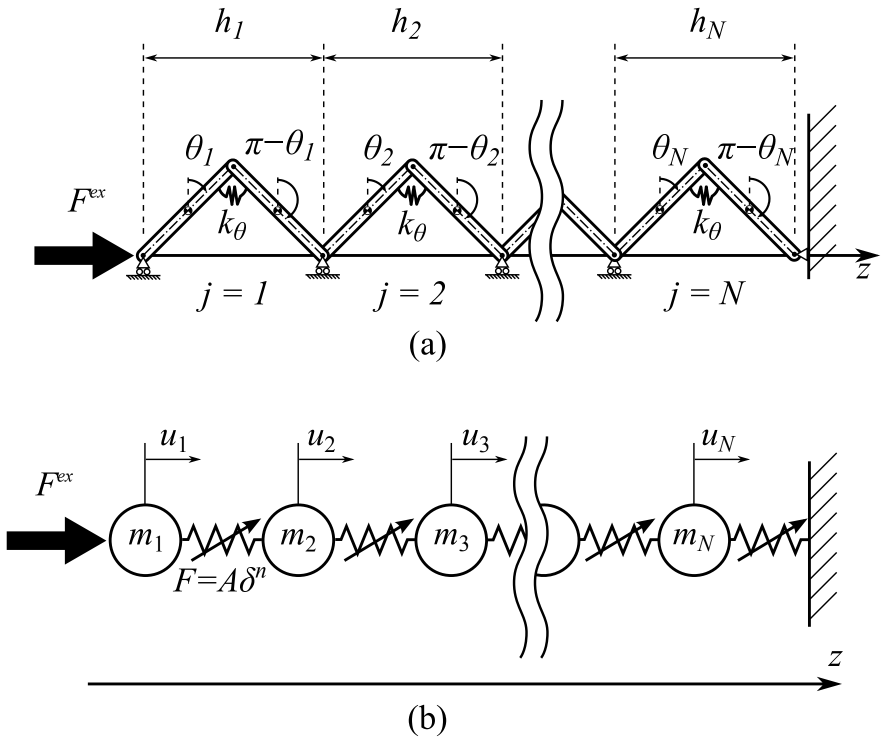

Figure 6.3: Schematic illustrations of (**a**) Multi-bar linkage model and (**b**) Lumped mass model.

relationship:

$$F^{ex} = A\delta^{n} \tag{6.4}$$

where δ is the compressive displacement, and the coefficient A and the exponent n are the constant values determined by curve fitting of Eq. (6.3).

Since the power-law relationship in Eq. (6.4) assumes only a positive displacement as an argument, we need to apply a displacement offset (denoted by d_0) towards the tension side, so that the lumped mass model can approximate the force-displacement curve of the multi-bar linkage model not only in the compressive region, but also in the tensile domain. In Fig. 6.2(c), the dashed curve shows the fitted power-law relationship for the multi-bar linkage model, where the black circle represents (along the horizontal axis) the displacement offset d_0.

By using this simple force-displacement relationship, we can derive a general expression of the equation of motion as follows:

$$M\ddot{u}_j = A\left[d_0 + \delta_{j-1,j}\right]_+^n - A\left[d_0 + \delta_{j,j+1}\right]_+^n \tag{6.5}$$

where M is the lumped mass corresponding to $2m$, $n \in \mathbb{R}$, and the bracket is defined by $[\cdot]_+ = \max(0, \cdot)$. Note that this form of equation has been used widely for analyzing nonlinear waves propagating in discrete systems in the case of strain-hardening interactions (i.e., $n > 1$ in Eq. (6.5), e.g., granular crystals). Therein, the formation and propagation of nonlinear wave structures, such as solitary waves [59, 60] and discrete breathers [61], have been well studied. The interpretation of origami dynamics via this nonlinear lumped mass system opens up a broad, novel potential vein of studies. Indeed, one advantage of modeling the origami lattice in this way is that many tools and results obtained in the context of granular crystals and more generally Fermi-Pasta-Ulam-type settings [63, 64] can be applied in our system. For example, the recent work of [58] examined a one-dimensional discrete system under the power-law relationship of strain-softening springs (i.e., $n < 1$ in Eq. (6.5)). This study reported the propagation of rarefaction waves through dynamic simulations and a long wavelength approximation, where it was shown that the width of the rarefaction wave is independent of the wave speed. In the work of [62], a lattice of tensegrity structures were shown to be described by Eq. (6.5) with $n < 1$. In this setting rarefaction waves were also studied. The analysis of nonlinear waves in post-buckled structures has been also attempted using a similar discrete system [65].

6.2 Numerical Simulations

To examine the dynamic characteristics of the origami-based structure and compare the results from the two reduced models, we conduct numerical computations of wave propagation under a compressive impact. Also, we apply various amplitudes of impact force to the multi-bar linkage model in order to examine the speed of both compressive and tensile strain waves, especially focusing on the dominant traveling wave.

We perform numerical computations where a compressive impact is applied to the first unit cell with the right end of the N-th unit cell kept fixed as shown in Fig. 6.3(a). The strain waves propagating in a uniform chain of $N = 400$ unit cells are examined numerically. In the case of the multi-bar linkage model, the relative strain is defined as

$$\eta_j = \frac{h_{j,0} - h_j}{h_{j,0}} \tag{6.6}$$

where $h_j = 4L \sin\theta_j$ and $h_{j,0} = 4L \sin\theta_{j,0}$ (see Fig. 6.2(b)). The numerical constants used in the calculation are the following: $L = 5\,\text{mm}$, $m = 0.39\,\text{g}$, $k_\theta = 1.0\,\text{Nm/rad}$, and $\theta_{j,0} = 45°$. To apply impact excitation, we impose $F^{ex} = 100\,\text{N}$ for the first 1 ms and $F^{ex} = 0\,\text{N}$ after the first 1 ms in our simulations. From the force-displacement curve based on these constants, we obtain $n = 0.64$ and $A = 2,938\,\text{N/m}^n$, given an initial displacement offset of $d_0 = 2.1\,\text{mm}$ for the power-law approximation. In the case of the lumped mass model, the relative strain is defined as

$$\eta_j = \frac{u_{j+1} - u_j}{d_0}. \tag{6.7}$$

Figures 6.4(a) and (b) show space-time contour plots of strain wave propagation under compressive impact, while Figs. 6.4(c) and (d) show the strain waveforms corresponding to $t = 3, 40$, and $70\,\text{ms}$. Note that in Figs. 6.4(c) and (d), the strain curves at $t = 3$ and 40

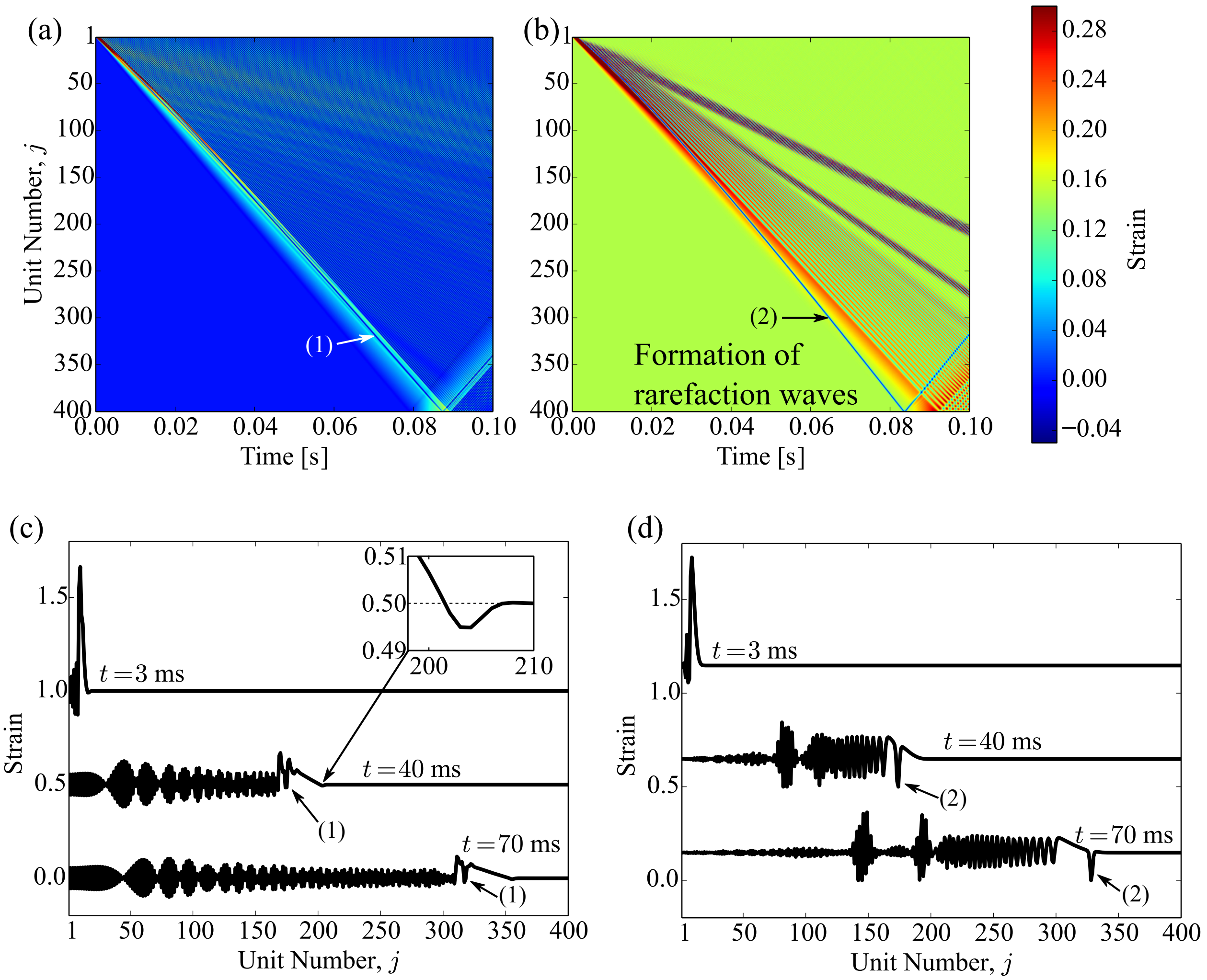

Figure 6.4: Space-time contour plots of strain wave propagation based on (**a**) the Multi-bar linkage model and (**b**) the Lumped mass model. Temporal plots of strain waves using (**c**) the Multi-bar linkage model and (**d**) the Lumped mass model. Strain curves at $t = 3$ ms and 40 ms are offset by 1.0 and 0.5, respectively, to ease visualization. The inset in (**c**) shows the magnified view of the leading edge. The arrows (1) and (2) point to the rarefaction wave present in the dynamics.

ms are shifted vertically by 0.5 and 1, respectively, to ease visualization. After the impact force is applied to the system, the first compressive impact attenuates quickly as the strain waves propagate through the system, and then a rarefaction wave appears in front of the first compressive wave (see the insets as well as the arrows (1) and (2) in Fig. 6.4). It should be also noted that due to the strain-softening behavior, the amplitude of the compressive force is reduced drastically as the wave propagates along the chain. Since both the multi-bar linkage model and the lumped mass model have this strain-softening nature, the analogous type of rarefaction waves is observed.

In addition, the inset of Fig. 6.4(c) shows the magnified view of the leading edge of the propagating strain wave. This leading wave is created due to the effect of inertia in the multi-bar linkage model. That is, when the first unit cell folds right after the compressive impact, the second unit cell is pulled by the first unit cell before the compressive force propagates to the next unit cell. Therefore, the tensile strain appears in front of the first compressive wave in the multi-bar linkage model. Comparing the numerical results of the two models, the lumped mass model captures the multi-bar linkage model dynamics even quantitatively at short times.

Let us also note in passing that in the wake of this primary rarefaction pulse, we observe radiative dispersive wavepackets both in the multi-bar linkage model and in the lumped mass model. These wavepackets apparently travel maximally with the speed of sound in the medium, while the rarefaction pulse outrunning them is apparently supersonic. We will return to this point to corroborate it further by our numerical bifurcation analysis in the next section. Additionally, it should be noted that in the lumped mass model, highly localized structures with a clear envelope can be discerned (see e.g., the vicinity of unit number 150 of the 70 ms panel of Fig. 6.4(d)), which seem to have the form of excitations, which are exponentially localized in space and periodic in time [66,67]. A closer inspection of Fig. 6.4(b) also seems to suggest that such coherent wavepackets travel more slowly than the dispersive radiation. The multi-bar linkage model also exhibits such time-periodic patterns, but there is no clear signature of spatial localization. The fundamental difference of wave propagation between these two models stems from the fact that the lumped mass model neglects rotational motions of origami components, while the multi-bar linkage model accounts for coupled motions of both translational and rotational dynamics of origami. While these nonlinear wave structures are worth investigating, this topic is beyond the scope of this study, and we do not explore them further here.

6.3 Conclusions

In this Chapter, we investigated nonlinear wave dynamics in origami-based metamaterials consisting of building blocks based on Tachi-Miura polyhedron (TMP) cells. We analyzed the kinematics of the TMP unit cell using a simple multi-bar linkage model and found that it exhibits tunable strain-softening behavior under compression due to its geometric nonlinearity. We observed that upon impact, this origami-based structure supports the formation and propagation of rarefaction waves. The resulting evolution features a tensile wavefront despite the application of compressive impact. A further reduction was also offered based on the fitted force-displacement formula for a single cell, in the form of a lumped mass model. The dynamical features observed herein may constitute a highly useful feature towards the efficient mitigation of impact by converting compressive waves into rarefaction waves and disintegrating high-amplitude impulses into small-amplitude oscillatory wave patterns. We also demonstrated the potential tunability of the wave speed by altering initial folding conditions of the origami-based structure, which naturally opens up the feasibility of controlling stress wave propagation in an efficient manner.

The rather unique nonlinear wave dynamics of origami structures can lead to a wide range of applications, such as tunable wave transmission channels and deployable impact mitigating layers for space and other engineering systems. These applications will leverage intrinsic versatility of origami structures, e.g., the formation of not only rarefaction waves, but also other types of nonlinear waves and tunable frequency band structures. On the theoretical/computational side, there is also a large number of intriguing questions that are emerging. For example, a more detailed comparison of the coherent wave structures propagating in the multi-bar linkage model vs. the lumped-mass model would be an interesting topic for further consideration. This would help uncover the dynamical features leading to the apparent weak amplitude decay in the former, in contrast to the robust wave propagation in the latter. At the single wave level, an exploration of the delicate issues of spectral stability by means of different numerical methods and of the corresponding dynamical implications would be of particular interest. Subsequently, understanding the dynamics and interactions of multiple rarefaction wave patterns would also be a relevant theme for future investigations.

Chapter 7

NONLINEAR WAVE PROPAGATION IN TCO

While the TMP structure described in Chapter 6 shows novel nonlinear wave dynamics, the experimental verification of such dynamics (e.g., rarefaction wave formation) is highly challenging. This is because of (i) the difficulty in fabricating rugged, multi-DOF waveguide using the TMP unit cells; and (ii) the necessity of assembling a long chain (e.g., 300 elements in Fig. 6.4 in Chapter 6) to form rarefaction waves. In this Chapter, we investigate the nonlinear wave propagation in the chain of the TCO unit cells, specifically the rarefaction solitary wave (see Fig. 7.1). We fabricate the TCO unit cell by using paper sheet (Fig. 7.1B), and conduct compression test on fabricated prototypes. Unlike the TMP, this TCO offers unique advantages, such as the intrinsic multi-DOF characteristic and the efficacy in forming rarefaction waves even using a dozen unit cells. As a first step, by leveraging the simplified truss-like model that we discuss in Chapter 3, we approximate the static/dynamic folding behavior of the paper prototype, which provides simple yet powerful numerical and analytical tools to analyze the unique wave propagation in the system. Then, we conduct dynamic analysis by applying compressive impact to the end of the chain (see Fig. 7.1C and D). We observe the rarefaction solitary wave experimentally, and examine the shape and wave speed of this solitary wave experimentally, numerically, and analytically. Interestingly, although the compressive impact is applied to the system, the tensile solitary wave propagates ahead of the initial compressive strain, which is a counter intuitive phenomena. In addition, the amplitude of the incident compressive strain is attenuated significantly, therefore, this strong attenuation for compressive impact, togethered with the formation of rarefaction solitary wave, can be used for designing a new type of impact mitigation systems.

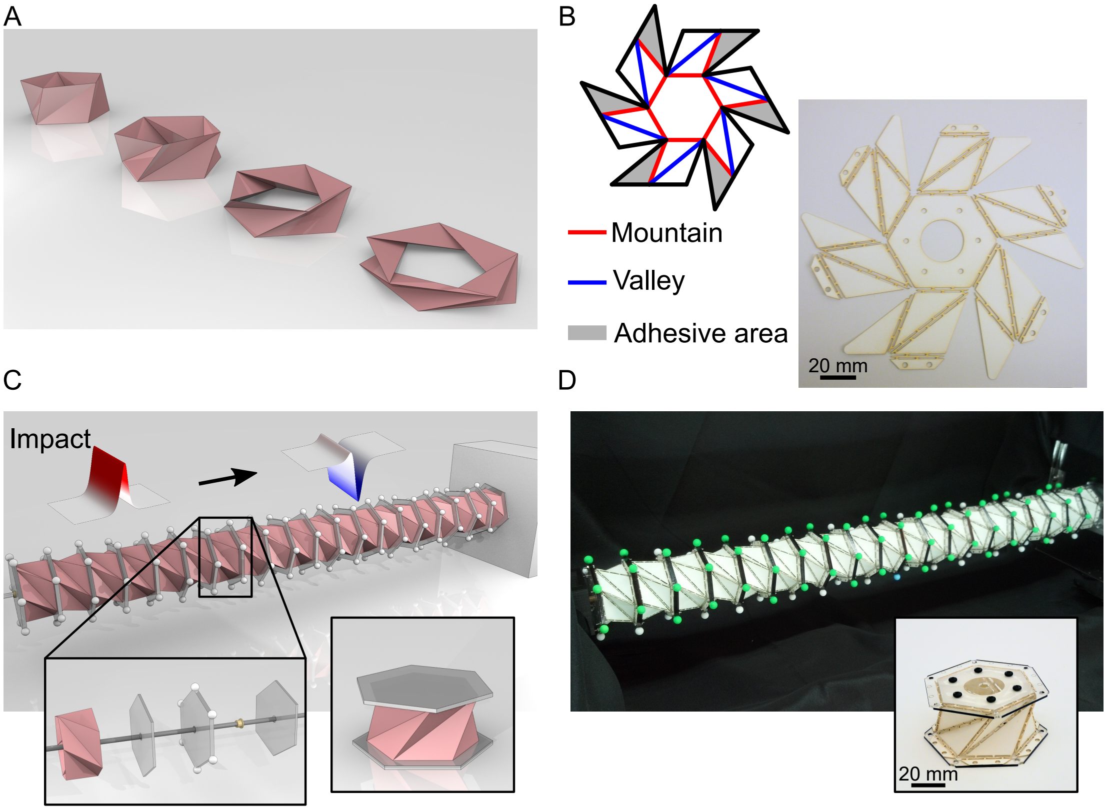

Figure 7.1: Schematics and digital images of the triangulated cylindrical origami prototypes. (**a**) Folding motion of the TCO is shown in sequence. (**b**) The flat sheet with crease patterns (upper left) is composed of mountain crease lines (red), valley crease lines (blue), and the adhesive area (shaded area). The photograph shows corresponding laser-cut paper sheets (lower right). (**c**) The origami-based metamaterial generates the rarefaction solitary wave despite the application of compressive impact. The system is composed of the TCO unit cells (lower right). To connect the neighboring unit cells, the interfacial polygonal cross-section is used (lower left). (**d**) The actual prototype of the system and its unit cell (lower right inset).

7.1 *Static mechanical response of paper prototype*

We start by examining the geometry of the TCO unit cell. The TCO structure shows axial and rotational motions coupled to each other, and we characterize this folding motion by using the axial displacement (u) and rotational angle (φ), which are defined with respect to the initial height (h_0) and angle (θ_0) (Fig. 7.6 A and B). To analyze the kinematics of the origami, we construct a simplified mathematical model which approximates the folding behavior of the TCO into linear spring motions along the crease lines [48]. In this model, we use two different spring constants (K_a and K_b) for the shorter ($\overline{A_aB}$ in Fig. 7.6 A) and longer crease lines ($\overline{A_bB}$), respectively. Also, the bending motion between the triangular facet and the edge of the N_p-sided polygon (denoted by the shaded area in Figs. 7.6 A and B with the radius R of the circle circumscribing the polygon) is modeled as a torsional spring with the spring constant K_ψ. These three spring constants are determined empirically by conducting compression tests on the fabricated TCO cell.

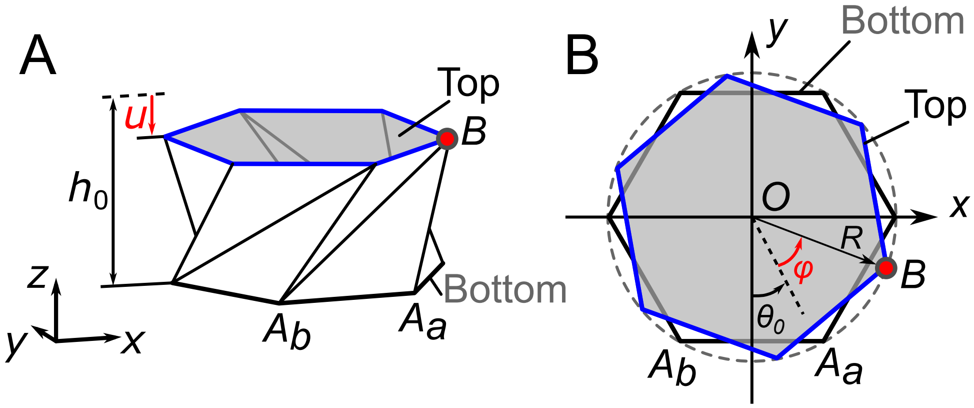

Figure 7.2: Geometry of the TCO and experimental data of force-displacement relationship with strain softening behavior. (**a**) The axial displacement (u) is defined with respect to the initial height of the TCO (h_0). (**b**) Top-down view shows the rotational angle (φ) defined with respect to the initial angle (θ_0).

7.1.1 *Prototype fabrication*

We use construction paper sheets (Strathmore 500 Series 3-PLY BRISTOL, thickness of the paper is 0.5 mm) for the origami part (see Fig.1B), and extruded acrylic sheets with the thickness of 1.6 mm for the interfacial polygon as shown in the inset of Fig.1C. These two materials are tailored by a laser cutting machine (VLS 4.6, Universal Laser Systems) as shown in Fig. 7.3A. For the crease of the TCO unit cell, we design a customized crease lines based on the compliant mechanisms (Fig. 7.3B). By using this crease pattern, each crease line shows enhanced repeatable and consistent folding behavior and fatigue property, compared with crease lines made from purely flat sheet configurations. It should be also noted that this crease pattern (e.g., length, width, and distance of cut slits) affects the compressive force-displacement behavior of the TCO cell significantly. In this study, we prototype twenty identical TCO unit cells by choosing $h_0 = 35$ mm, $\theta_0 = 70°$, and $R = 36$ mm. After the unit cell prototype is assembled by hand, we apply the preconditioning process, which we discuss in the next section, to minimize the errors among fabricated prototypes.

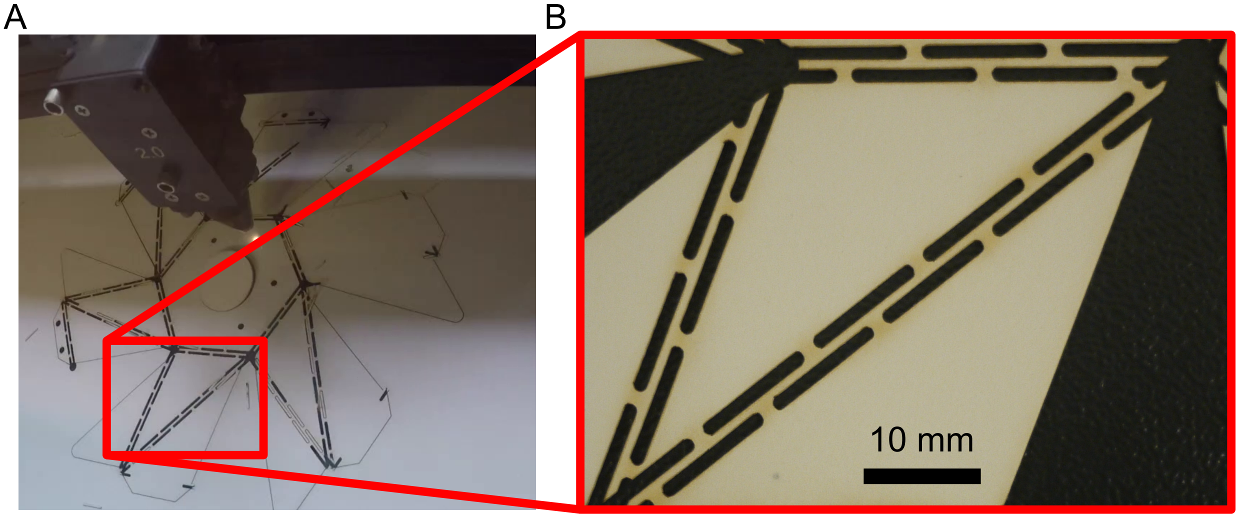

Figure 7.3: Fabrication of the TCO unit cell. (**a**) Laser cutting the crease pattern of the TCO unit cell. (**b**) Customized crease line based on compliant mechanisms.

7.1.2 Preconditioning process

To obtain the consistent folding behavior from all TCO unit cells, we design a recipe for preconditioning each fabricated prototype. Each prototype is assembled by hand, therefore the folding behavior, specifically force-displacement relationship, varies among the samples. Any inclusion of abnormal cells into the chain of the origami system will cause disruption of wave propagation in the system, causing unwanted reflection and/or localization of waves in the spot of these 'impurity' cells. Similarly, the repeatability of folding/unfolding behavior of each unit cell is also a critical factor to ensure reliable performance of the whole origami system.

To address this issue, we conduct fatigue tests on all unit cells by using the customized load frame as shown in Fig. 7.4. The unit-cell prototype is placed vertically on the load frame (Fig. 7.4) where the bottom part of the unit cell is fixed. The top end of the unit cell is connected to the load cell (LUX-B-50N-ID, Kyowa) through a sleeve bearing (PTFE) so that the top polygon is constrained in the axial direction but it can rotate freely around the longitudinal axis. The top part holding the load cell is actuated by the motor-driven linear stage (BiSlider, Velmex). Note that by using this system, we apply a desired compression to the system, while allowing free rotational motions and restricting any bending motions of the prototype (see the sequence of the compresion test as shown in Fig. 7.4. The displacement is measured by the non-contact laser sensor (CMOS Multi-Function Analog Laser Sensor IL-065, Keyence). By using this load frame, we apply 200 cycles of controlled displacement from -3 mm (tension) to 15 mm (compression) at 6 mm/s, and we measure the corresponding force-displacement relationship.

Figure 7.5A shows the loading and unloading curves from the first cycle (i.e., newly fabricated state without experiencing axial force) to the 200th cycle. One of the noticeable feature is that the first cycle shows the significant maximum force peak during loading (denoted by the black curve in Fig. 7.5A). Then, as the number of cycles increases, each curve traces a similar path. To analyze this fatigue behavior, we consider the area bounded by the

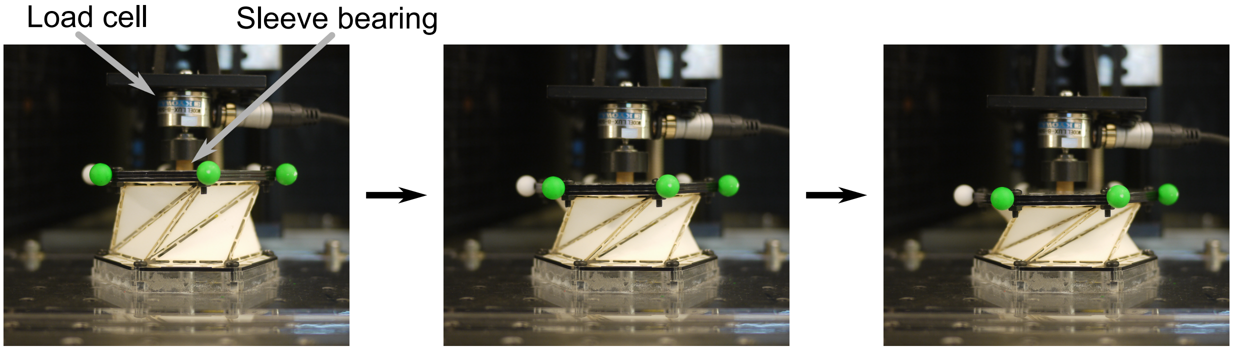

Figure 7.4: Compression test on the TCO unit cell. The top polygon of the TCO unit cell is attached to the load cell through the sleeve bearing so that the top surface is constrained in the axial direction, but it can freely rotate. The sequence of the compression is shown from the left to right photographs.

loading and unloading curves for each hysteresis loop, and we plot the area as a function of the number of cycles as shown in Fig. 7.5B. The area enclosed by the hysteresis loop is associated with energy dissipation, and in Fig. 7.5B, we normalize this area by that of the first cycle. For the initial fifty cycles, the energy dissipation decreases significantly, and then the slope of the energy dissipation curve becomes relatively small value. Therefore, if the fabricated prototypes that experienced only a few loading/unloading cycles are used for both static and dynamic experiments, the performance of the unit cell depends highly on the history of the loading/unloading. On the other hand, if we apply enough number of loading/unloading cycles to the prototypes, each unit cell shows the consistent and repeatable folding behavior with less effect of the cycle history. Hence, we apply this cyclic preconditioning process (200 cycles, displacement of $-3 \sim 15$ mm) to all unit cells in advance of the static compression test and the dynamic test.

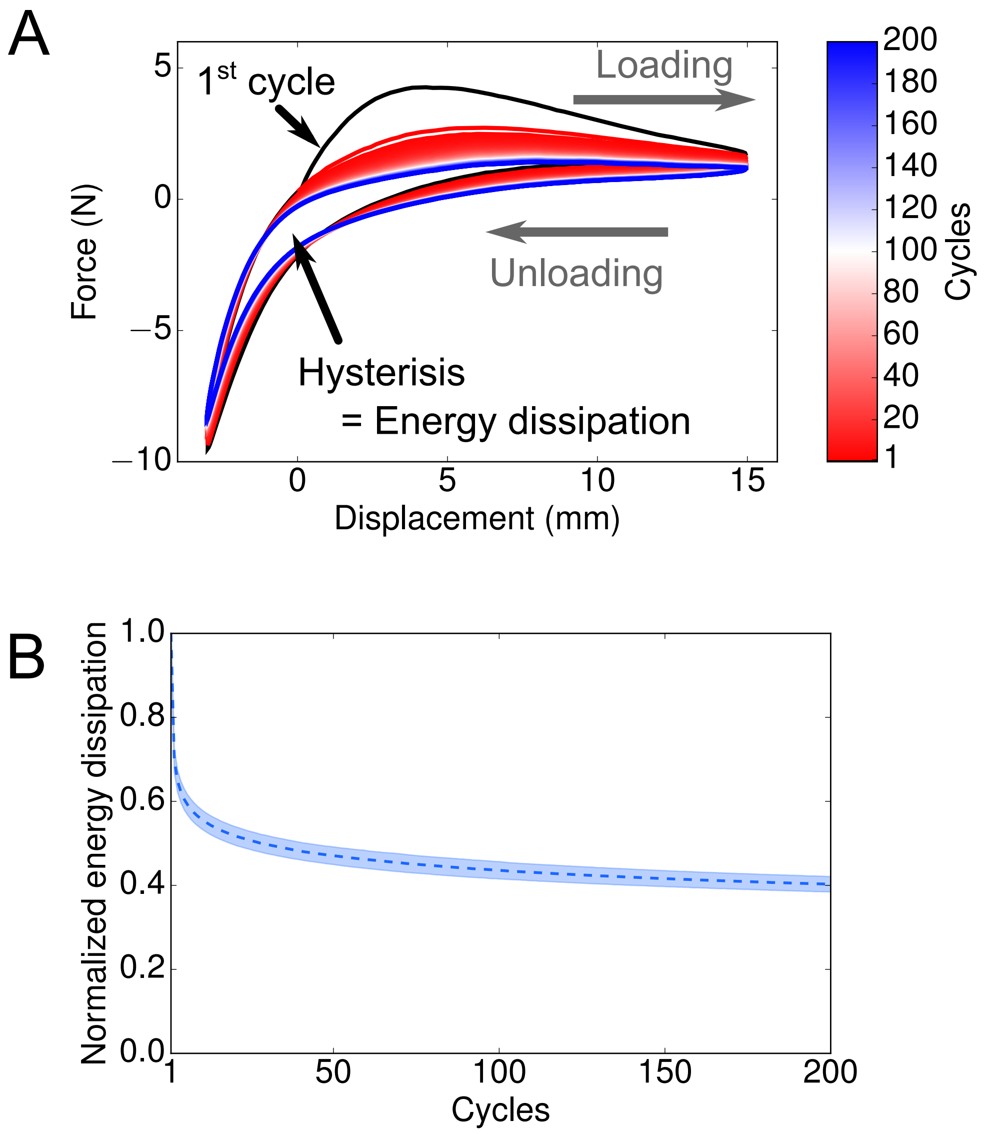

Figure 7.5: Fatigue property of the TCO single unit cell. (**a**) Force-displacement curves for 200 loading/unloading cycles. The color gradient indicates the number of cycles. (**b**) The area enclosed by each hysteresis loop (i.e., energy dissipation) is plotted as a function of cycles. The energy dissipation is normalized by that of the first hysteresis loop. We use twenty of the TCO prototypes, and the mean value is shown as the dashed line, and the standard deviation is represented by the colored area.

7.1.3 Compression test on a single unit cell

Figure 7.6 shows the experimental result (solid curve), along with the analytical prediction (dashed curve) obtained from the simplified model. We observe the analytical model corroborates the experimental result. Also, we validate the strain softening behavior of the TCO under compression, i.e., the stiffness of the structure decreases as it is compressed. In addition, by using the simplified model, we can analyze the elastic potential energy change as a function of u/h_0 and φ (see the inset of Fig. 7.6, where the dark color indicates a minimal energy regime). This near-curve trajectory indicates how the deformation of the TCO cell takes place by coupling axial and rotational motions (see Chapter 3).

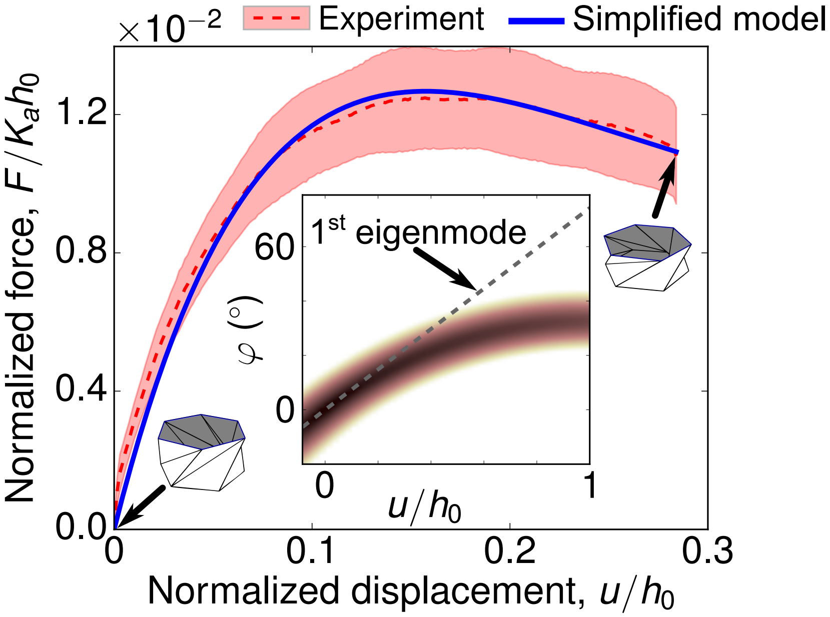

Figure 7.6: Compression test result. Experimentally measured axial force normalized by the spring constant (K_a) and h_0 (the mean value is shown as dashed curves, and s.d. is represented by colored areas) is compared with the simplified linear spring model (blue). The inset shows the surface plot of the elastic potential energy. The darker color indicates the lower energy level. The dashed line shows the folding behavior of the reduced 1D model obtained from the first eigen mode.

7.2 Experimental verification of rarefaction solitary wave

Based on the unit cell analysis, we investigate the wave dynamics in a chain of TCO cells (Fig. 7.7 A). The left end of the chain (unit number $n = 1$) is connected to the shaker (LDS V406 M4-CE, Brüel & Kjær) through the customized attachment with a sleeve bearing, which transfers shaker impact to the cell while allowing its free rotational motion. The TCO cell positioned in the right end of the chain ($n = 20$) is fixed to the rigid wall. The shaker is excited by a single step voltage to inject compressive impact to the system. To obtain the dynamic folding/unfolding motion of each unit cell, we use six action cameras (GoPro HERO 4 BLACK) whose maximum frame rate is mere 240 fps (see the lower inset of Fig. 7.7 A, and also Appendix C for the detail information). By using three pairs of the GoPro cameras, we split the field of view of the entire origami system by three and capture the axial and rotational motions of the TCO cells based on the stereo vision. To facilitate detection of the motions, we attach fluorescent green spherical markers to each interfacial polygon (see the inset in Fig. 7.1 C). The weight and moment of inertia of the interfacial polygon including a sleeve bearing and markers are 49.4 g and 5.32 $\times 10^{-5}$ kg m^2, respectively. The weight of the triangulated facets made of paper is 3.6 g, therefore the inertia of the side facets are negligible compared to the polygon.

The digital images in Fig. 7.7 B show the snapshots of the first eight TCO unit cells at four different time frames captured by the first pair of the action cameras. In this figure, the length of the arrows represents the velocity of the polygon in the axial direction, and red (blue) color denotes the rightward (leftward) direction. For the sake of visualization, the 3D images are reconstructed based on the experiment data as shown in the right column in Fig. 7.7 B, where red (blue) color indicates compressive (tensile) strain. Here, the strain value of the nth cell is defined by $(u_n - u_{n+1})/h_0$ where u_n (u_{n+1}) is the axial displacement of its left (right) polygon, such that compressive (tensile) strains take positive (negative) signs for convenience. Also, the deformed shapes are scaled 2.5 time larger than original deformation for visual clarity. From the experimental results, we observe that initially, the first unit

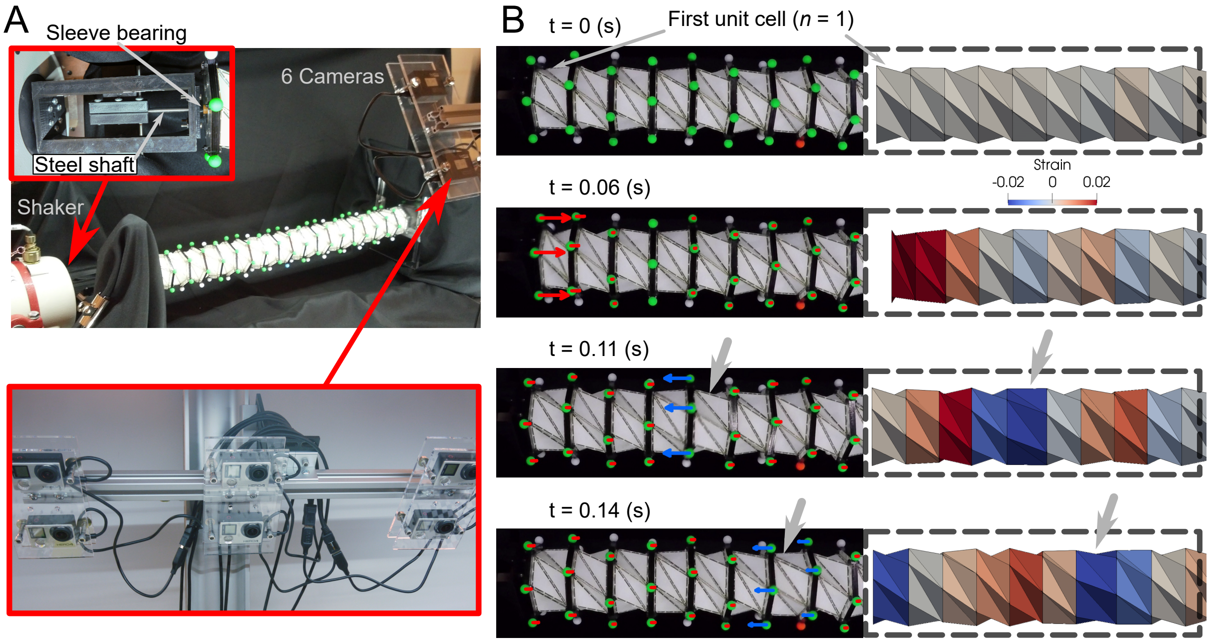

Figure 7.7: Experimental setup and digital image correlation (DIC) analysis results. (**a**) The shaker is attached to the left-most unit cell through the sleeve bearing (upper right inset). The folding motion of each unit cell is captured by six action cameras (lower inset). For DIC analysis, the fluorescent green markers are used. (**b**) Snapshots of the experiment at $t = 0$, 0.06, 0.11, 0.14 s. Images from the camera are shown in the left column where the arrow represents the velocity vector of the polygon in the axial direction. 3D reconstruction of the TCO chain (right column). The deformation is scaled 2.5 times larger than the original deformation for visual clarity. Arrows indicate the propagation of the rarefaction solitary wave.

shows the large-amplitude compression due to the excitation by the shaker. However, this compressive motion decays quickly without being robustly transmitted to the right, whereas the noticeable tensile motion is evolved instead (see the arrows in Fig. 7.7 B).

To better understand this interesting wave dynamics, we plot the measured strains in time and space domains (Fig. 7.8 A). We observe that after the compressive impact is applied to the front end of the system, this origami system creates two different types of mechanical waves: small-amplitude and fast-traveling oscillatory waves (see small ripples in $t < 0.2$ s in Fig. 7.8 A), and large-amplitude and slow-traveling, tsunami-like waves (high spikes and dips). The separation of waves into such two groups arises from the two degree-of-freedom nature of the TCO cells with coupled dynamics between axial and rotational motions (see the reference [38] for wave mixing effects in such settings). While the former wave group is interesting on its own right, in this study, we focus on the slower but larger-amplitude mechanical waves from a perspective of designing effective impact mitigation system. If we limit our scope to this, we find interestingly in Fig. 7.7 A that the primary wave that the last TCO cell ($n = 20$) experiences is a tensile wave despite the application of compressive impact to the system.

For computational investigation, we formulate the equations of motions for the entire chain based on the simplified model of the TCO cells (see Appendix B for details) and solve them numerically by using the Runge-Kutta method. The simulation results are shown in Fig. 7.8 B, which show an excellent agreement with the experimental results. These equations of motions can be further reduced to a 1D model by considering the first eigen-mode of the single TCO unit cell (see the dashed line in the inset of Fig. 7.6 C). We take the continuum limit of the equations given the infinite TCO chain, and then, we reach the mathematical expression that shows this TCO-based system can be approximated into the well-known KdV equation (see Appendix D for details). This equation supports solitary wave solutions, thereby analytically confirming the existence of the rarefaction solitary waves propagating in the origami-based system.

To take into account damping effects in the system (e.g., material dissipation and friction), we consider the leading-order solitary wave solution for the damped KdV equation, in which we introduce an exponential damping factor ν [68,69] (see Appendix D). We determine ν by conducting curve-fitting to the experimental amplitude of the rarefaction solitary wave in space (red dots in Fig. 7.8 C). As a result, the black solid curve is obtained from the damped KdV solution ($\nu = 13.8\ \mathrm{s}^{-1}$). Note that the numerical results in Fig. 7.8 B adopted this damping factor for accounting for damping in simulations. We find that this results in the reasonably close trend of the strain attenuation in numerics compared to experiments and analysis. If we analyze the attenuation trend of the leading compressive wave, how-

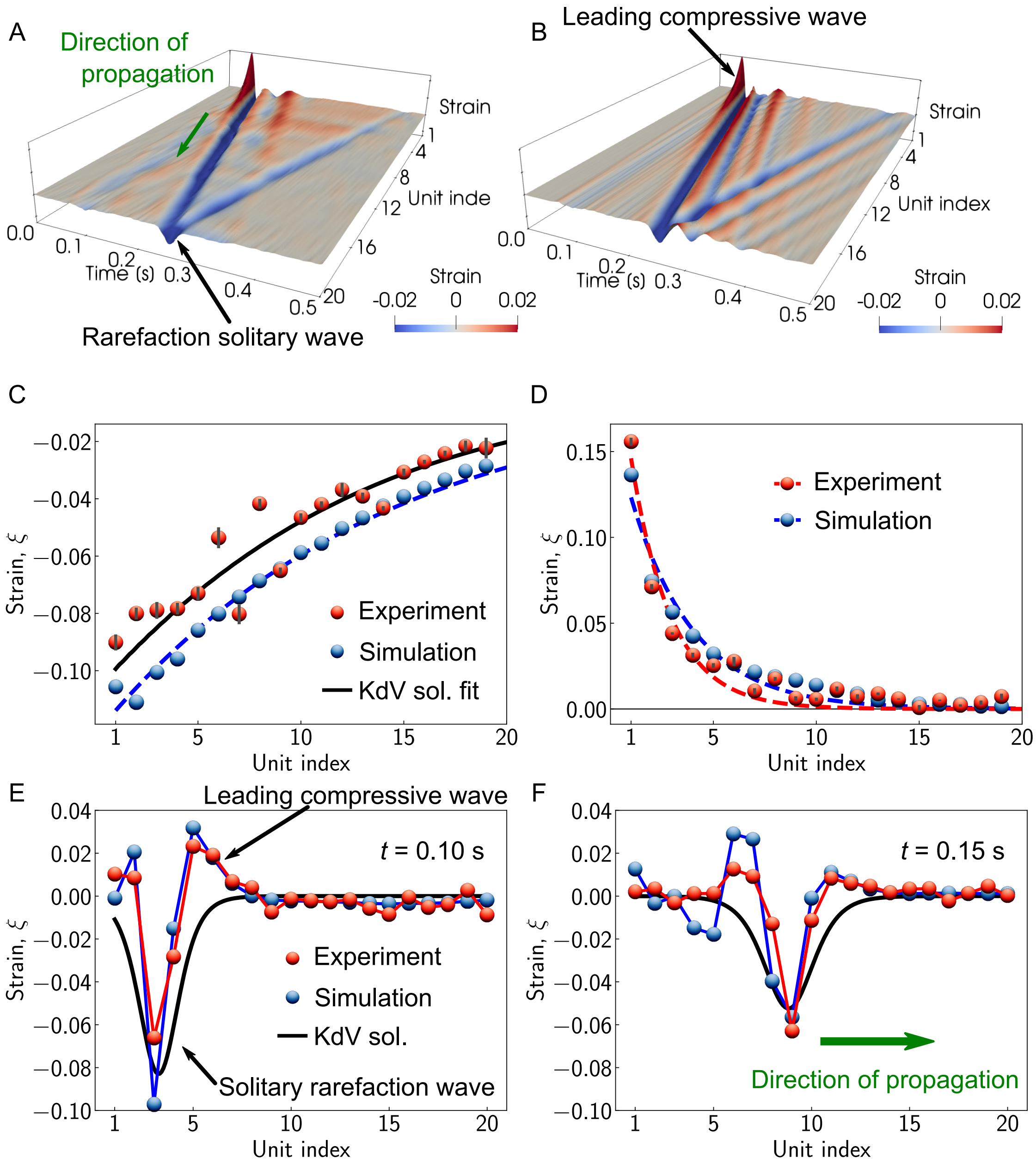

Figure 7.8: Wave form analysis. (**a**) The space-time contour plot of the experimentally measure strain wave propagation in the origami-based system. The black arrow indicates the rarefaction solitary wave, and the green shows the direction of the propagation. (**b**) Numerical simulation results show a qualitative agreement with the experimental data. The black arrow indicates the leading compresive wave in front of the rarefaction wave. (**c**) The amplitude change of the rarefaction solitary wave. The experimental data is fitted by the KdV solution (black curve) to obtain the damping coefficient for numerical and analytical analysis. The errorbar is s.d. calculated from five measurements. (**d**) The amplitude of the leading compression is analyzed. The dashed curves are obtained from the exponential fit to the experimental and numerical data. The shape of the rarefaction solitary wave (**e**) at $t = 0.10$ s and (**f**) $t = 0.15$ s are shown.

ever, we find that the numerical simulation yields better agreement with the experimental observation as shown in Fig. 7.8 D. Comparing the attenuation trends of the leading tensile and compressive waves (Figs. 7.8 C and D), we observe the compressive component decays more drastically than the tensile counterpart. The compressive waves show an order-of-magnitude reduction in its amplitude within 10 TCO cells. This manifests the efficacy of the origami-based metamaterial for efficient mitigation of compressive impact.

In Figs. 7.8 E and F, we show the temporal plots of the strain waves at $t = 0.10$ and 0.15 s. In these plots, the compressive waves are attenuated significantly, while the tensile ones are propagating more dominantly and robustly. Although the analytical expression predicts the rarefaction solitary wave with a wider width, we observe a qualitative agreement among analytical, numerical, and experimental results. One interesting finding here is that the maximum compressive strain is ahead of the rarefaction solitary wave at $t = 0.10$ s, but the peak is shifted to the rear part of the solitary wave at $t = 0.15$ s. This indicates that the rarefaction solitary wave propagates faster than the other compressive wave packets, and eventually overtakes the initial compressive strain wave. While such overtaking behavior has been previously studied numerically [55, 58], this is the first experimental observation in mechanical platforms.

We further investigate the overtaking behavior by calculating the wave speeds of both tensile and compressive components. To this end, we conduct numerical simulations for a longer chain composed of 50 unit cells (see Fig. 7.9 A and its inset for the magnified view). We evidently observe the overtaking phenomenon around the fifth cell location, verifying the larger speed of the rarefaction solitary wave than that of the compressive one. To quantify the speeds, we extract the time and location of the maximum peak of the rarefaction solitary and compressive strain waves as shown in Fig. 7.9 B. As marked by the circle in the figure, we detect the overtaking moment around $t = 0.11$ s, when the trajectories of solitary wave and maximum compression peak are crossing. The slope of each curve represents the wave speed, therefore the wave speed of the rarefaction solitary wave can be calculated from the experimental and numerical results. Figure 7.9 C shows the wave speed calculated from the experiment (20 units) and simulation (50 units), and the result is compared with the prediction from the KdV solution. In addition, the speed of the sound of the system is calculated from the linear analysis (see Appendix D). We observe that the experimental and numerical results corroborate the analytical prediction. Also, our analysis reveals that the wave speed of the rarefaction solitary wave is larger than the speed of sound, therefore this rarefaction solitary wave is evidently supersonic.

7.3 Conclusion

In conclusion, we have studied experimentally, numerically, and analytically unique nonlinear wave propagation in mechanical metamaterials made of the Triangulated Cylindrical Origami (TCO) cells. We found that the TCO-based metamaterials exhibit the rarefaction solitary wave propagating ahead of the initial compressive strain despite the application of compressive impact. Also, the initial compressive strain is attenuated significantly, which can be highly beneficial for impact mitigation application. While we focused on the monoatomic TCO unit cells with strain-softening behavior in this study, the origami-based system has great potential for supporting rich wave dynamics by introducing heterogeneous elements (e.g., hardening, multi-stable, and impurity components) in the chain. Also, the findings in this 1D setting can be further extended to multi-dimensions in a modular way. We believe that this versatile platform composed of volumetric origami structures can be used for a wide range of applications such as impact/shock mitigation, vibration filtering, and energy harvesting.

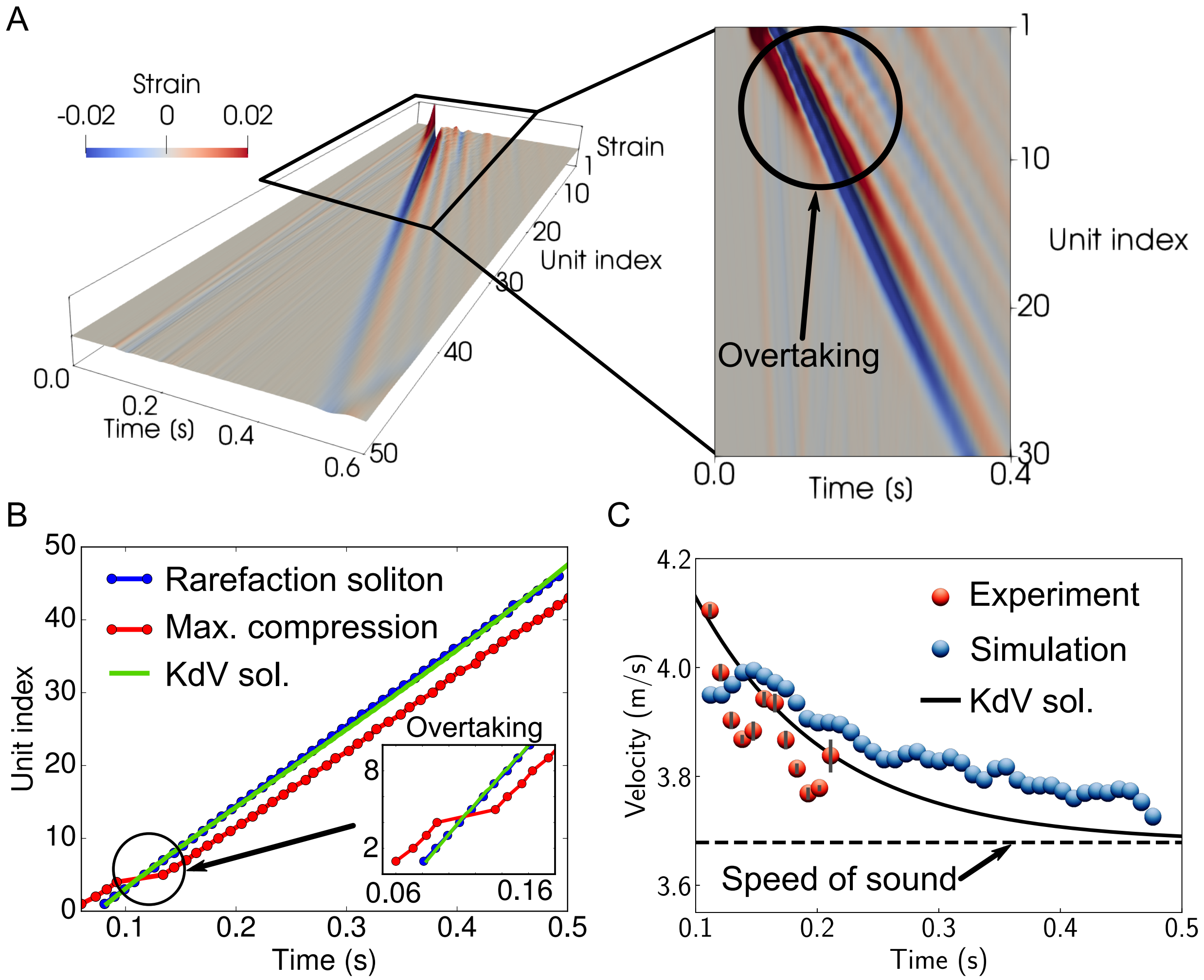

Figure 7.9: Wave speed analysis. (**a**) Space-time contour plot of the strain wave for the numerical simulation conducted on the longer chain composed of 50 TCO unit cells. Magnified view of the overtaking moment is shown in the right inset. (**b**) Trajectory of the rarefaction solitary wave (denoted by the blue markers) and the maximum compressive strain wave (red markers) shows the overtaking behavior of the rarefaction solitary wave. The green line indicates the analytical prediction from the KdV equation. (**c**) Wave speed of the rarefaction solitary wave is larger than the speed of sound of the medium, which means supersonic behavior.

Chapter 8

FUTURE EXPLORATION OF ORIGAMI-BASED STRUCTURES

We have studied numerically, analytically, and experimentally unique static/dynamic response of origami-based mechanical metamaterials made of the Tachi-Miura Polyhedron (TMP) and Triangulated Cylindrical Origami (TCO) cells. From the static analysis, we have found the following unique mechanical properties:

- The TMP structure exhibits tunable positive/negative Poisson's ratio depending on the geometrical parameters and initial shape of the unit cell. This transition between positive and negative Poisson's ratio has been predicted analytically and measured experimentally.

- For the application of lateral loading to the TMP structure, we observe the transition between flat-foaldable in two directions to increasing stiff configurations which means that the structure becomes extremely difficult to fold in a practical sense. We found this behavior analytically.

- The TCO unit cell possesses tailorable four distinctively different behaviors: mono-/bistable behavior, zero-stiffness mode, and bifurcation configurations. These four configurations have been verified experimentally.

Based on these unconventional static behaviors, we have designed the two different types of the discrete chain composed of the TMP or TCO unit cells. We have conducted dynamic analysis on these two chains and the important findings are summarized as follows:

- Both TMP-/TCO-based system show frequency band structure if the system consists of two different configurations of the origami unit cells. This frequency band gap has been investigated numerically and analytically.

- TCO-based chain exhibits wave mixing behavior due to the coupling of axial and rotational motions of the TCO unit cell. This wave mixing has been analyzed numerically.

- Both TMP-/TCO-based chain support the rarefaction solitary wave, tsunami-like nonlinear wave propagation, arising from strain-softening nature of each unit cell. We have confirmed this unique wave propagation numerically.

- The rarefaction solitary wave with overtaking behavior, i.e., the tensile solitary wave overtakes the initially leading compressive strain waev, has been verified analytically, numerically, and experimentally.

While we focused on one dimensional chain of the TMP/TCO sturcutres in this thesis, the origami-based system has great potential for constructing two or three dimensional metamaterials with rich wave dynamics by stacking the unit cells in vertical/horizontal directions. One of the feasible extension of the TMP is the multi-TMP cellular structure as we discuss in Chapter 2. Figure 8.1 shows the preliminary prototype made of acrylic plates and stainless steel shafts. The next step should be experimental evaluation of the prototype in static compression tests and dynamic analysis such as vibration test and impact response.

To extend the TCO-based mechanical metamaterial concept to multi-dimensions, one of the possible idea would be arranging the TCO unit cells in a planer direction and connecting the polygon of neighboring unit cells by linear spring elements as shown in Fig. 8.2A. In this way, the rotational motion of each polygon is transmitted to other neighboring unit cells. One of the interesting research direction is to examine the different types of interactions between adjacent unit cells. For example, depending on the installation point of the linear spring, the direction of the rotational motion transmitted to neighboring cells would be different.

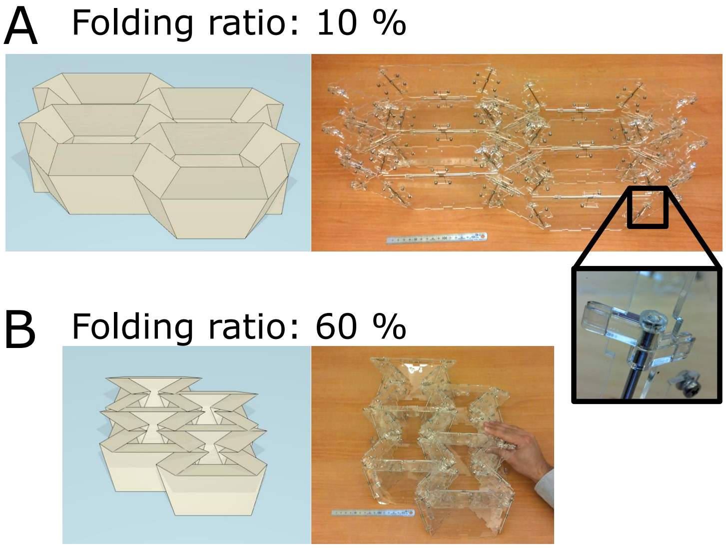

Figure 8.1: Prototype of 2×2 multi-TMP cellular structure. The illustration of 2×2 multi-TMP unit cells (Left column) and photograph of the corresponding configuration (Right) for folding ratio of (**a**) 10 % and (**b**) 60% are shown. The inset photograph shows the enlarged image of the laser-cut acrylic hinge and a strain steel shaft.

It would be interesting to explore wave dynamics in this extended 2D TCO system with different interaction behaviors.

Another interesting extension of this research is the use of different materials and dimensions for prototype fabrication. Currently, origami-based structure has been fabricated mostly by paper sheets. To develop practical engineering applications, new prototype fabrication techniques need to be investigated by preserving the unique mechanical responses of origami. Since the TMP is a single-DOF structure, it can be constructed by using metal sheets (see Fig. 8.3). However, the thickness of actual materials causes the discrepancy between rigid origami assumption and physical prototypes, which prohibits smooth implementation of origami design principles into real engineering applications. Therefore, the origami design principle based on thick materials could drastically enhance the use of origami in engineering.

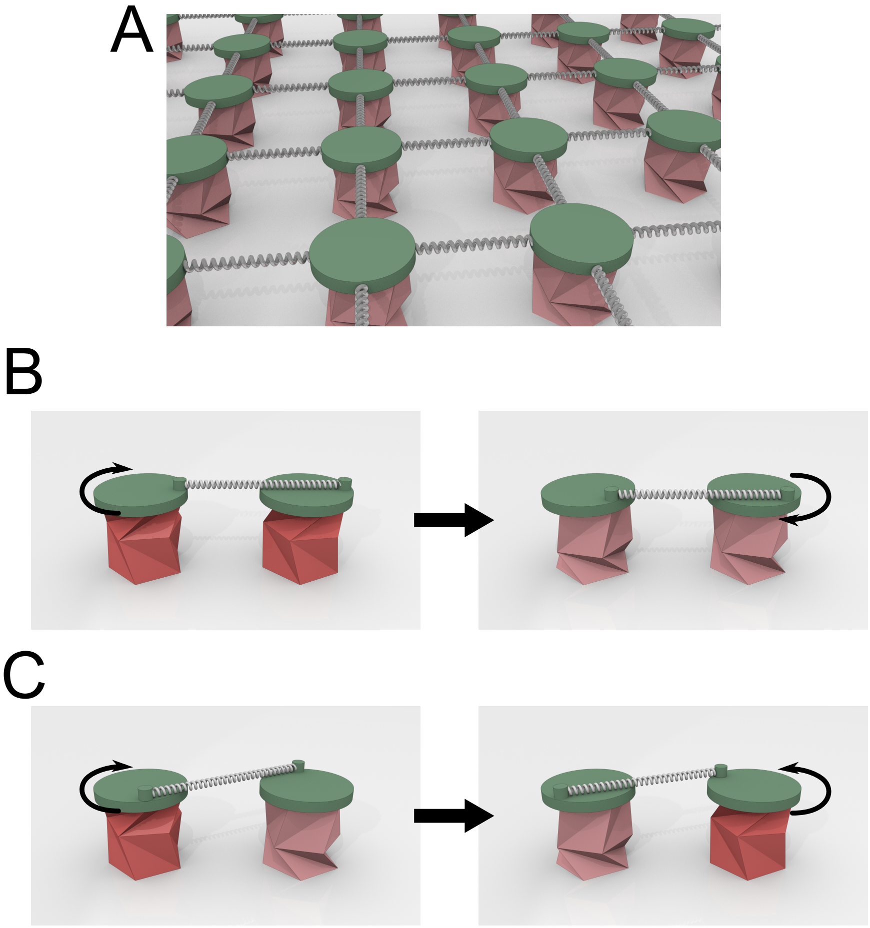

Figure 8.2: Conceptual illustration of the extension of the TCO-based mechanical metamaterials. (**a**) Planer extension of the TCO mematerials in which the top surfaces are connected by linear springs. (**b**) Different interactions between neighboring unit cells. The top polygons of two neighboring units are connected by a linear spring. If we apply clock-wise torque to the left unit cell, the right cell also rotates in a clock-wise direction. (**c**) If we connect two adjacent unit cells in a diagonal direction and apply the same torque to the left unit cell, the right rotates in a counter clock-wise manner.

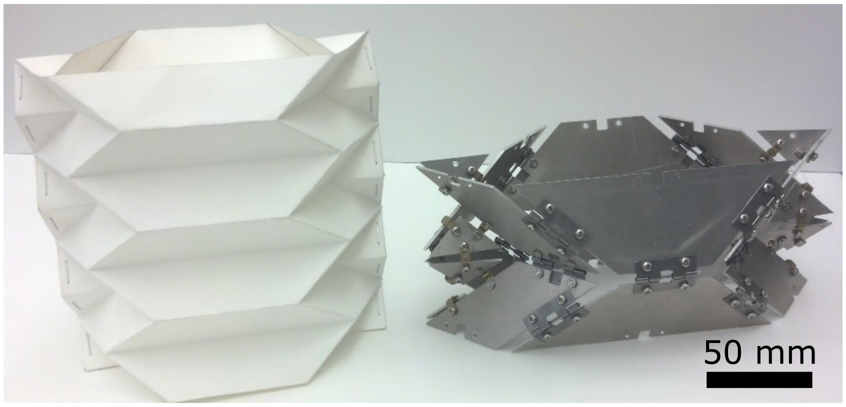

Figure 8.3: Prototype of the TMP single unit cells. (**Left**) Paper prototype of the TMP structure with $\alpha = 45°$). (**Right**) The prototype made of aluminum plates and hinges.

Based on the research finding in this thesis, this versatile platform composed of volumetric origami structures, together with new fabrication technique dealing with these challenges, can be used a wide range of applications such as impact/shock mitigation, vibration filtering, and energy harvesting.

BIBLIOGRAPHY

[1] K. Miura. Method of packaging and deployment of large membranes in space. *The Institute of Space and Astronautical Science Report No.618*, pages 1–9, 1985.

[2] Y. Tsuda, O. Mori, R. Funase, H. Sawada, T. Yamamoto, T. Saiki, T. Endo, and J. Kawaguchi. Flight status of IKAROS deep space solar sail demonstrator. *Acta Astronautica*, 69(9-10):833–840, 2011.

[3] S. A. Zirbel, R. J. Lang, M. W. Thomson, D. A. Sigel, P. E. Walkemeyer, B. P. Trease, S. P. Magleby, and L. L. Howell. Accommodating thickness in origami-based deployable arrays. *Journal of Mechanical Design*, 135(11):111005, 2013.

[4] L. Mahadevan and S. Rica. Self-organized origami. *Science*, 307:1740, 2005.

[5] H. Kobayashi, B. Kresling, and J. F. V. Vincent. The geometry of unfolding tree leaves. *Proceedings of the Royal Society B: Biological Sciences*, 265(1391):147–154, 1998.

[6] K. Saito, S. Yamamoto, M. Maruyama, and Y. Okabe. Asymmetric hindwing foldings in rove beetles. *Proceedings of the National Academy of Sciences*, 111(46):16349–16352, 2014.

[7] I. Mikó, R. S. Copeland, J. P. Balhoff, M. J. Yoder, and A. R. Deans. Folding wings like a cockroach: a review of transverse wing folding ensign wasps (Hymenoptera: Evaniidae: Afrevania and Trissevania). *PloS one*, 9(5):e94056, 2014.

[8] K. Saito, S. Nomura, S. Yamamoto, R. Niyama, and Y. Okabe. Investigation of hindwing folding in ladybird beetles by artificial elytron transplantation and microcomputed tomography. *Proceedings of the National Academy of Sciences*, 114(22):5624–5628, 2017.

[9] T. Tachi. Origamizing polyhedral surfaces. *IEEE Transactions on Visualization and Computer Graphics*, 16(2):298–311, 2010.

[10] K. Miura. Proposition of pseudo-cylindrical concave polyhedral shells. In *Proceedings of IASS Symposium on Folded Plates and Prismatic Structures, International Association for Shell Structures*, Vienna, Austria, 1970.

[11] S. Miyashita, S. Guitron, M. Ludersdorfer, C. R. Sung, and D. Rus. An untethered miniature origami robot that self-folds, walks, swims, and degrades. In *2015 IEEE International Conference on Robotics and Automation (ICRA)*, pages 1490–1496, 2015.

[12] J. T. B. Overvelde, J. C. Weaver, C. Hoberman, and K. Bertoldi. Rational design of reconfigurable prismatic architected materials. *Nature*, 541(7637):347–352, 2017.

[13] K. Kuribayashi-Shigetomi, H. Onoe, and S. Takeuchi. Cell origami: self-folding of three-dimensional cell-laden microstructures driven by cell traction force. *PloS one*, 7(12):e51085, 2012.

[14] J. H. Lee, J. P. Singer, and E. L. Thomas. Micro-/nanostructured mechanical metamaterials. *Advanced Materials*, 24(36):4782–4810, 2012.

[15] M. Wegener. Metamaterials beyond optics. *Science*, 342(6161):939–940, 2013.

[16] J. Paulose, A. S. Meeussen, and V. Vitelli. Selective buckling via states of self-stress in topological metamaterials. *Proceedings of the National Academy of Sciences of the United States of America*, 112(25):7639–44, 2015.

[17] G. Ma and P. Sheng. Acoustic metamaterials: From local resonances to broad horizons. *Science Advances*, 2(2):e1501595–e1501595, 2016.

[18] C. Coulais, D. Sounas, and A. Alù. Static non-reciprocity in mechanical metamaterials. *Nature*, 542(7642):461–464, 2017.

[19] M. Schenk and S. D. Guest. Geometry of Miura-folded metamaterials. *Proceedings of the National Academy of Sciences*, 110(9):3276–3281, 2013.

[20] C. Lv, D. Krishnaraju, G. Konjevod, H. Yu, and H. Jiang. Origami based mechanical metamaterials. *Scientific reports*, 4:5979, 2014.

[21] K. C. Cheung, T. Tachi, S. Calisch, and K. Miura. Origami interleaved tube cellular materials. *Smart Materials and Structures*, 23(9):094012, 2014.

[22] S. Waitukaitis, R. Menaut, B. G. Chen, and M. van Hecke. Origami multistability: From single vertices to metasheets. *Physical Review Letters*, 114(5):055503, 2015.

[23] J. L. Silverberg, A. A. Evans, L. McLeod, R. C. Hayward, T. C. Hull, C. D. Santangelo, and I. Cohen. Using origami design principles to fold reprogrammable mechanical metamaterials. *Science*, 345(6197):647–650, 2014.

[24] M. Schenk, S. D. Guest, and G. J. McShane. Novel stacked folded cores for blast-resistant sandwich beams. *International Journal of Solids and Structures*, 51(25-26):4196–4214, 2014.

[25] E. T. Filipov, T. Tachi, and G. H. Paulino. Origami tubes assembled into stiff, yet reconfigurable structures and metamaterials. *Proceedings of the National Academy of Sciences*, 112:12321–12326, 2015.

[26] K. Miura and T. Tachi. Synthesis of rigid-foldable cylindrical polyhedra. *Journal of the International Society for the Interdisciplinary Study of Symmetry*, pages 204–213, 2010.

[27] T. Tachi and K. Miura. Rigid-foldable cylinders and cells. *Journal of the International Association for Shell and Spatial Structures (IASS)*, 53(4):217–226, 2012.

[28] H. Yasuda, T. Yein, T. Tachi, K. Miura, and M. Taya. Folding behaviour of Tachi-Miura polyhedron bellows. *Proceedings of the Royal Society A: Mathematical Physical and Engineering*, 469(2159):20130351, 2013.

[29] B. H. Hanna, J. M. Lund, R. J. Lang, S. P. Magleby, and L. L. Howell. Waterbomb base: a symmetric single-vertex bistable origami mechanism. *Smart Materials and Structures*, 23(9):094009, 2014.

[30] S. D. Guest and S. Pellegrino. The folding of triangulated cylinders, Part I: Geometric considerations. *Journal of Applied Mechanics*, 61:773–777, 1994.

[31] G. W. Hunt and I. Ario. Twist buckling and the foldable cylinder: an exercise in origami. *International Journal of Non-Linear Mechanics*, 40(6):833–843, 2005.

[32] J. Song, Y. Chen, and G. Lu. Axial crushing of thin-walled structures with origami patterns. *Thin-Walled Structures*, 54:65–71, 2012.

[33] J. Ma and Z. You. Energy absorption of thin-walled square tubes with a prefolded origami patternPart I: Geometry and numerical simulation. *Journal of Applied Mechanics*, 81(1):011003, 2014.

[34] S. Ishida, H. Uchida, and I. Hagiwara. Vibration isolators using nonlinear spring characteristics of origami-based foldable structures. *Transactions of The Japan Society of Mechanical Engineers*, 80(820):1–11, 2014.

[35] B. Kresling. Plant design: mechanical simulations of growth patterns and bionics. *Biomimetics*, 3(3):105–122, 1995.

[36] X. Zhao, H. Yabo, and I. Hagiwara. Optimal design for crash characteristics of cylindrical thin-walled structure using origami engineering. *Transactions of The Japan Society of Mechanical Engineers Series A*, 76(761):10–17, 2010.

[37] C. Jianguo, D. Xiaowei, Z. Ya, F. Jian, and T. Yongming. Bistable behavior of the cylindrical origami structure with kresling pattern. *Journal of Mechanical Design*, 137(6):061406, 2015.

[38] G. Y. Lee, C. Chong, P. G. Kevrekidis, and J. Yang. Wave mixing in coupled phononic crystals via a variable stiffness mechanism. *Journal of the Mechanics and Physics of Solids*, 95:501–516, 2016.

[39] R. Chaunsali, F. Li, and J. Yang. Stress wave isolation by purely mechanical topological phononic crystals article. *Scientific Reports*, 6(1):30662, 2016.

[40] M. Ruzzene, F. Scarpa, and F. Soranna. Wave beaming effects in two-dimensional cellular structures. *Smart Materials and Structures*, 12(3):363–372, 2003.

[41] L. Dong and R. S. Lakes. Advanced damper with negative structural stiffness elements. *Smart Materials and Structures*, 21(7):075026, 2012.

[42] P. Wang, F. Casadei, S. Shan, J. C. Weaver, and K. Bertoldi. Harnessing buckling to design tunable locally resonant acoustic metamaterials. *Physical Review Letters*, 113(1):014301, 2014.

[43] C. Zhou, B. Wang, J. Ma, and Z. You. Dynamic axial crushing of origami crash boxes. *International Journal of Mechanical Sciences*, 118:1–12, 2016.

[44] Itseez. Open source computer vision library, 2015.

[45] Z. Y. Wei, Z. V. Guo, L. Dudte, H. Y. Liang, and L. Mahadevan. Geometric mechanics of periodic pleated origami. *Physical Review Letters*, 110(21):215501, 2013.

[46] H. Yasuda and J. Yang. Reentrant origami-based metamaterials with negative Poisson's ratio and bistability. *Physical Review Letters*, 114(18):1–5, 2015.

[47] C. A. Schneider, W. S. Rasband, and K. W. Eliceiri. NIH Image to ImageJ: 25 years of image analysis. *Nature Methods*, 9(7):671–675, 2012.

[48] H. Yasuda, T. Tachi, M. Lee, and J. Yang. Origami-based tunable truss structures for non-volatile mechanical memory operation. *Nature Communications*, 8:962, 2017.

[49] H. Yasuda, M. Lee, and J. Yang. Tunable wave dynamics in origami-based mechanical metamaterials. In *Proceedings of the ASME 2016 International Design Engineering Technical Conferences and Computers and Information in Engineering Conference*, page V05BT07A012, 2016.

[50] T. Aprille and T. Trick. A computer algorithm to determine the steady-state response of nonlinear oscillators. *IEEE Transactions on Circuit Theory*, 19(4):354–360, 1972.

[51] F. C. Moon. *Applied dynamics : with applications to multibody and mechatronic systems.* New York : Wiley, New York, 1998.

[52] L. Brillouin. *Wave propagation in periodic structures: electric filters and crystal lattices.* New York: Dover Publications, 1946.

[53] A. Nayfeh and D. T. Mook. *Nonlinear oscillations.* New York: Wiley, 1946.

[54] H. Yasuda and J. Yang. Tunable frequency band structure of origami-based mechanical metamaterials. *Journal of the International Association for Shell and Spatial Structures*, 58(4):287–294, 2017.

[55] H. Yasuda, C. Chong, E. G. Charalampidis, P. G. Kevrekidis, and J. Yang. Formation of rarefaction waves in origami-based metamaterials. *Physical Review E*, 93:043004, 2016.

[56] É. Falcon, C. Laroche, and S. Fauve. Observation of depression solitary surface waves on a thin fluid layer. *Physical Review Letters*, 89(20):204501, 2002.

[57] P. Lax. *Hyperbolic systems of conservation laws and the mathematical theory of shock waves.* Society for Industrial and Applied Mathematics, 1973.

[58] E. B. Herbold and V. F. Nesterenko. Propagation of rarefaction pulses in discrete aterials with Strain-Softening Behavior. *Physical Review Letters*, 110(14):144101, 2013.

[59] V. F. Nesterenko. *Dynamics Of heterogeneous materials.* Springer-Verlag New York Inc., 2001.

[60] S Sen, J Hong, J Bang, E Avalos, and R Doney. Solitary waves in the granular chain. *Physics Reports*, 462(2):21–66, 2008.

[61] P. G. Kevrekidis. Non-linear waves in lattices: past, present, future. *IMA Journal of Applied Mathematics*, 76(3):389–423, 2011.

[62] F. Fraternali, G. Carpentieri, A. Amendola, R. E. Skelton, and V. F. Nesterenko. Multiscale tunability of solitary wave dynamics in tensegrity metamaterials. *Applied Physics Letters*, 105(20):201903, 2014.

[63] E. Fermi, J. Pasta, and S. Ulam. Studies of nonlinear problems. i. *(Los Alamos National Laboratory, Los Alamos, NM, USA)*, Tech. Rep.:LA–1940, 1955.

[64] D. K. Campbell, P. Rosenau, and G. M. Zaslavsky. Introduction: The Fermi-Pasta-Ulam problem - The first fifty years. *Chaos*, 15(1):015101, 2005.

[65] F. P. R. Maurin and A. Spadoni. Low-frequency wave propagation in post-buckled structures. *Wave Motion*, 51(2):323–334, 2014.

[66] S. Flach and A. V. Gorbach. Discrete breathers - Advances in theory and applications. *Physics Reports*, 467(1-3):1–116, 2008.

[67] S. Aubry. Discrete breathers: Localization and transfer of energy in discrete Hamiltonian nonlinear systems. *Physica D: Nonlinear Phenomena*, 216:1–30, 2006.

[68] M. S. Janaki, B. Dasgupta, M. R. Gupta, and B. K. Som. Solitary magnetosonic waves with landau damping. *Physica Scripta*, 45(4):368–372, 1992.

[69] S. Ghosh, M. Ranjan Gupta, N. Chakrabarti, and M. Chaudhuri. Nonlinear wave propagation in a strongly coupled collisional dusty plasma. *Physical Review E*, 83(6):066406, 2011.

[70] Z. Liu, X. Zhang, Y. Mao, Y. Y. Zhu, Z. Yang, C. T. Chan, and P. Sheng. Locally resonant sonic materials. *Science*, 289(5485):1734–1736, 2000.

[71] M. Maldovan. Sound and heat revolutions in phononics. *Nature*, 503(7475):209–217, 2013.

[72] S. Felton, M. Tolley, E. Demaine, D. Rus, and R. J. Wood. A method for building self-folding machines. *Science*, 345(6197):644–646, 2014.

[73] J. T. B. Overvelde, T. A. Jong, Y. Shevchenko, S. A. Becerra, G. M. Whitesides, J. C. Weaver, C. Hoberman, and K. Bertoldi. A three-dimensional actuated origami-inspired transformable metamaterial with multiple degrees of freedom. *Nature Communications*, 7:10929, 2016.

[74] J. L. Silverberg, J. H. Na, A. A. Evans, B. Liu, T. C. Hull, C. D. Santangelo, R. J. Lang, R. C. Hayward, and I. Cohen. Origami structures with a critical transition to bistability arising from hidden degrees of freedom. *Nature materials*, 14(4):389–93, 2015.

[75] J. R. Raney, N. Nadkarni, C. Daraio, D. M. Kochmann, J. A. Lewis, and K. Bertoldi. Stable propagation of mechanical signals in soft media using stored elastic energy. *Proceedings of the National Academy of Sciences*, 113(35):9722–9727, 2016.

[76] M. Hiraiwa, M. A. Ghanem, S. P. Wallen, A. Khanolkar, A. A. Maznev, and N. Boechler. Complex contact-based dynamics of microsphere monolayers revealed by resonant attenuation of surface acoustic waves. *Physical Review Letters*, 116(19):198001, 2016.

[77] Y. Y. Chen, G. K. Hu, and G. L. Huang. An adaptive metamaterial beam with hybrid shunting circuits for extremely broadband control of flexural waves. *Smart Materials and Structures*, 25(10):105036, 2016.

[78] S. Shan, S. H. Kang, J. R. Raney, P. Wang, L. Fang, F. Candido, J. A. Lewis, and K. Bertoldi. Multistable architected materials for trapping elastic strain energy. *Advanced Materials*, 27:4296–4301, 2015.

[79] H. Lee, J. H. Oh, H. M. Seung, S. H. Cho, and Y. Y. Kim. Extreme stiffness hyperbolic elastic metamaterial for total transmission subwavelength imaging. *Scientific Reports*, 6(November 2015):24026, 2016.

[80] O. R. Bilal, A. Foehr, and C. Daraio. Reprogrammable phononic metasurfaces. *Advanced Materials*, 29(39):1700628, 2017.

[81] S. Babaee, J. T. B. Overvelde, E. R. Chen, V. Tournat, and K. Bertoldi. Reconfigurable origami-inspired acoustic waveguides. *Science Advances*, 2(11):e1601019, 2016.

[82] S. Zhang, L. Yin, and N. Fang. Focusing ultrasound with an acoustic metamaterial network. *Physical Review Letters*, 102(19):194301, 2009.

[83] B. Deng, J.R. Raney, V. Tournat, and K. Bertoldi. Elastic vector solitons in soft architected materials. *Physical Review Letters*, 118(20):204102, 2017.

[84] F. Maurin. Solitary waves in longitudinally wrinkled and creased helicoids. *International Journal of Non-Linear Mechanics*, 89:133–141, 2017.

Appendix A

EQUATION OF MOTION FOR THE TMP-BASED METAMATERIALS

We model a chain of N-TMP cells based on the simplified bar-linkage model described in Chapter 4. In this model, each unit cell is connected by pin joints, which are allowed to move along the z-axis. The center-of-mass coordinates of the two bars and the orientation angles for the j-th unit cell are (z_j^L, y_j^L, θ_j) and $(z_j^R, y_j^R, \pi - \theta_j)$, respectively. Let us regroup this set of coordinates in a vector form as follows:

$$\boldsymbol{r}_j = \begin{bmatrix} z_j^L & y_j^L & \theta_j & z_j^R & y_j^R & \pi - \theta_j \end{bmatrix}^T.$$

Then, the coordinate of the origami chain can be expressed as:

$$\boldsymbol{r} = \begin{bmatrix} \boldsymbol{r}_1^T & \cdots & \boldsymbol{r}_j^T & \cdots & \boldsymbol{r}_N^T \end{bmatrix}^T.$$

Introducing the general coordinate

$$\boldsymbol{q} = \begin{bmatrix} \theta_1 & \cdots & \theta_j & \cdots & \theta_N \end{bmatrix}^T,$$

the velocity vector $\boldsymbol{v}$ and the corresponding acceleration $\dot{\boldsymbol{v}}$ can be expressed as

$$\boldsymbol{v} = \dot{\boldsymbol{r}} = \boldsymbol{G}\dot{\boldsymbol{q}}, \quad \dot{\boldsymbol{v}} = \ddot{\boldsymbol{r}} = \dot{\boldsymbol{G}}\dot{\boldsymbol{q}} + \boldsymbol{G}\ddot{\boldsymbol{q}} \tag{A.1}$$

where

$$
\begin{aligned}
\boldsymbol{G} &= \begin{bmatrix} \boldsymbol{G}_1 & \boldsymbol{g}_2 & \cdots & \boldsymbol{g}_j & \cdots & \boldsymbol{g}_N \\ \boldsymbol{O}_{6\times1} & \boldsymbol{G}_2 & \vdots & \boldsymbol{g}_j & \vdots & \boldsymbol{g}_N \\ \vdots & \boldsymbol{O}_{6\times1} & \ddots & \vdots & \vdots & \vdots \\ \vdots & \vdots & \ddots & \boldsymbol{G}_j & \vdots & \vdots \\ \vdots & \vdots & \vdots & \ddots & \ddots & \vdots \\ \boldsymbol{O}_{6\times1} & \boldsymbol{O}_{6\times1} & \cdots & \cdots & \cdots & \boldsymbol{G}_N \end{bmatrix}, \\
\boldsymbol{G}_j &= [-3L\cos\theta_j \quad -L\sin\theta_j \quad 1 \\
&\qquad -L\cos\theta_j \quad -L\sin\theta_j \quad -1]^T, \\
\boldsymbol{g}_j &= \begin{bmatrix} -4L\cos\theta_j & 0 & 0 & -4L\cos\theta_j & 0 & 0 \end{bmatrix}^T, \\
\boldsymbol{O}_{6\times1} &= \begin{bmatrix} 0 & 0 & 0 & 0 & 0 & 0 \end{bmatrix}^T.
\end{aligned}
$$

If we fix the time and displacement under virtual velocity (i.e., $\delta\boldsymbol{q} = \boldsymbol{0}$ and $\delta t = 0$) [51], the variation of the velocity vector becomes

$$\delta\boldsymbol{v}_j = \sum_{k=1}^{N} \frac{\partial\boldsymbol{v}_j}{\partial\dot{q}_k}\delta\dot{q}_k. \tag{A.2}$$

Then the principle of virtual power is expressed by

$$\sum_{j=1}^{N} \left(\hat{\boldsymbol{M}}_j\dot{\boldsymbol{v}}_j - \boldsymbol{f}_j\right)\delta\boldsymbol{v}_j = 0 \tag{A.3}$$

where $\hat{\boldsymbol{M}}_j$ is a mass matrix expressed as

$$\hat{\boldsymbol{M}}_j = \operatorname{diag}\begin{bmatrix} m & m & J & m & m & J \end{bmatrix},$$

and J is the bar's moment of inertia ($J = mL^2/3$). Also, $\boldsymbol{f}_j$ is a force vector defined as follows

$$\boldsymbol{f}_j = \begin{cases} [F^{ex}, \quad 0, \quad -2k_\theta\left(\theta_1 - \theta_{1,0}\right) - F^{ex}L\cos\theta_1, & \\ \quad 0, \quad 0, \quad -2k_\theta\left(\theta_{1,0} - \theta_1\right)] & \text{if } j = 1 \\ [0, \quad 0, \quad -2k_\theta\left(\theta_j - \theta_{j,0}\right), & \\ \quad 0, \quad 0, \quad -2k_\theta\left(\theta_{j,0} - \theta_j\right)] & \text{if } j = 2\ldots N \end{cases}$$

where $\theta_{j,0}$ is the initial folding angle of the j-th unit cell (i.e., no torque applied at the hinge in this initial angle), and F^{ex} is the external force applied to the first unit cell as shown in Fig.4.1(b). The advantage of the principle of virtual power is that we can apply it to a system with both motion and geometrical constraints, and we can derive the equation of motion without considering force constraints.

Substituting Eq. (A.2) into Eq. (A.3), we obtain

$$\sum_{k=1}^{N}\left[\sum_{j=1}^{N}\left(\hat{\boldsymbol{M}}_j\dot{\boldsymbol{v}}_j-\boldsymbol{f}_j\right)\frac{\partial \boldsymbol{v}_j}{\partial \dot{q}_k}\right]\delta\dot{q}_k=0.$$

Therefore

$$\sum_{j=1}^{N}\left(\hat{\boldsymbol{M}}_j\dot{\boldsymbol{v}}_j-\boldsymbol{f}_j\right)\frac{\partial \boldsymbol{v}_j}{\partial \dot{q}_k}=0$$

where $k=1,\ \ldots,N$. Then

$$\boldsymbol{G}^T\hat{\boldsymbol{M}}\dot{\boldsymbol{v}}=\boldsymbol{G}^T\boldsymbol{f}. \tag{A.4}$$

where

$$\begin{aligned}\hat{\boldsymbol{M}} &= \operatorname{diag}\left[\hat{\boldsymbol{M}}_1 \quad \cdots \quad \hat{\boldsymbol{M}}_N\right],\\ \boldsymbol{f} &= \left[\boldsymbol{f}_1 \quad \cdots \quad \boldsymbol{f}_j \quad \cdots \quad \boldsymbol{f}_N\right]^T\end{aligned}$$

Substituting Eq. (A.1) into Eq. (A.4), we obtain the equation of motion as follows:

$$\boldsymbol{G}^T\hat{\boldsymbol{M}}\boldsymbol{G}\ddot{\boldsymbol{q}}+\boldsymbol{G}^T\hat{\boldsymbol{M}}\dot{\boldsymbol{G}}\dot{\boldsymbol{q}}=\boldsymbol{G}^T\boldsymbol{f}. \tag{A.5}$$

To obtain the equation of motion of a unit cell, let us consider a simple case of $N=1$. The position and velocity vectors of the two rigid bars in the unit cell (see Fig.4.1(b)) are

$$\begin{aligned}(z_1,y_1)&=(-3L\sin\theta_1, L\cos\theta_1)\\ (z_2,y_2)&=(-L\sin\theta_1, L\cos\theta_1)\\ (\dot{z}_1,\dot{y}_1)&=(-3L\dot{\theta}_1\cos\theta_1, -L\dot{\theta}_1\sin\theta_1)\\ (\dot{z}_2,\dot{y}_2)&=(-L\dot{\theta}_1\cos\theta_1, -L\dot{\theta}_1\sin\theta_1).\end{aligned}$$

Note that the origin of z-axis is located at the fixed wall. Then, we obtain

$$\begin{aligned} \boldsymbol{G} = \quad & [-3L\cos\theta_1 \quad -L\sin\theta_1 \quad 1 \\ & -L\cos\theta_1 \quad -L\sin\theta_1 \quad -1]^T, \\ \dot{\boldsymbol{G}} = \quad & [3L\dot{\theta}_1\sin\theta_1 \quad -L\dot{\theta}_1\cos\theta_1 \quad 0 \\ & L\dot{\theta}_1\sin\theta_1 \quad -L\dot{\theta}_1\cos\theta_1 \quad 0]^T. \end{aligned}$$

Also, the force vector is expressed as:

$$\begin{aligned} \boldsymbol{f} = & [F^{ex}, \quad 0, \quad -2k_\theta\left(\theta_1 - \theta_{1,0}\right) - F^{ex}L\cos\theta_1, \\ & 0, \quad 0, \quad -2k_\theta\left(\theta_{1,0} - \theta_1\right)]^T. \end{aligned}$$

Plugging these expressions into Eq. (A.5), we finally obtain the equation of motion of the single unit cell as

$$\begin{aligned} \left(mL^2/2 + J/2 + 2mL^2\cos^2\theta_1\right)\ddot{\theta}_1 - mL^2\dot{\theta}_1^2\sin 2\theta_1 \\ +k_\theta\left(\theta_1 - \theta_{1,0}\right) = -F^{ex}L\cos\theta_1. \end{aligned} \tag{A.6}$$

Here, we consider the quasi-static case (i.e., acceleration and velocity terms are much smaller compared to the external excitation and spring force terms), and the force-displacement relationship can be derived as follows:

$$F^{ex} = -\frac{k_\theta\left(\theta_1 - \theta_{1,0}\right)}{L\cos\theta_1}. \tag{A.7}$$

Note that F^{ex} is the external force applied to the roller joint as shown in Fig.4.1(b).

Appendix B

EQUATION OF MOTION FOR THE TCO-BASED METAMATERIALS

B.1 Equation of motion for the TCO-based 1D chain

To conduct analytical and numerical analysis, we derive the equation of motion by using the Hamiltonian based on the simplified TCO model. The TCO cell typically undergoes the planar deformation of its facets during folding/unfolding motions, so-called non-rigid origami motions. Thus, the analysis of the folding/unfolding motions of the TCO cell is extremely challenging. However, if we simplify this TCO cell into a truss structure, the derivation of analytical model is possible (see [Nature Comm] for more details). In this section, we briefly introduce this simplified model of the TCO unit cell, while the main focus will be placed on the dynamic equations of the TCO chain.

The first step in the simplified TCO model is to approximate the crease lines into linear springs. That is, we model the shorter ($\overline{A_aB}$ in Fig.2A) and longer crease lines ($\overline{A_bB}$ in Fig.2A) as linear springs whose spring constants are K_a and K_b, respectively. For the crease line along the N_p-sided interfacial polygons with the radius R of its circle circumscribing, we consider the bending motion between the triangular facet and the edge of the polygon. This bending behavior is modeled as a torsional spring with the spring constant, K_ψ. Let the length of the shorter and longer crease lines be a_n and b_n where n is the unit index, we obtain the following expressions:

$$a_n = \sqrt{\left(h_n^{(0)} - \Delta u_n\right)^2 + 4R^2\sin^2\left(\frac{\Delta\varphi_n}{2} + \frac{\theta_n^{(0)}}{2} - \frac{\pi}{2N_p}\right)}, \tag{B.1}$$

$$b_n = \sqrt{\left(h_n^{(0)} - \Delta u_n\right)^2 + 4R^2\sin^2\left(\frac{\Delta\varphi_n}{2} + \frac{\theta_n^{(0)}}{2} + \frac{\pi}{2N_p}\right)}. \tag{B.2}$$

where $h_n^{(0)}$ and $\theta_n^{(0)}$ are the initial height and rotational angle of the n-th TCO unit cell, respectively, and $\Delta u_n = u_n - u_{n+1}$ and $\Delta\varphi_n = \varphi_n - \varphi_{n+1}$. Also, let the bending angle for the edge crease line be ψ_n, it is expressed by

$$\psi_n = \tan^{-1}\left(\frac{h_0 - \Delta u_n}{R\left\{\cos\left(\pi/N_p\ \right) - \cos\left(\Delta\varphi_n + \theta_0\right)\right\}}\right). \tag{B.3}$$

Then, the elastic potential energy is

$$U_n\left(\Delta u_n, \Delta\varphi_n\right) = \frac{1}{2}N_p K_a\bigl(a_n - a_n^{(0)}\bigr)^2 + \frac{1}{2}N_p K_b\bigl(b_n - b_n^{(0)}\bigr)^2 + N_p K_\psi\bigl(\psi_n - \psi_n^{(0)}\bigr)^2 \tag{B.4}$$

where the superscript (0) denotes the initial states. The kinetic energy is

$$T_n = \frac{1}{2}M\dot{u}_n^2 + \frac{1}{2}J\dot{\varphi}_n^2 \tag{B.5}$$

where M and J are the mass and moment of inertia, respectively. The dot indicates the time derivative. Therefore, Hamiltonian is

$$H = \sum_n \left(T_n + U_n\right) = \sum_n \left\{\frac{1}{2M_n}p_n^2 + \frac{1}{2J_n}q_n^2 + U_n\left(\Delta u_n, \Delta\varphi_n\right)\right\} \tag{B.6}$$

where we define the following variables:

$$p_n = M\dot{u}_n, \qquad q_n = J\dot{\varphi}_n, \qquad . \tag{B.7}$$

Thus, the Hamilton's equations are

$$\dot{u}_n = \frac{\partial H}{\partial p_n} = \frac{1}{M}p_n, \tag{B.8}$$

$$\dot{\varphi}_n = \frac{\partial H}{\partial q_n} = \frac{1}{J}q_n, \tag{B.9}$$

$$\dot{p}_n = -\frac{\partial H}{\partial u_n} = \frac{\partial U_{n-1}}{\partial u_n} - \frac{\partial U_n}{\partial u_n}, \tag{B.10}$$

$$\dot{q}_n = -\frac{\partial H}{\partial \varphi_n} = \frac{\partial U_{n-1}}{\partial \varphi_n} - \frac{\partial U_n}{\partial \varphi_n}. \tag{B.11}$$

Then,

$$
\begin{aligned}
\frac{\partial U_n}{\partial u_n} &= F\left(\Delta u_n, \Delta\varphi_n\right) && \text{(B.12)}\\
&= -N_p K_a \left(h_0 - \Delta u_n\right)\left(1 - \frac{a_0}{a}\right) - N_p K_b \left(h_0 - \Delta u_n\right)\left(1 - \frac{b_0}{b}\right) && \text{(B.13)}\\
&- \frac{2N_p K_\psi \left(\psi_n - \psi_n^{(0)}\right)}{R\left\{\cos\left(\pi/N_p\right) - \cos\left(\Delta\varphi_n + \theta_0\right)\right\}\left[\frac{\left(h_0-\Delta u_n\right)^2}{R^2\left\{\cos\left(\pi/N_p\right)-\cos\left(\Delta\varphi_n+\theta_0\right)\right\}^2} + 1\right]}. && \text{(B.14)}
\end{aligned}
$$

and

$$
\begin{aligned}
\frac{\partial U_n}{\partial \varphi_n} &= T\left(\Delta u_n, \Delta\varphi_n\right) && \text{(B.15)}\\
&= N_p K_a R^2 \left(1 - \frac{a_0}{a}\right)\sin\left(\Delta\varphi_n + \theta_n^{(0)} - \frac{\pi}{N_p}\right) && \text{(B.16)}\\
&+ N_p K_b R^2 \left(1 - \frac{b_0}{b}\right)\sin\left(\Delta\varphi_n + \theta_n^{(0)} + \frac{\pi}{N_p}\right) && \text{(B.17)}\\
&- \frac{2N_p K_\psi \left(\psi_n - \psi_n^{(0)}\right)\left(h_0 - \Delta u_n\right)\sin\left(\Delta\varphi_n + \theta_0\right)}{R\left\{\cos\left(\pi/N_p\right) - \cos\left(\Delta\varphi_n + \theta_0\right)\right\}^2\left[\frac{\left(h_0-\Delta u_n\right)^2}{R^2\left\{\cos\left(\pi/N_p\right)-\cos\left(\Delta\varphi_n+\theta_0\right)\right\}^2} + 1\right]}. && \text{(B.18)}
\end{aligned}
$$

By using Eq. (B.8), the equations of motion are

$$
\begin{aligned}
M\ddot{u}_n &= F\left(\Delta u_{n-1}, \Delta\varphi_{n-1}\right) - F\left(\Delta u_n, \Delta\varphi_n\right) && \text{(B.19)}\\
J\ddot{\varphi}_n &= T\left(\Delta u_{n-1}, \Delta\varphi_{n-1}\right) - T\left(\Delta u_n, \Delta\varphi_n\right). && \text{(B.20)}
\end{aligned}
$$

Here F and T are the expressions of the axial force and torque as a function of displacement and rotational angle.

Please note that for linear wave analysis in Chapter 5, the spring constant K_ψ is not included in the analysis for the sake of simplicity. For the nonlinear wave anlysis in Chapter 7, by using this force expression, we apply the numerical optimization method (Least square method) to the experimental data of the force-displacement relationship, and determine the spring constants. Since we use the identical design of the crease to the shorter and longer crease lines, we assume the same material properties (Young's modulus) so that there is a relationship between K_a and K_b as $K_b = a^{(0)}/b^{(0)}K_a$. Thus, from the numerical optimization, we determine K_a and K_ψ, and then we calculate K_b.

Appendix C

DYNAMIC TEST ON THE CHAIN OF THE TCO UNIT CELLS

We conduct the dynamic test on the chain of the TCO unit cells by applying compressive impact to the system. For the chain of the TCO unit cells (Fig.1C), neighboring unit cells are connected mechanically by using M3 stainless steel screws and hex nuts. Also, a flanged sleeve bearing made of Polytetrafluoroethylene (PTFE) is embedded in the interfacial polygon, and the stainless steel shaft with diameter of 4.76 mm is inserted to align each TCO unit cell and constrain the unit cell motion to axial and rotational motions only. The left end of the chain (1st unit cell) is connected to the shaker (LDS V406 M4-CE, Brüel & Kjær) through the customized attachment with a sleeve bearing (PTFE), which attaches the left-most polygon of the cell to the shaker, but allows free rotational motions. The right end of the chain (20th unit cell) is fixed to the rigid wall. Note that by using this attachment with the sleeve bearing, we apply a desired compressive impact to the system, while allowing free rotational motions and restricting any bending motions of the unit cell. The shaker is excited by a single step voltage to inject compressive impact to the system.

To capture the dynamic folding/unfolding motion of each unit cell, we use six action cameras (GoPro HERO 4 BLACK), whose maximum frame rate is 240 fps (see the lower inset of Fig. 7.7 A). For extracting the TCO cells' displacement information from the recorded still shot images, we develope a customized non-contact digital image correlation technique by using Python and OpenCV [44]. To track the motion of each interfacial polygon, we use the color and shape as the features of a target marker. We attach a spherical markers to each corner of the polygons. For the color of the marker, fluorescent green is used to distinguish the marker of the polygons from the other objects. Figure C.1A is the original image from the GoPro camera, and then, with the mask based on the fluorescent green, we extracted the marker color area from the raw digital image (see the lower inset of Fig. C.1A). Lastly, we identify the marker from this filtered image by examining the shape of the extracted area and determine the 3D coordinate of each marker based on the triangulation method implemented in OpenCV [44]. By using three pairs of the action cameras, we split the field of view horizontally by three, and capture the axial and rotational motion of the polygons along the longitudinal axis based on the stereo vision. The all six cameras are calibrated by using OpenCV built-in function, and our in-house code processes the rectified images to obtain the 3D coordinate information. Figure C.1B shows the axial displacement change of the first interfacial polygon attached to the shaker attachment. For numerical simulations, we feed this experimentally-obtained displacement data into the equation of the first TCO element's motion.

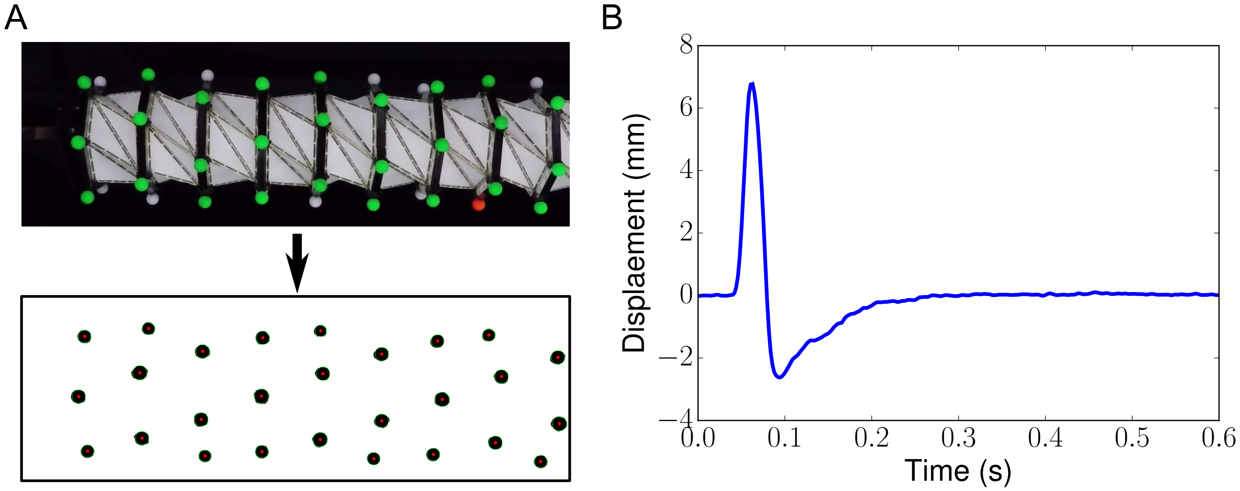

Figure C.1: Digital image correlation (DIC) technique to measure the axial displacement and the rotational angle of each polygon. (**a**) The upper photograph shows the image obtained by the action camera. The lower image shows the extracted marker based on the color of the marker. (**b**) DIC analysis result showing the axial displacement of the left-most polygon attached to the shaker attachment.

Appendix D

DERIVATION OF KDV EQUATION FROM THE TCO CHAIN

First, we derive the reduced equation of motion for the TCO chain by considering the first eigen-mode. Then, we implement the damping effect in the equation of motion. Based on the reduced model with damping, we take the continuum limit to obtain the KdV equation and discuss 1-soliton solution to analyze the rarefaction solitary wave.

D.1 Reduced 1D model

To investigate the wave propagation in the TCO-based system analytically, we reduce the two degree-of-freedom (DOF) model to a 1D model by linearizing the equation of motion obtained in the previous section, and we obtain a relationship between u and ϕ, which can eliminate one DOF from the equation of motion, by considering the eigenmode from the modal analysis.

First, we linearize the equation of motion. By applying the Taylor expansion to Eqs. (B.1) and (B.3), we obtain

$$\begin{aligned}
a_n(\Delta u_n, \Delta\varphi_n) &= a_n^{(0)} + \frac{\partial a_n}{\partial \Delta u_n}\Delta u_n + \frac{\partial a_n}{\partial \Delta\varphi_n}\Delta\varphi_n \\
&\quad + \frac{1}{2}\left\{ \frac{\partial^2 a_n}{\partial (\Delta u_n)^2}(\Delta u_n)^2 + 2\frac{\partial^2 a_n}{\partial \Delta u_n \partial \Delta\varphi_n}\Delta u_n \Delta\varphi_n + \frac{\partial^2 a_n}{\partial (\Delta\varphi_n)^2}(\Delta\varphi_n)^2 \right\} \\
&\quad + H.O.T., \qquad \text{(D.1)}
\end{aligned}$$

$$\begin{aligned}
b_n(\Delta u_n, \Delta\varphi_n) &= b_n^{(0)} + \frac{\partial b_n}{\partial \Delta u_n}\Delta u_n + \frac{\partial b_n}{\partial \Delta\varphi_n}\Delta\varphi_n \\
&\quad + \frac{1}{2}\left\{ \frac{\partial^2 b_n}{\partial (\Delta u_n)^2}(\Delta u_n)^2 + 2\frac{\partial^2 b_n}{\partial \Delta u_n \partial \Delta\varphi_n}\Delta u_n \Delta\varphi_n + \frac{\partial^2 b_n}{\partial (\Delta\varphi_n)^2}(\Delta\varphi_n)^2 \right\} \\
&\quad + H.O.T. \qquad \text{(D.2)}
\end{aligned}$$

where

$$\alpha_u = \left[\frac{\partial a_n}{\partial \Delta u_n}\right]_{\Delta u_n=0,\Delta\varphi_n=0} = -\frac{h_0}{\sqrt{h_0^2 + 4R^2 \sin^2\left(\frac{\theta_0}{2} - \frac{\pi}{2N_p}\right)}} = -\frac{h_0}{a_n^{(0)}}, \tag{D.3}$$

$$\alpha_\varphi = \left[\frac{\partial a_n}{\partial \Delta\varphi_n}\right]_{\Delta u_n=0,\Delta\varphi_n=0} = \frac{R^2 \sin\left(\theta_0 - \frac{\pi}{N_P}\right)}{a_n^{(0)}}. \tag{D.4}$$

Also,

$$\psi_n = \psi_n^{(0)} + \frac{\partial \psi_n}{\partial \Delta u_n}\Delta u_n + \frac{\partial \psi_n}{\partial \Delta\varphi_n}\Delta\varphi_n + \cdots \tag{D.5}$$

where

$$\frac{\partial \psi_n}{\partial \Delta u_n} = -\frac{1}{R\left\{\cos\left(\pi/N_p\ \right) - \cos\theta_0\right\}\left[1 + \frac{h_0^2}{R^2\{\cos(\pi/N_p\ ) - \cos\theta_0\}^2}\right]}, \tag{D.6}$$

$$\frac{\partial \psi_n}{\partial \Delta\varphi_n} = -\frac{h_0 \sin\theta_0}{R\{\cos\left(\pi/N_p\ \right) - \cos\theta_0\}^2\left[1 + \frac{h_0^2}{R^2\{\cos(\pi/N_p\ ) - \cos\theta_0\}^2}\right]}. \tag{D.7}$$

The force and torque are linearized as follows:

$$\frac{\partial U_n}{\partial u_n} = F(\Delta u_n, \Delta\varphi_n) \approx F_{u1}\Delta u_n + F_{\varphi 1}\Delta\varphi_n, \tag{D.8}$$

$$\frac{\partial U_n}{\partial \varphi_n} = T(\Delta u_n, \Delta\varphi_n) \approx T_{u1}\Delta u_n + T_{\varphi 1}\Delta\varphi_n. \tag{D.9}$$

where

$$F_{u1} = N_p\left\{K_a(\alpha_u)^2 + K_b(\beta_u)^2 + 2K_\psi(\gamma_u)^2\right\}, \tag{D.10}$$

$$T_{u1} = N_p\left\{K_a\alpha_u\alpha_\varphi + K_b\beta_u\beta_\varphi + 2K_\psi\gamma_u\gamma_\varphi\right\}, \tag{D.11}$$

$$T_{\varphi 1} = \left\{K_a(\alpha_\varphi)^2 + K_b(\beta_\varphi)^2 + 2K_\psi(\gamma_\varphi)^2\right\}. \tag{D.12}$$

If we only consider a single unit cell, the equations of motion can be linearized as follows:

$$\frac{d^2 u_1}{dt} = -F\left(\Delta u_n, \Delta\varphi_n\right) = -\left(\frac{F_{u1}}{M}u_1 + \frac{F_{\varphi 1}}{M}\varphi_1\right), \tag{D.13}$$

$$\frac{d^2 \varphi_1}{dt^2} = -T\left(\Delta u_n, \Delta\varphi_n\right) = -\left(\frac{T_{u1}}{J}u_1 + \frac{T_{\varphi 1}}{J}\varphi_1\right). \tag{D.14}$$

The matrix form in

$$\frac{d^2}{dt^2}\begin{bmatrix} u_1 \\ \varphi_1 \end{bmatrix} = \begin{bmatrix} F_{u1}/M_n & F_{\varphi 1}/M_n \\ T_{u1}/J_n & T_{\varphi 1}/J_n \end{bmatrix}\begin{bmatrix} u_1 \\ \varphi_1 \end{bmatrix} \tag{D.15}$$

Next, we conduct the modal analysis and find the eigenmode to approximate the folding motion of the TCO Let

$$\begin{aligned} u_1 &= u \exp\left(-i\omega t\right), \\ \varphi_1 &= \varphi \exp\left(-i\omega t\right). \end{aligned}$$

we solve the eigenvalue problem as follows:

$$-\omega^2\begin{bmatrix} u \\ \varphi \end{bmatrix} = \begin{bmatrix} F_{u1}/M_n & F_{\varphi 1}/M_n \\ T_{u1}/J_n & T_{\varphi 1}/J_n \end{bmatrix}\begin{bmatrix} u \\ \varphi \end{bmatrix} \tag{D.16}$$

Thus,

$$\det\left(\mathbf{A} - \omega^2\mathbf{I}\right) = \mathbf{O} \tag{D.17}$$

where

$$\mathbf{A} = \begin{bmatrix} F_{u1}/M_n - \omega^2 & F_{\varphi 1}/M_n \\ T_{u1}/J_n & T_{\varphi 1}/J_n - \omega^2 \end{bmatrix} \tag{D.18}$$

Hence,

$$\omega^2 = \frac{1}{2}\left(\frac{F_{u1}}{M} + \frac{T_{\varphi 1}}{J}\right) \pm \frac{1}{2}\sqrt{\left(\frac{F_{u1}}{M} + \frac{T_{\varphi 1}}{J}\right)^2 - 4\left(\frac{F_{u1}T_{\varphi 1}}{MJ} - \frac{F_{\varphi 1}T_{u1}}{MJ}\right)} \tag{D.19}$$

Then, the eigenvectors are calculated as follows:

$$\begin{bmatrix} F_{\varphi_1}/M \\ \omega^2 - F_{u1}/M \end{bmatrix} \tag{D.20}$$

Then, by selecting the lower eigenmode, we get the 1D approximation of the relationship between axial displacement and rotational angle as follows:

$$\varphi = \alpha u \tag{D.21}$$

where

$$\alpha = \frac{\omega^2 - F_{u1}}{F_{\varphi 1}} \tag{D.22}$$

For analytical and numerical analysis, we choose the lowest eigenmode which is plotted as the gray dashed line in the inset figure of Fig.2C.

By using this relationship, we can reduce the original equation of motion as follows: Here, let

$$\tilde{M} = M + \alpha^2 J, \tag{D.23}$$

we approximate the length of each crease line as follows:

$$\begin{aligned}
a_n &\approx \sqrt{\left(h_n^{(0)} - \Delta u_n\right)^2 + 4R^2 \sin^2\left(\frac{\alpha}{2}\Delta u_n + \frac{\theta_n^{(0)}}{2} - \frac{\pi}{2N_p}\right)}, \\
b_n &\approx \sqrt{\left(h_n^{(0)} - \Delta u_n\right)^2 + 4R^2 \sin^2\left(\frac{\alpha}{2}\Delta u_n + \frac{\theta_n^{(0)}}{2} + \frac{\pi}{2N_p}\right)}, \\
\psi_n &\approx \tan^{-1}\left(\frac{h_0 - \Delta u_n}{R\left\{\cos\left(\pi/N_p\right) - \cos\left(\alpha \Delta u_n + \theta_0\right)\right\}}\right).
\end{aligned}$$

Then, we apply the Taylor expansion to these expressions as follows:

$$\begin{aligned}
a_n &\approx a_n^{(0)} + A_1 \Delta u_n + A_2 (\Delta u_n)^2 + O(3), \\
b_n &\approx b_n^{(0)} + B_1 \Delta u_n + B_2 (\Delta u_n)^2 + O(3), \\
\psi_n &\approx \psi_n^{(0)} + C_1 \Delta u_n + C_2 (\Delta u_n)^2 + O(3).
\end{aligned}$$

where

$$\begin{aligned}
A_1 &= \left[\frac{da_n}{d(\Delta u_n)}\right]_{\Delta u_n=\Delta\varphi_n=0} = -\frac{h_0}{a_n^{(0)}} + \frac{\alpha R^2 \sin\left(\theta_0 - \pi/N\right)}{a_n^{(0)}}, \\
A_2 &= \frac{1}{2}\left[\frac{d^2 a_n}{d(\Delta u_n)^2}\right]_{\Delta u_n=\Delta\varphi_n=0} = \frac{1}{2a_n^{(0)}} + \frac{\alpha^2 R^2 \cos\left(\theta_0 - \pi/N\right)}{2a_n^{(0)}} - \frac{\left\{h_0 - \alpha R^2 \sin\left(\theta_0 - \pi/N\right)\right\}^2}{2\left\{a_n^{(0)}\right\}^3}, \\
B_1 &= \left[\frac{db_n}{d(\Delta u_n)}\right]_{\Delta u_n=\Delta\varphi_n=0} = -\frac{h_0}{b_n^{(0)}} + \frac{\alpha R^2 \sin\left(\theta_0 + \pi/N\right)}{b_n^{(0)}}, \\
B_2 &= \frac{1}{2}\left[\frac{d^2 b_n}{d(\Delta u_n)^2}\right]_{\Delta u_n=\Delta\varphi_n=0} = \frac{1}{2b_n^{(0)}} + \frac{\alpha^2 R^2 \cos\left(\theta_0 + \pi/N\right)}{2b_n^{(0)}} - \frac{\left\{h_0 - \alpha R^2 \sin\left(\theta_0 + \pi/N\right)\right\}^2}{2\left\{b_n^{(0)}\right\}^3}, \\
C_1 &= \left[\frac{d\psi_n}{d(\Delta u_n)}\right]_{\Delta u_n=\Delta\varphi_n=0} = -\frac{1}{R\eta}\left[\frac{1}{\cos\left(\pi/N\right) - \cos\left(\theta_0\right)} + \frac{\alpha h_0 \sin\theta_0}{\left\{\cos\left(\pi/N\right) - \cos\left(\theta_0\right)\right\}^2}\right], \\
C_2 &= \frac{1}{2}\left[\frac{d^2 \psi_n}{d(\Delta u_n)^2}\right]_{\Delta u_n=\Delta\varphi_n=0} \\
&= \frac{1}{2R\eta^2\left\{\cos\left(\pi/N\right) - \cos\left(\theta_0\right)\right\}^2} \\
&\quad \left[2\alpha\eta\sin\theta_0 - \alpha^2\eta h_0\cos\left(\theta_0\right) + \frac{2\alpha^2\eta h_0 \sin\theta_0}{\cos\left(\pi/N\right) - \cos\left(\theta_0\right)}\right. \\
&\quad \left. -\left\{1 + \frac{\alpha h_0 \sin\theta_0}{\cos\left(\pi/N\right) - \cos\left(\theta_0\right)}\right\}\left\{\frac{2h_0}{R^2\left\{\cos\left(\pi/N\right) - \cos\left(\theta_0\right)\right\}} + \frac{2\alpha h_0^2 \sin\theta_0}{R^2\left\{\cos\left(\pi/N\right) - \cos\left(\theta_0\right)\right\}^3}\right\}\right].
\end{aligned}$$

where

$$\eta = 1 + \frac{h_0^2}{R^2\left\{\cos\left(\pi/N\right) - \cos\left(\theta_0\right)\right\}^2} \tag{D.24}$$

Substituting these into the force, we get

$$\frac{\partial U_n}{\partial u_n} \approx N_p\left(K_a A_1^2 + K_b B_1^2 + 2K_\psi C_1^2\right)\Delta u_n + 2N_p\left\{K_a A_1 A_2 + K_b B_1 B_2 + 2K_\psi C_1 C_2\right\}\left(\Delta u_n\right)^2 + O(3) \tag{D.25}$$

Therefore, the reduced 1D equation of motion is

$$\begin{aligned}
\tilde{M}\ddot{u}_n &= F\left(\Delta u_{n-1}\right) - F\left(\Delta u_n\right) \\
&= N_p\left(K_a A_1^2 + K_b B_1^2 + 2K_\psi C_1^2\right)\left(\Delta u_{n-1} - \Delta u_n\right) \\
&\quad + 2N_p\left\{K_a A_1 A_2 + K_b B_1 B_2 + 2K_\psi C_1 C_2\right\}\left\{\left(\Delta u_{n-1}\right)^2 - \left(\Delta u_n\right)^2\right\} + O(3)
\end{aligned}$$

D.2 Equation of motion with damping effect

To account for damping effect, we modify the Hamiltonian and derive the equations of motion in which the damping effect is considered. By introducing a damping coefficient (ν), we modify the Hamiltonian as follows:

$$H = \sum_n \left(T_n + U_n\right) e^{\nu t} = \sum_n \left\{ \frac{1}{2M_n} p_n^2 e^{-\nu t} + \frac{1}{2J_n} q_n^2 e^{-\nu t} + e^{\nu t} U_n \left(\Delta u_n, \Delta\varphi_n\right) \right\} \tag{D.26}$$

where

$$\begin{aligned} p_n &= M \dot{u}_n e^{\nu t}, \\ q_n &= J \dot{\varphi}_n e^{\nu t}. \end{aligned}$$

Then, similarly to the previous section, the Hamilton's equations of motion are

$$\begin{aligned} \dot{u}_n &= \frac{\partial H}{\partial p_n} = \frac{1}{M} p_n e^{-\nu t}, \\ \dot{\varphi}_n &= \frac{\partial H}{\partial q_n} = \frac{1}{J} q_n e^{-\nu t}, \\ \dot{p}_n &= -\frac{\partial H}{\partial u_n} = \left(\frac{\partial U_{n-1}}{\partial u_n} - \frac{\partial U_n}{\partial u_n} \right) e^{\nu t}, \\ \dot{q}_n &= -\frac{\partial H}{\partial \varphi_n} = \left(\frac{\partial U_{n-1}}{\partial \varphi_n} - \frac{\partial U_n}{\partial \varphi_n} \right) e^{\nu t}. \end{aligned}$$

Therefore the equations of motion are

$$M\ddot{u}_n + \nu_u \dot{u}_n = F\left(\Delta u_{n-1}, \Delta\varphi_{n-1}\right) - F\left(\Delta u_n, \Delta\varphi_n\right), \tag{D.27}$$

$$J\ddot{\varphi}_n + \nu_\varphi \dot{\varphi}_n = T\left(\Delta u_{n-1}, \Delta\varphi_{n-1}\right) - T\left(\Delta u_n, \Delta\varphi_n\right). \tag{D.28}$$

where $\nu_u = M\nu$ and $\nu_\varphi = J\nu$. For the numerical simulations, we use Eq. (D.27).

Also, the 1D approximated equation of motion is

$$\tilde{M}\ddot{u}_n + \nu \dot{u}_n = F\left(\Delta u_{n-1}\right) - F\left(\Delta u_n\right) \tag{D.29}$$

D.3 Continuum limit

To analyze the rarefaction solitary wave propagating in the TCO-based system, we take continuum limit, and derive 1-soliton solution. First, we apply the Taylor expansion

$$\begin{aligned} u_{n\pm1} &= u_n \pm h_0 \frac{\partial u_n}{\partial x} + \frac{h_0^2}{2!}\frac{\partial^2 u}{\partial x^2} \pm \frac{h_0^3}{3!}\frac{\partial^3 u}{\partial x^3} + \frac{h_0^4}{4!}\frac{\partial^4 u}{\partial x^4} \pm \cdots, && \text{(D.30)} \\ \varphi_{n\pm1} &= \varphi_n \pm h_0 \frac{\partial \varphi_n}{\partial x} + \frac{h_0^2}{2!}\frac{\partial^2 \varphi}{\partial x^2} \pm \frac{h_0^3}{3!}\frac{\partial^3 \varphi}{\partial x^3} + \frac{h_0^4}{4!}\frac{\partial^4 \varphi}{\partial x^4} \pm \cdots. && \text{(D.31)} \end{aligned}$$

Then, the relative displacement and angle are expressed by

$$\begin{aligned} \Delta u_n &= u_n - u_{n+1} = -h_0 \frac{\partial u}{\partial x} - \frac{h_0^2}{2!}\frac{\partial^2 u}{\partial x^2} - \frac{h_0^3}{3!}\frac{\partial^3 u}{\partial x^3} - \frac{h_0^4}{4!}\frac{\partial^4 u}{\partial x^4}, && \text{(D.32)} \\ \Delta u_{n-1} &= u_{n-1} - u_n = -h_0 \frac{\partial u}{\partial x} + \frac{h_0^2}{2!}\frac{\partial^2 u}{\partial x^2} - \frac{h_0^3}{3!}\frac{\partial^3 u}{\partial x^3} + \frac{h_0^4}{4!}\frac{\partial^4 u}{\partial x^4}, && \text{(D.33)} \\ \Delta \varphi_n &= \varphi_n - \varphi_{n+1} = -h_0 \frac{\partial \varphi}{\partial x} - \frac{h_0^2}{2!}\frac{\partial^2 \varphi}{\partial x^2} - \frac{h_0^3}{3!}\frac{\partial^3 \varphi}{\partial x^3} - \frac{h_0^4}{4!}\frac{\partial^4 \varphi}{\partial x^4}, && \text{(D.34)} \\ \Delta \varphi_{n-1} &= \varphi_{n-1} - \varphi_n = -h_0 \frac{\partial \varphi}{\partial x} + \frac{h_0^2}{2!}\frac{\partial^2 \varphi}{\partial x^2} - \frac{h_0^3}{3!}\frac{\partial^3 \varphi}{\partial x^3} + \frac{h_0^4}{4!}\frac{\partial^4 \varphi}{\partial x^4}. && \text{(D.35)} \end{aligned}$$

Substituting these equations into the reduced 1D model, we obtain

$$\begin{aligned} \frac{\partial^2 u}{\partial t^2} &= \frac{N_p\left(K_a A_1^2 + K_b B_1^2 + 2K_\psi C_1^2\right)}{\tilde{M}} \left(h_0^2 \frac{\partial^2 u}{\partial x^2} + \frac{h_0^4}{12}\frac{\partial^4 u}{\partial x^4}\right), && \text{(D.36)} \\ &\quad + \frac{2N_p\left\{K_a A_1 A_2 + K_b B_1 B_2 + 2K_\psi C_1 C_2\right\}}{\tilde{M}} \left(-2h_0^3 \frac{\partial u}{\partial x}\frac{\partial^2 u}{\partial x^2} + \cdot\right) && \text{(D.37)} \end{aligned}$$

By ignoring the higher order terms ($O(3)$), we obtain

$$u_{tt} + \frac{\nu c_0}{\tilde{M}} u_t = c_0^2 u_{xx} + \frac{c_0^2 h_0^2}{12} u_{xxxx} - B u_x u_{xx} \tag{D.38}$$

where

$$\begin{aligned} c_0 &= h_0 \sqrt{\frac{N_p\left(K_a A_1^2 + K_b B_1^2 + 2K_\psi C_1^2\right)}{\tilde{M}}}, && \text{(D.39)} \\ B &= \frac{4h_0^3 N_p\left\{K_a A_1 A_2 + K_b B_1 B_2 + 2K_\psi C_1 C_2\right\}}{\tilde{M}}. && \text{(D.40)} \end{aligned}$$

Here, c_0 is the speed of the sound of the medium, and we compare this sound speed with the wave speed of the solitary wave.

By introducing the traveling coordinate $X = x - c_0 t$, $\xi = -\partial u/\partial X$, and slower time $\tau = (1/2\ )\,\varepsilon c_0 t$, we obtain

$$c_0^2 \left\{ -\xi_X + \varepsilon \xi_\tau - \frac{1}{4}\varepsilon^2 u_{\tau\tau} \right\} + \frac{\nu c_0}{\tilde{M}} \left(\xi + \frac{1}{2}\varepsilon u_\tau \right) = -c_0^2 \xi_X - \frac{c_0^2 h_0^2}{12} \xi_{XXX} - B\xi\xi_X \tag{D.41}$$

If we assume that ν and ε are in the same order, and we neglect $O(\varepsilon^2)$ and we get

$$\xi_\tau + \frac{h_0^2}{12\varepsilon}\xi_{XXX} + \frac{B}{\varepsilon c_0^2}\xi\xi_X + \gamma\xi = 0 \tag{D.42}$$

where $\gamma = \nu/\varepsilon c_0 \tilde{M}$. The leading-order 1-soliton solution for this damped KdV equation has been studied [68, 69], and we utilize their result which is expressed by

$$\xi(X,\tau) = \xi_{amp}(\tau)\mathrm{sech}^2\left[\Lambda^{-1}\left\{X - V(\tau)\tau\right\}\right] \tag{D.43}$$

where

$$\begin{aligned}
\xi_{amp}(\tau) &= \xi_{amp}(0)\exp\left(-\frac{4\gamma}{3}\tau\right), \\
V(\tau) &= \frac{B\xi_{amp}(0)}{3\varepsilon c_0^2}\exp\left(-\frac{4\gamma}{3}\tau\right), \\
\Lambda^2 &= \frac{c_0^2 h_0^2}{B\xi_{amp}(0)}\exp\left(\frac{4\gamma}{3}\tau\right).
\end{aligned}$$

VITA

Hiromi Yasuda was born in Yokohama, Japan. He earned his B.S. in Aerospace Engineering from Nihon University, College of Science and Technology, Japan in 2011, and his M.S. in Mechanical Engineering from the University of Washington in 2014. In Summer 2014, he joined the Laboratory for Engineered Materials and Systems (LEMS), led by Professor Jinkyu Yang, at the University of Washington. In 2018, he earned a Ph.D. degree in Aeronautics & Astronautics from the University of Washington.